**Clouds and the Earth's Radiant Energy System (CERES)**

**Algorithm Theoretical Basis Document**

# Compute Surface and Atmospheric Fluxes (System 5.0)

Thomas P. Charlock1
Fred G. Rose2
David A. Rutan2
Timothy L. Alberta2
David P. Kratz1
Lisa H. Coleman2
G. Louis Smith1
Nitchie Manalo-Smith2
T. Dale Bess1

1NASA Langley Research Center
Hampton, VA 23681-0001

2Analytical Services and Materials, Inc.
One Enterprise Parkway
Hampton, VA 23666

3Science Applications International Corporation (SAIC)
One Enterprise Parkway, Suite 250
Hampton, VA 23666

Release 2
May 1997

CERES Algorithm Theoretical Basis Document

# CERES Top Level Data Flow Diagram

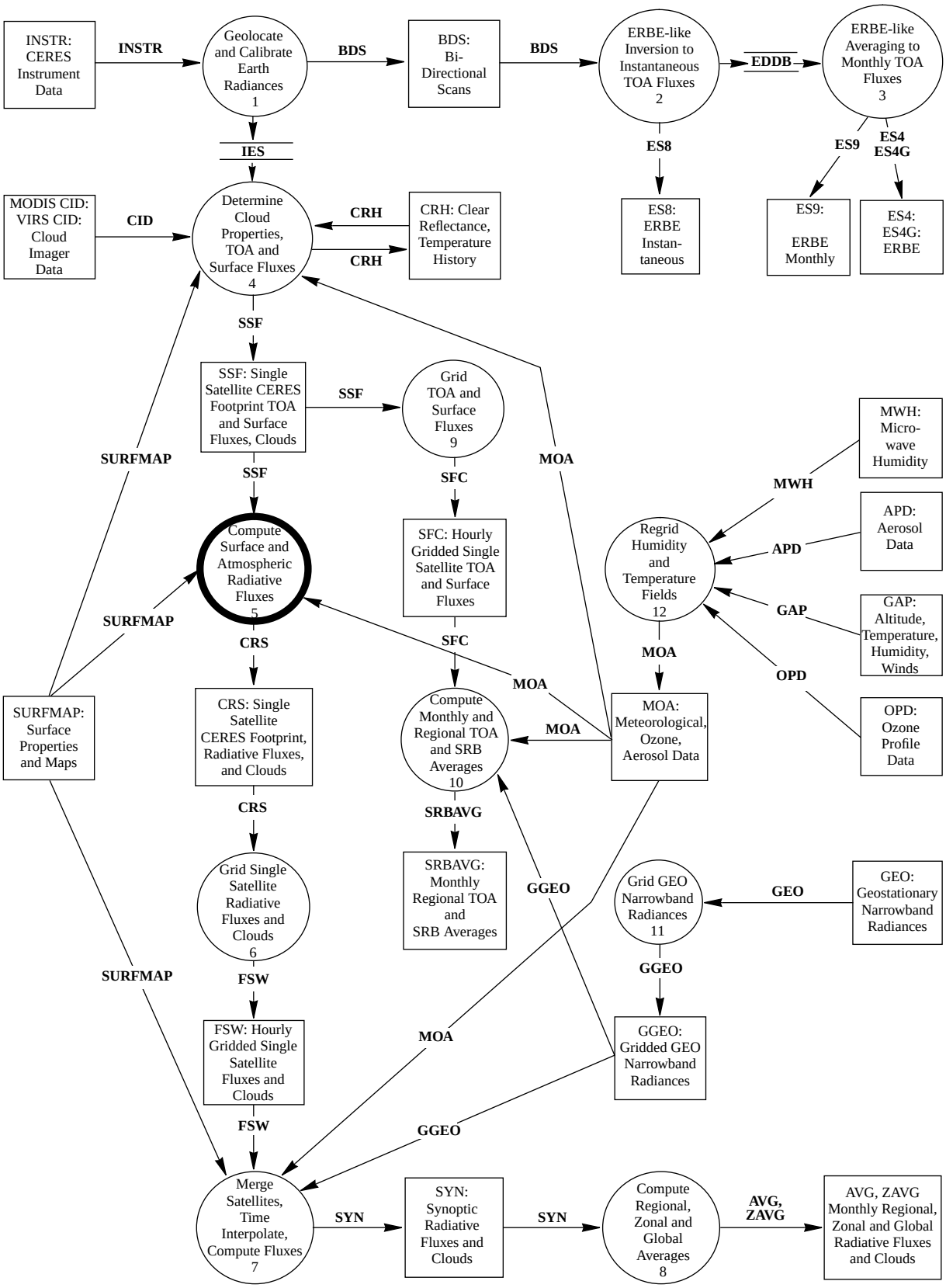

**Abstract**

This document presents preliminary algorithms for the Clouds and the Earth's Radiant Energy System (CERES) retrieval of the vertical atmospheric profile of shortwave (SW, solar wavelengths) and longwave (LW, thermal infrared wavelengths) radiative fluxes: the Surface and Atmospheric Radiation Budget (SARB). The CERES effort to retrieve the SARB produces three sets of radiative fluxes as (a) the full vertical profile of fluxes in the atmosphere and at the surface, determined from radiative transfer calculations that match the simultaneously observed CERES Top-Of-the-Atmosphere (TOA) fluxes, (b) an independent, parameterized set of radiative fluxes at the surface only, that are also simultaneous with the CERES TOA fluxes, and (c) the full vertical profile of fluxes in the atmosphere and at the surface as estimated for synoptic times (i.e., 3-hourly UTC). This document provides a brief scientific overview of all three sets of radiative fluxes, but its main purpose is to discuss the preliminary CERES SARB retrieval algorithms which will be utilized to obtain the first (a) of these three sets of radiative fluxes. The vertical profile of fluxes is calculated with satellite imager-retrieved clouds and meteorological data as inputs. The input parameters are constrained to match the modeled TOA fluxes with the observed CERES broadband TOA fluxes. Since the initial unconstrained radiative transfer calculations generally do not match the observed CERES TOA fluxes, the unconstrained fluxes at the surface and TOA are archived for use in diagnostic studies of the radiative transfer techniques, the CERES cloud retrievals, and other parameters.

Draft Validation Plans for this and other components of CERES are presently available from the EOS Project Office home page (http://eospso.gsfc.nasa.gov and click first on “Validation,” second on “DOCUMENTS,” third on “Validation Plans,” and fourth on “CERES” for the most current version).

## 5.0 Compute Surface and Atmospheric Fluxes

### 5.1 Introduction

The Surface and Atmospheric Radiation Budget (SARB) is the primary driver of the hydrological cycle and the general circulation of the atmosphere. Anthropogenically induced changes in radiatively active trace gases, aerosols, and the earth’s surface will affect the SARB and force a climatic response. There are, however, formidable challenges to developing accurate SARB records in CERES, or in the Earth Observing System (EOS) generally. While certain components of the SARB can now be determined with existing data, other components, to be determined with even marginal accuracy, must wait for theoretical advances; the development of new observing systems; active remote sensing on satellites (lidar and sub-cm cloud profiling radar); and especially more accurate and extensive long-term surface-based (1) monitoring of fluxes and (2) remote sensing of cloud and aerosol radiative properties. CERES will be an unique opportunity to expand the space and time domain wherein the SARB can be specified accurately. The CERES program will not only provide accurate TOA broadband fluxes and simultaneous cloud property retrievals, but will also be well suited to determine the effects of clouds on the various components of the SARB. The CERES SARB product will be an important integrating tool for resolving the radiation issues in climate analysis and prediction that are associated with cloud feedback, aerosol forcing, and land-use forcing.

The SARB algorithms in this document essentially complete the instantaneous satellite-based component of the CERES mission. Other CERES documents describe the more fundamental retrievals of TOA broadband radiative fluxes with the CERES instrument, the retrievals of cloud properties with the Advanced Very High Resolution Radiometer (AVHRR), High Resolution Infrared Sounder (HIRS/2), Visible Infrared Scanner (VIRS) and Moderate Resolution Imaging Spectroradiometer (MODIS) imaging instruments, and the preparation of meteorological and ancillary data which are used in both the cloud and SARB retrievals.

This document will discuss the retrieval of the SARB firstly from a theoretical standpoint. Then, we describe more concretely the pre-launch "Release 1" SARB retrieval that has been produced by the CERES team, using AVHRR and Earth Radiation Budget Experiment (ERBE) data, and the NCEP (National Centers for En-

vironmental Prediction) Reanalysis from October 1986. Only the first orbit of Release 1 will be shown in the Figures of this document. Release 1 has been superceeded by a longer, full-day test called Release 1.5 (figures from Release 1.5 are not included in this document). We further describe the more ambitious launch-ready Release 2. Release 2 is being programmed at this writing. Goddard EOS Data Assimilation System (GEOS-DAS) meteorological data (the successor to GEOS-1 described by Schubert et al., 1995) and/or the NCEP Reanalysis (Kalnay et al., 1996) will be used for Release 2 (as it was for the recent Release 1.5). Release 2 will be used by CERES for the Tropical Rainfall Measuring Mission (TRMM) launch in late 1997. Plans for the post-launch Releases 3 and 4 are presented very roughly. Release 3 will span the full globe with the MODIS cloud imager on the polar orbiters EOS-AM and PM. Release 4, which will follow Release 2 by about 2 years, will use updated angular distribution models (ADMs) for more accurate TOA broadband fluxes (the 2 years of sampling with the single rotating azimuth plane scanner RAPS on TRMM will be needed to develop new ADMs). Results from a prototype "Version 0" software were described in an earlier ATBD. Version 0 is no longer in use. Version 0 and Releases 1-4 are summarized in Table 1.

Table 1 CERES Version 0 and Release 1-3 for SARB product

| *Name* | *Broadband* | *Imager and* | *Vertical* | *Domain* |
|---|---|---|---|---|
| *Date* | | *Met. data* | | |
| | | | | |
| **Version 0** | ERBE | AVHRR | 26 levels | Oct. 86 (1 orbit) |
| Feb. 94 | | NMC | calculated | |
| | | | | |
| **Release 1** | ERBE | AVHRR | 4 levels in | Oct. 86 (1 orbit) |
| summer 96 | | NCEP Reanal. | release | **figs. used here** |
| | | | | |
| **Release 1.5** | ERBE | AVHRR | 4 levels in | Oct. 86 (1 day) |
| spring 97 | | GEOS-1 DAS | release | |
| | | | | |
| **Release 2** | CERES | VIRS | 4 levels in | TRMM |
| post-launch | | DAS or NCEP | release | |
| | | | | |
| **Release 3** | CERES | MODIS | 4 levels in | EOS-AM/PM |
| post-launch | | DAS or NCEP | release | |
| | | | | |
| **Release 4** | CERES | MODIS | 4 (or more) | EOS-AM/PM |
| post-launch | new ADMs | | levels | |

Frequent reference to Releases 1, 1.5, and 2 in this document for Subsystem 5 (SARB) may be confusing for the reader who is following documents from other CERES Subsystems. The other CERES Subsystem documents focus heavily on a description of plans for flight-ready Release 2 software. The SARB production software has changed greatly from Version 0. This document also describes the SARB Subsystem for Release 1, which has the bulk of the software changes from Version 0; changes which are planned for SARB Release 2 software; planned and ongoing investigations using other models and analysis not pertaining directly to CERES production code.

## 5.2 Overview and Background Information

### 5.2.1 Experimental Objectives

An accurate record of the SARB is needed (1) to validate the radiation simulations in climate models and (2) to parse and quantify currently uncertain forcings due to aerosols and land surfaces. Most General Circulation Models (GCMs) spend several tens of percent of their computational burden determining the SARB. Our techniques for the retrieval of SARB vertical profiles have been tested with radiative transfer codes (Harshvardhan et al. 1987; Wang et al. 1991; Chou 1992; Fu and Liou 1993) that have been been built for GCM-type applications. We use the simple concept of constrainment to achieve balance with broadband TOA observations. First, the SARB is calculated with standard meteorological data from NCEP (Release 1) and/or DAO (Release 2) and satellite-retrieved cloud properties as input parameters; the cloud properties are produced by the CERES team with cloud imager data (see Subsystem 4 documents; AVHRR for Version 0, AVHRR and HIRS for Release 1, VIRS on the TRMM spacecraft, and MODIS on EOS). Second, the computed TOA fluxes are compared with observed broadband fluxes (ERBE radiometer for Version 0 and Release 1, CERES radiometer for Release 2). Then, in a constrainment process, the most uncertain and radiatively effective input parameters are adjusted to bring recalculated SARB to balance with the observed TOA broadband fluxes. The amount of constrainment of the cloud parameters that is required to balance the broadband TOA observations is useful for evaluating the quality of the CERES products (see Subsystem 4 documents).

The SARB effort in CERES is directed at providing a set of through-the-atmosphere radiative fluxes that are applicable to large-scale general circulation and climate studies. Radiative fluxes also influence cloud processes at the microscale, but because we are working at the scale of CERES footprints (roughly 20 km and much larger than the cloud imager pixels or the spacing of a cloud resolving non-hydrostatic model), the CERES SARB will be too coarse for the study of cloud systems at high resolution. SARB retrievals will provide energy fluxes that can be compared to GCM outputs directly, side-stepping the problem posed by different definitions of cloudiness in satellite retrievals and models. The CERES SARB products are anticipated to be useful for GCM validation because, as energy fluxes, they may be readily averaged in space and time. Other satellite-derived parameters (like cloud optical depth) relate to energy non-linearly and are thus more difficult to average and intercompare with GCMs.

We anticipate that the initial, unconstrained calculation (radiative transfer based on unadjusted input parameters) of SARB fluxes will be useful for diagnostic studies immediately after launch. The initial, unconstrained calculations will be compared with the first generation of CERES "ERBE-like" TOA fluxes (observed fluxes based on the old ERBE ADMs). A few years after launch, new CERES ADMs will be produced with the CERES RAPS data, yielding a more accurate observed TOA record. CERES TOA observations account for 3-D effects empirically, and it will be interesting to compare them with the CERES SARB calculations. The CERES SARB calculations are based on the plane parallel assumption, as are the CERES cloud retrievals. The constrainment that is required to bring the calculated plane parallel fluxes to a match with the CERES TOA observations will provide a diagnosis of the plane parallel assumption, which is widely used in models and retrievals.

At what stage of the CERES experiment are the constrained vertical profiles of radiative fluxes likely to be reliable? For *clear skies over oceans* with TRMM (VIRS imager), we anticipate that early confidence could be placed on the constrained vertical profile of *LW* SARB fluxes that match the CERES TOA observations with the new ADMs. We will rely on the water vapor sounding channels on MODIS (on EOS-AM) for spot checking of the TRMM LW SARB cooling rates in narrow bands. We could be confident of the constrained CERES SARB fluxes for *LW over clear sky oceans and land* in the EOS polar orbiter missions, as the MODIS imager has improved capabilities for aerosol, surface emissivity, and skin temperature retrieval over land. The TRMM ADMs will not be available until after the launch of EOS-AM, but the new ADMs will mostly affect the SW. In LW, the quality of our SARB product will likely depend more heavily on the water vapor profile in DAO and/or NCEP.

Confidence in any CERES clear-sky SW product below the TOA will depend in part on the resolution of present discrepancies between measured and computed clear-sky surface SW fluxes (Wild et al., 1995), which has been reported by groups using different codes and instruments in ARM (Charlock and Alberta, 1996; Kato et al., 1996) and FIRE (Kinne et al., 1996). When this issue ("SW codes and measurements disagree for clear skies") is resolved, the SARB fluxes at the tropopause (i.e., above cloud tops) should also be reliable, even for total-sky conditions, early in the EOS polar orbiter missions. A few years of post-launch study and validation will be needed, before constrained SARB fluxes would be regarded as reliable below cloud tops. With some cloud systems, we will never be certain of the SARB. Even with the projected deployment of cloud profiling radars (with smaller wavelength than the precipitation radar on TRMM), the additional information on high optical depth systems would be limited. A lidar mission would provide vital data for thin optical depth systems like cirrus. Such a lidar mission, coupled with adequate ground-based monitoring, may be needed to accurately determine the SW atmospheric heating induced by aerosol.

The atmospheric portion of the SARB is calculated at many vertical levels (38 levels in the ERBE- and AVHRR-based exercise of Release 1 reported here). Formally, at the first SARB release 24 months after launch, however, only the fluxes at the TOA, tropopause, and surface will be issued; this presumes satisfactory performance of the initial launch-ready Release 2 code. Fluxes at 500 hPa will be released 30 months after launch as the 4th flux reported in the "vertical" column of Table 1. Following validation of CERES cloud property products (Subsystem 4) and SARB fluxes (Subsystem 5), we anticipate that multiple levels of SARB fluxes will be issued not sooner than 36 months after launch. As cloud overlap and cloud vertical thickness have substantial impacts, especially on the LW SARB, CERES validation activities will focus on cloud base height and cloud thickness, as well as on radiative fluxes.

While much of CERES is oriented toward the tropospheric aspects of global change, the CERES SARB should also be useful for stratospheric studies. The 9.6 micrometer O3 band is important for stratosphere-troposphere radiative exchange (Ramanathan and Dickinson 1979), because stratospheric O3 absorbs upwelling photons from the warmer lower troposphere. CERES will determine the properties of the cloud tops, which are important in the modulation of the upwelling window flux and thus the stratospheric radiation balance. Because the tropopause is almost always above the cloud tops, the fluxes near the tropopause can be retrieved with more confidence than at lower levels. The radiative balance near the tropopause is vital because anthropogenic forcing has been calculated to heat the troposphere but cool the stratosphere (i.e., Intergovernmental Panel on Climate Change IPCC,1990). Raval and Ramanathan (1989) and Stephens and Greenwald (1991) have used ERBE and other data to quantitatively assess the clear-sky LW greenhouse effect of the integrated atmospheric column. The CERES SARB product will serve as the basis for a more highly resolved analysis.

We anticipate that a detailed analysis of Release 4 CERES SARB fluxes for clear-sky conditions will be essential for the accurate determination of anthropogenic radiative climate forcing in IPCC. Radiative forcing must be determined, if we are to interpret the climate record in terms of cause and effect, and if we hope to understand climate with deterministic models. Radiative forcings due to $CO_2$, $CH_4$, $N_2O$, and CFCs can be specified fairly accurately because the concentrations of these well-mixed species are routinely monitored, and their spectroscopic properties are well known. The radiative forcings by changes in aerosol (Penner et al., 1994) and land use are uncertain, however; aerosols are not well-mixed, and their optical properties are not routinely monitored. By combining CERES clear-sky SARB results with ground-based measurements of broadband surface radiative flux and aerosol optical properties, focused validation studies should be able to separate the radiative signals due to changes in surface and aerosol properties. If such CERES validation can be done at 50-100 sites around the globe, secular changes in land-surface radiative forcing and aerosol radiative forcing could be monitored effectively. 50-100 ground-based sites are needed because aerosol effects tend to be regional, while land surface effects are more localized. The aerosol forcing from the satellite can be validated on a regional basis with data from surface sites, permitting the more varied local land surface forcings to be inferred from space observations. As noted earlier, a space-based lidar mission may be required to close the issue of aerosol heating. We presently lack such a combined satellite and surface monitoring system, and the full anthropogenic radiative forcing of climate remains uncertain. Plans for the ground-based aspects of this activity are described in forthcoming CERES Validation Plans .

### 5.2.2 Historical Perspective

The importance of the vertical profile of the atmospheric radiation budget was demonstrated with the development of the 1-dimensional radiative-convective model (Manabe and Wetherald 1967). A change in the concentration of an infrared-active trace gas would change the model's temperature profile, but once in the new equilibrium state, the corresponding change to the broadband TOA planetary radiation budget could be very small or even vanish. The temperature profile would be maintained in the new equilibrium state by a significant vertical redistribution of energy fluxes within the atmosphere. Stephens and Webster (1984) further noted that clouds could play a vital role in such a process.

A 3-dimensional model study by Hartmann et al. (1984) showed that the vertical distribution of atmospheric energy fluxes affects the primary modes of circulation, in addition to the temperature structure. The GCM results of Ting and Sardeshmukh (1993) indicate that a redistribution of vertical fluxes within the tropics would affect teleconnections to midlatitudes. The vertical energy fluxes are produced mainly by radiative (to be retrieved by CERES) and latent (to be retrieved using radar and other instruments on TRMM, i.e., Tao et al. 1993) processes. The full vertical profile of radiative flux divergence is needed to determine the effect of radiation on the generation of Available Potential Energy (APE; Lorenz 1955; Stuhlmann and Smith 1988ab). Ramanathan et al. (1983) demonstrated the importance of the atmospheric LW budget in the simulation of the midlatitude jet in a GCM. The substantial effect of tropical cloud LW radiative forcing on atmospheric heating and circulation has been demonstrated with a GCM by Slingo and Slingo (1991); the accuracy of the LW forcing was noted to be critical for computing impacts such as Amazon deforestation. The importance of radiation within the atmosphere for circulation has been demonstrated in other studies (e.g., Donner and Kuo 1984; Slingo and Slingo 1988; Randall et al. 1989; Hoskins, 1996).

London (1957) and Dopplick (1972) are classical, pre-satellite estimates of the SARB, based on radiative transfer calculations with climatological data. The retrieval of radiative fluxes at the surface has been advanced by Darnell et al. (1992) and Pinker and Laszlo (1992a) using International Satellite Cloud Climatology Project (ISCCP) data (Schiffer and Rossow 1983; Rossow et al. 1991), as well as with HIRS/2 (Wu and Chang 1992), Nimbus 7 (Chertock et al. 1991; Charlock et al. 1990), GOES VISSR (Gautier and Frouin 1992), and ERBE (Cess et al. 1991; Li and Leighton 1993). The retrieval of surface LW fluxes has been developed at NASA LaRC by Darnell et al. (1992) and Gupta (1989). The World Climate Research Program (WCRP) Global Energy and Water Cycle Experiment (GEWEX; Chahine 1992) has established a formal project (Whitlock et al. 1995) that retrieves the global surface radiation budget (SRB), with the results archived at the NASA LaRC EOS DAAC (Distributed Active Archive Center). The GEWEX SRB (surface only) Project has used radiometric observations, compiled as the Global Energy Balance Archive (GEBA) by the Swiss Federal Institute (Ohmura and Gilgen 1993), for the validation of SW fluxes; for the annual (24 hour) domain of the GEBA sites, the mean monthly surface SW insolation as calculated from satellite measurements is usually 10-15 $Wm^{-2}$ larger than the observations. The WCRP has organized a program of more precise surface observations, at a limited number of sites, in the Baseline Surface Radiation Network (BSRN). NOAA runs a Surface Radiation Budget Network (SURFRAD; Hicks et al., 1996) in the U.S. The development of these pioneering programs for surface fluxes provides the groundwork for validating the combined retrieval of surface and atmospheric flux profiles in CERES.

Calculations of clear-sky LW fluxes have been compared to broadband observations from aircraft for some time (Ellingson and Gille 1978). The recent Spectral Radiation Experiment (SPECTRE) activity (Ellingson and Wiscombe, 1995), which provides an observational data base for clear-sky radiances, can be expected to hone more accurate codes for the calculation of LW and SW vertical flux profiles. Calculated cloudy-sky broadband fluxes are often compared to observations at selected vertical-levels in field campaigns (i.e., Stackhouse and Stephens 1989; Fu and Liou 1993). In an investigation of the energetics of small, cloud-scale systems (Churchill and Houze 1991), broadband flux profiles have been calculated with input data from aircraft and radar, and the calculated fluxes have been compared with observations (Churchill 1992). Field campaigns have not resolved the issue of the possible "anomalous" SW absorption by clouds (Cess et al., 1995; Ramanathan et al., 1995; Pilewskie and Valero, 1995; Li et al. 1995; Hayasaka et al., 1995; Chou et al., 1995;

Ramaswamy and Friedenreich, 1992), which has been reported for decades. Stephens and Tsay (1990) have examined hypotheses for the cause of anomalous absorption such as the presence of large droplets, cloud absorbing aerosol, enhanced continuum absorption, and cloud inhomogeneities. They conclude that better measurements are required to resolve the discrepancies.

In applying satellite data to the global scale, we have about two decades of experience in the retrieval of temperature profiles and about one decade of experience in the retrieval of clouds. The large-scale, satellite-based retrieval of the full vertical profiles of radiative fluxes is a much newer activity. Stephens et al. (1993) use ERBE and Special Sensor Microwave/Imager (SSM/I) data to estimate the LW cooling of the full atmospheric column (rather than multi-layer profiles) over the oceans. Ellingson et al. (1994) describe an experimental program at National Atmospheric and Oceanic Administration (NOAA) to retrieve the clear-sky LW heating rate for 4 atmospheric layers with HIRS/2 data; observed narrowband radiances are used in a statistical fit to detailed radiative transfer calculations.

Stuhlmann et al. (1993) used METEOSAT data to produce vertical profiles of both LW and SW fluxes. METEOSAT-derived cloud optical depth was used to determine the cloud ice water path (IWP) or liquid water path (LWP) following Rockel et al. (1991); water content is estimated using relations due to Fiegelson (1978) and Paltridge (1974); cloud geometric thickness was obtained from the ratio of water path to water content. Stuhlmann et al. (1993) then retrieved the flux profiles with delta-2-stream calculations based on the method of Schmetz (1984). For April 1985, the equator-to-pole temperature gradient over the METEOSAT region was found to be strengthened by the effects of net cloud generated radiative heating.

Clear-sky and total-sky LW flux profiles have been computed (Charlock et al. 1993) with ISCCP data (Rossow et al. 1991) and the Harshvardhan et al. (1987) radiation code over the globe. The calculated outgoing longwave radiation (OLR) was compared (but not constrained) with ERBE, and the calculated surface downward longwave flux (DLF) was compared with a time-matched NMC Numerical Weather Prediction (NWP) simulation. Different cloud overlap assumptions produced very different vertical profiles of LW divergence. Despite the uncertainty due to cloud overlap, it was possible to determine that LW divergence fluctuations damp temperature fluctuations in most of the troposphere, but systematically enhance temperature fluctuations in a few regions.

### 5.2.3 Community Access

The extensive aircraft and surface measurements which have been initiated in the Department of Energy Atmospheric Radiation Measurement Program (ARM; Stokes and Schwartz, 1994) provide theoreticians with some of the tools needed to address the retrieval of more components of the SARB. In cooperation with the GEWEX Continental-Scale International Project (GCIP; Leese, 1995), CERES has formed an on-line experiment with which to engage the scientific community in the evaluation, improvement, and application of techniques to retrieve the vertical profile of radiative fluxes. A web page (http://snowdog.larc.nasa.gov:8081/cagex.html) has been established to facilitate access to CERES research on the SARB. Version 1 (Fig. 0) of the CERES/ARM/GEWEX Experiment (CAGEX) provides complete on-line files for

(1) satellite-based cloud properties and atmospheric sounding data that fulfill input requirements for calculations with broadband radiative transfer models;

(2) vertical profiles of radiative fluxes calculated with those data as input; and

(3) measurements of broadband radiative fluxes and cloud properties for comparison with some of the flux calculations and input data.

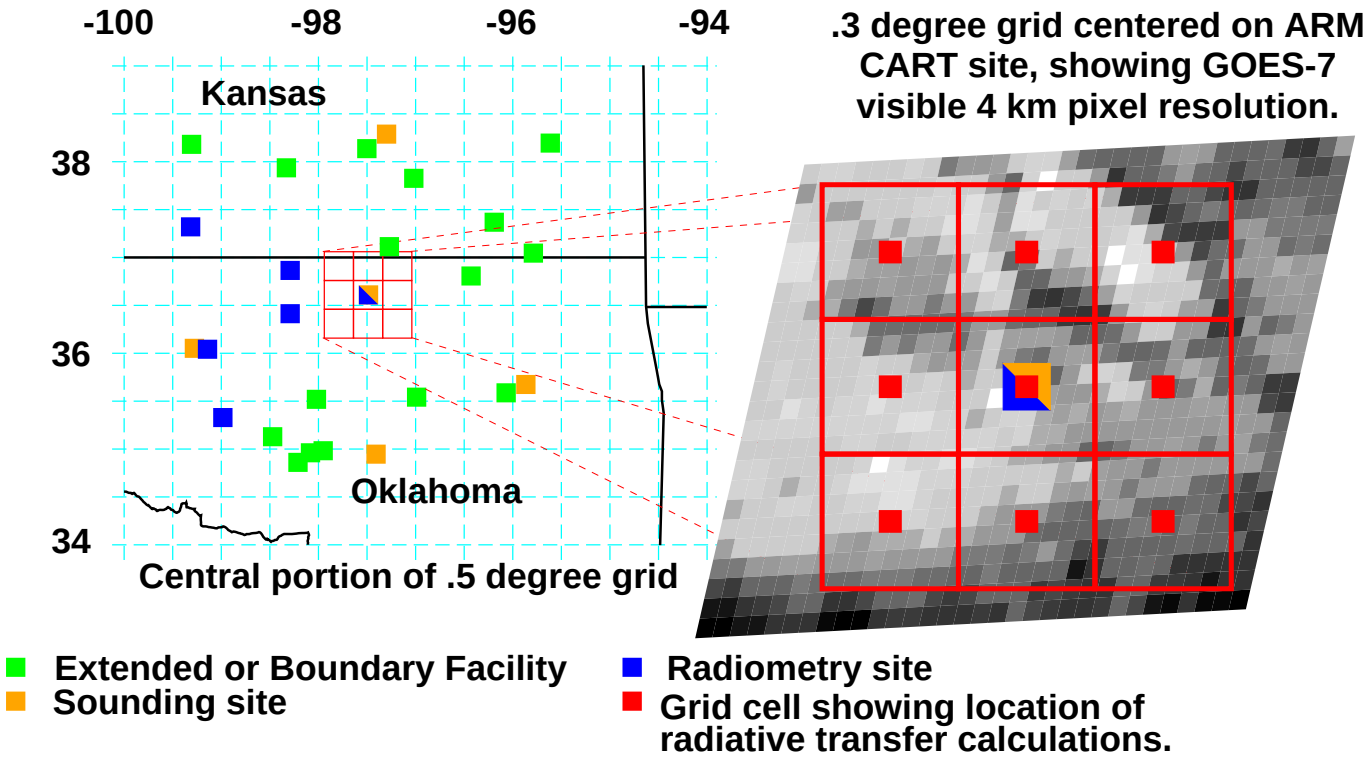


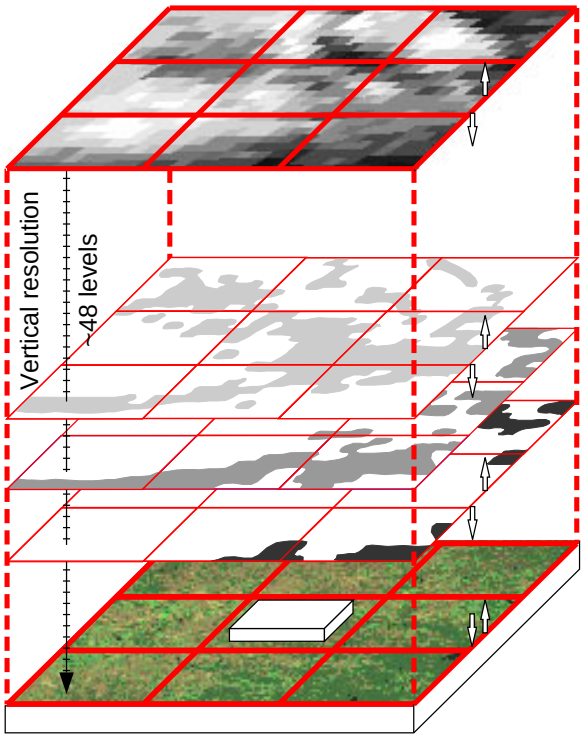


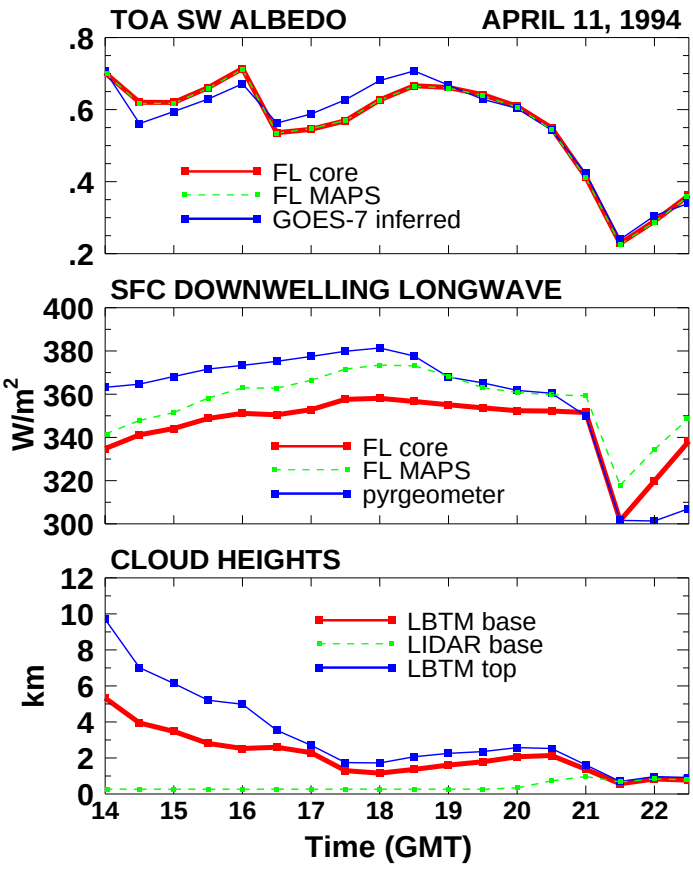


## The CERES/ARM/GEWEX Experiment (CAGEX)

Figure 0. - CAGEX on-line (http://snowdog.larc.nasa.gov:8081/cagex.html)

Version 1 covers the ARM Southern Great Plains (SGP) Cloud and Radiation Testbed (CART) site with a 3 by 3 grid ($0.3^o$ on each side) every 30 minutes from 1409 UTC to 2239 UTC (daylight) for 26 days, starting on April 5, 1994. CAGEX (Charlock and Alberta, 1996) is used to test Release 1 algorithms with the unique array of ARM measurements. Subsequent versions will be used for the development and testing of Releases 2, 3, and 4 for the validation of CERES products after launch. Interaction with the ARM and GEWEX communities through this vehicle has thus far been helpful. We are learning which components of our pre-launch products are most questionable, and also which are the most useful to NWP and hydrology researchers. CAGEX is proving an invaluable tool for combining satellite and ground-based data to describe the atmosphere more accurately.

### 5.2.4 Characteristics of EOS Data

CERES retrievals will have several advantages over earlier SARB retrievals because of the improved characteristics of the EOS data that will be applied. Most importantly, CERES footprint-scale broadband TOA fluxes will be available as tie points for SARB calculations. The CERES broadband footprints will have a resolution twice that of ERBE (Barkstrom et al. 1989). Data from the CERES rotating RAPS scanner will permit the development of improved angular and directional models, reducing the error in the broadband albedo especially.

The scene identification for the CERES angular and directional models will, unlike ERBE (Wielicki and Green 1989), include the use of high resolution cloud imager data for each footprint. This will increase the accuracy of the CERES broadband TOA fluxes and SARB calculations. CERES will distinguish clear scenes more reliably than ERBE, because of both the application of cloud imager data and the higher spatial resolution of the CERES broadband sensor. CERES cloud retrievals on the TRMM mission will use the VIRS imager. Unlike AVHRR, VIRS has a 1.60 micrometer channel, which will be useful for identifying the phase of particles (liquid water or ice) in cloud tops. The phase of the cloud particles can have a dramatic impact on the cloud optical properties and the effect of the cloud on the radiation budget (Liou 1992). Knowledge of the particle phase permits a more accurate retrieval of cloud height and optical depth (Minnis et al. 1993a, b). The Minnis et al. (1993a, b) Layer Bispectral Threshold Method (LBTM) technique has been somewhat successful with estimations of cloud geometric thickness, a parameter which significantly influences the LW SARB. On the EOS AM and PM spacecraft, CERES will use the MODIS cloud imager. MODIS has a higher spatial resolution than VIRS or present cloud imagers, and the spectral coverage of the MODIS channels is more suited to cloud retrieval than AVHRR and HIRS/2. Wielicki and Parker (1992) have noted the increased accuracy in the retrieval of cloud area that is obtained with higher spatial resolution. Because of the low TRMM orbital altitude, VIRS will have a substantially higher spatial resolution than AVHRR.

Besides instrumentation, other aspects of the EOS data stream are anticipated to increase the accuracy of the CERES cloud retrieval. GEOS-DAS operational temperature and humidity profiles will be available for cloud vertical placement. NCEP Reanalysis profiles were used for CERES pre launch Release 1 calculations shown in this document. ISCCP (Rossow et al. 1991) was restricted to approximately daily Tiros Operational Vertical Sounder (TOVS) soundings, while Nimbus 7 cloud retrievals (Stowe et al., 1988) were based on climatological temperature lapse rates. We anticipate that, deeper in the CERES post-launch time frame, the GEOS-DAS and NCEP humidity profiles will benefit from microwave-based retrievals on the Defense Meteorological Satellite Program (DMSP), TRMM, and EOS. The European Center for Medium Range Weather Forecasts (ECMWF) has reported on a radiance-based assimilation of TOVS data that has yielded dramatic improvements in the analyzed humidity profiles (i.e., Hollingsworth, 1996). The current CERES preferrence is for a multi-year "frozen" (i.e., no unnatural variability due to changes in the algorithm itself) analysis by GEOS-DAS.

Information on aerosol optical thickness will be available for CERES SARB calculations. On TRMM, CERES will retrieve aerosols with the VIRS sensor. On EOS, aerosol retrievals will be produced by the MODIS and Multi-angle Imaging Spectro-Radiometer (MISR) teams. While MODIS will attempt to retrieve the absorbing properties of aerosol, this will be significant challenge for the first years after launch. The best prospects for retrieving aerosol absorption will be over validation sites where ground-based optical depth and

broadband flux measurements are colocated. Over these sites, the surface, CERES, and MODIS data will be integrated, and a more reliable clear-sky SARB can then be produced. In Releases 3, 4 or later, the algorithms honed over the validation sites will be applied to yield accurate, global records of aerosol radiative forcing and the residual surface radiative forcing.

## 5.3 Algorithm Description

### 5.3.1 Radiative transfer

**5.3.1.1 Codes for radiative transfer.** The SARB component of CERES presently has used several broadband radiative transfer codes. The broadband radiative transfer codes (as distinguished from the SARB retrieval algorithms that employ them) were developed outside of NASA LaRC and have been generously provided to CERES by Drs. Ming-Dah Chou, Qiang Fu, Harshvardhan, Kuo-Nan Liou, and Wei-Chyung Wang. The radiation codes determine tropospheric and stratospheric broadband fluxes fairly efficiently and have been tested in the International Comparison of Radiation Codes in Climate Models (ICRCCM; Ellingson and Fouquart 1990). The Chou (1992), Fu and Liou (1993), Harshvardhan et al. (1987), and Wang et al. (1991) codes all use the plane-parallel assumption. Because of computational resources, we do not use narrowband or line-by-line radiative transfer codes for global processing.

Harshvardhan et al. (1987) developed a fast broadband code for GCM application. The code was used in Version 0 processing (Table 1) as described in the earlier ATBD 5.0, but is no longer active in CERES. The Harvardhan et al. (1987) LW code accounts for absorption and emission using methods by Chou (1984) for water vapor, by Chou and Peng (1983) for carbon dioxide, and by Rodgers (1968) for ozone. This code treats clouds as black bodies.

The Wang et al. (1991) longwave code includes the minor species methane (CH4), nitrous oxide (N2O), dichloroflouro carbon (CF2Cl2), and trichloroflouro carbon (CFCl3). This code is partly based on the Wang and Shi (1988) parameterization for total band absorptance in a homogeneous layer. The Wang et al. (1991) code is fast. CERES uses it as a test, rather than production, code for large scale OLR calculations

We use the Chou (1992) SW code for testing, rather than production, too. The Chou (1992) code employs the Liou et al. (1988) delta-4-stream treatment of clouds and aerosols. Clear and scattering layers are composited with the 2-stream adding method. The effects of H2O, O3, CO2, O2 and Rayleigh scattering are included. In a clear atmosphere, near infrared absorption by water vapor is computed with a broadband technique. In an atmosphere with scattering by clouds or aerosols, water vapor absorption is computed with the k-distribution method.

The Fu and Liou (1993) code is the principal research and production tool for SARB activities in CERES. The delta-4-stream approach agrees with adding-doubling calculations to within 5% for fluxes and is a considerable improvement over a 2-stream calculation (Liou et al., 1988). In the Fu and Liou (1993) code, numerical solutions for large optical depths are enabled by use of the scaling technique of Stamnes and Conklin (1984); results have been checked with the "exact" adding technique of Liou (1992). The Fu and Liou (1993) code accounts for the scattering of both LW and SW radiation, as do earlier studies by Stackhouse and Stephens (1991) and Ritter and Geleyn (1992). The correlated-k-distribution method for gaseous absorption is employed. Run time increases approximately linearly with the number of vertical levels. This contrasts with some "emissivity" codes, wherein the run time expands with the square of the number of levels.

The Fu and Liou (1993) code was selected for CERES, in part because of (a) the wide span of input parameters included, (b) speed, and (c) accuracy. To speed computer processing, CERES uses the faster 2-stream version for SW and the 2/4-stream version for LW. The 2/4-stream version (Fu et al., 1997) uses the faster 2-stream LW source function, but places it in the 4-stream framework for accuracy comparable to straight 4-stream calculations. The code accounts for the radiative effects of $H_2O$, $CO_2$, $O_3$, $O_2$, CH4, and $N_2O$; Rayleigh scattering; aerosols; liquid cloud droplets; hexagonal ice crystals (random orientation); and spectrally dependent surface reflectivity. Six spectral intervals are used in the SW (0.2-4.0 μm); twelve spectral inter-

vals are used in the LW (2200-1 $cm^{-1}$). We use a further revsion by Qiang Fu which resolves the first 0.2-0.7 μm band, originally spanned with correlated k's, into 10 separate sub-bands for a more accurate characterization of the spectral dependence of aerosol optical properties. The Roberts et al. (1976) water vapor continuum (280-1250 $cm^{-1}$) has been replaced with an economical parameterization (developed by CERES team members Fred G. Rose and David P. Kratz) of the more recent CKD2.1 (Clough et al., 1992) continuum. The uniform mixing ratios for $CO_2$, $CH_4$, and $N_2O$ are respectively 330, 1.6, and 0.28 ppmv; mixing ratios in our global Release 1 (1986) and small-scale CAGEX (1994 and 1995) applications were larger, but the total difference in the forcing with these more recent concentrations would amount to less than 1 $Wm^{-2}$. CFCs are not included in the calculation, but CFC forcing is also less than 1 $Wm^{-2}$. For the principal atmospheric gases, the Fu-Liou (1993) code matches a line by line (LBL) simulation of fluxes to within 0.05% for SW; 0.2% for LW excepting $O_3$; and ~2% for LW fluxes due to O3. An updated line data base is not expected to change results substantially. It should be noted, however, that there are significant uncertainties relating to the treatment of the $H_2O$ continuum (i.e., Clough et al., 1992) in radiative transfer codes generally. ICRCCM and SPECTRE are anticipated to provide more definitive evaluations of radiative transfer codes as a guide to their improvement.

CERES also applies more specialized, faster parameterizations to produce fluxes at the surface only. The CERES surface-only parameterizations, which are described in other documents, apply algorithms based on Li et al. (1993), Gupta et al. (1992) and the activities of Inamdar and Ramanathan (1994).

**5.3.1.2 Illustrations of LW cooling rates and fluxes.** Here, we provide a few examples of the LW SARB and its relationship to parameters that CERES will determine from broadband ERBE-like measurements, cloud imager, NWP analyses, and other data. The latest version of the Fu et al. (1997) code has not been used in the examples shown in this sub-section.

In Fig. 1a-d, the Wang et al. (1991) code has been used to compute the broadband LW fluxes for a climatological midlatitude summer condition. For clear skies (Fig. 1a), the LW cooling rate (deg K/day) is shown in solid. The dashed profile (Fig. 1a) shows the LW cooling rate for the same atmospheric sounding, but with an increase of 2 deg K in the surface temperature. By increasing the temperature of the surface (skin only) by 2 deg K, the cooling rate in the lowest 100 hPa has been reduced by about 25%; the clear-sky OLR has increased by 1.8 $Wm^{-2}$ (note "1.8" in upper right portion of Fig. 1a); the downward longwave flux (DLF) has not changed ("0.0" indicated in lower right portion of Fig. 1a). In a SARB retrieval for CERES, an initial temperature and humidity profile from NMC is used to compute the LW cooling rate profile indicated in solid in Fig. 1a. If the computed clear-sky OLR is 1.8 $Wm^{-2}$ less than the broadband CERES observation, one constrainment option would be an increase in the surface skin temperature by 2 deg K. The dashed line in Fig. 1a shows the resulting, hypothetically constrained, clear-sky cooling rate profile.

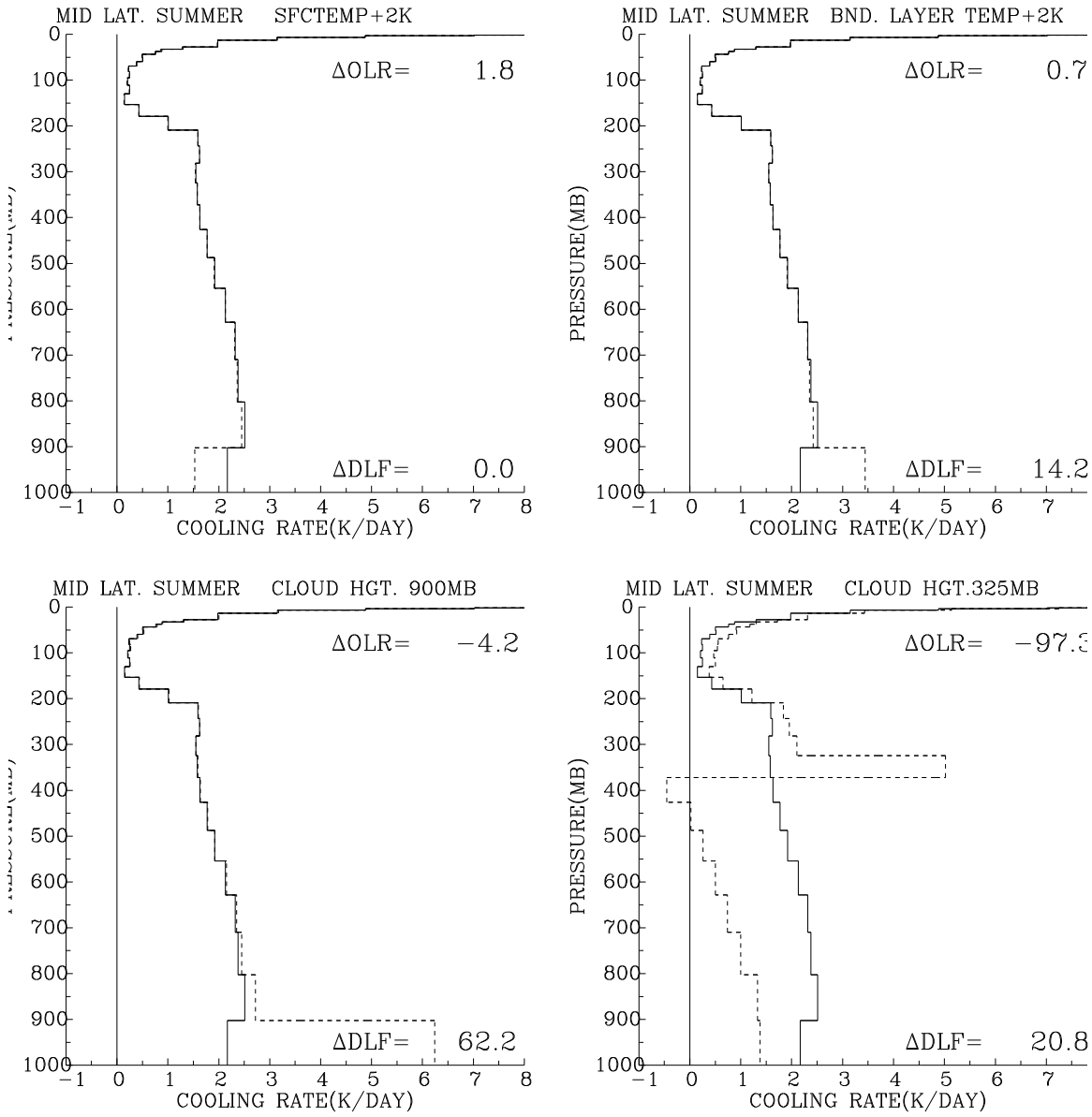


Figure 1 Broadband LW cooling rates (deg K/day) for midlatitude summer climatological (solid) and perturbed atmospheres. Change in OLR (as perturbed OLR minus climatological OLR) in upper right of each panel in W/m**2; change in DLF in lower right of each panel in W/m**2. Perturbations in panel on upper left (a) surface temperature increased by 2 deg K, on upper right (b) temperature in layer at 950hPa increased by 2 deg K, on lower left (c) cloud placed in layer with top at 900 hPa , and on lower right (d) cloud placed in layer with top at 325 hPa

Constrainment can also be done by adjusting the temperature, cloud, and humidity profiles within the atmosphere. In Fig. 1b (upper right), we have applied a 2-deg K increase, to the atmospheric layer only, between 900 and 1000 hPa. The dashed line (Fig. 1b) indicates that the 900-1000 hPa LW cooling rate has increased

from 2.2 deg K/day to 3.4 deg K/day. The OLR has increased by only 0.7 Wm-2, but the DLF has increased by 14.2 $Wm^{-2}$.

Fig. 1c-d show how important clouds are for the LW SARB. In Fig. 1c, the dashed line shows the dramatically increased cooling rate for a midlatitude summer atmosphere with a black cloud added to the layer 900-1000 hPa. The low cloud increases the DLF by 62.2 $Wm^{-2}$ but decreases the OLR by only 4.2 $Wm^{-2}$ (Fig. 1c). In Fig. 1d, the black cloud has been moved to the layer between 300 and 350 hPa. For the high black cloud, the LW cooling rate increases slightly at the cloud layer, but it significantly decreases below the cloud, while the OLR falls by 97.3 $Wm^{-2}$ and the DLF increases by 20.8 $Wm^{-2}$(Fig. 1d).

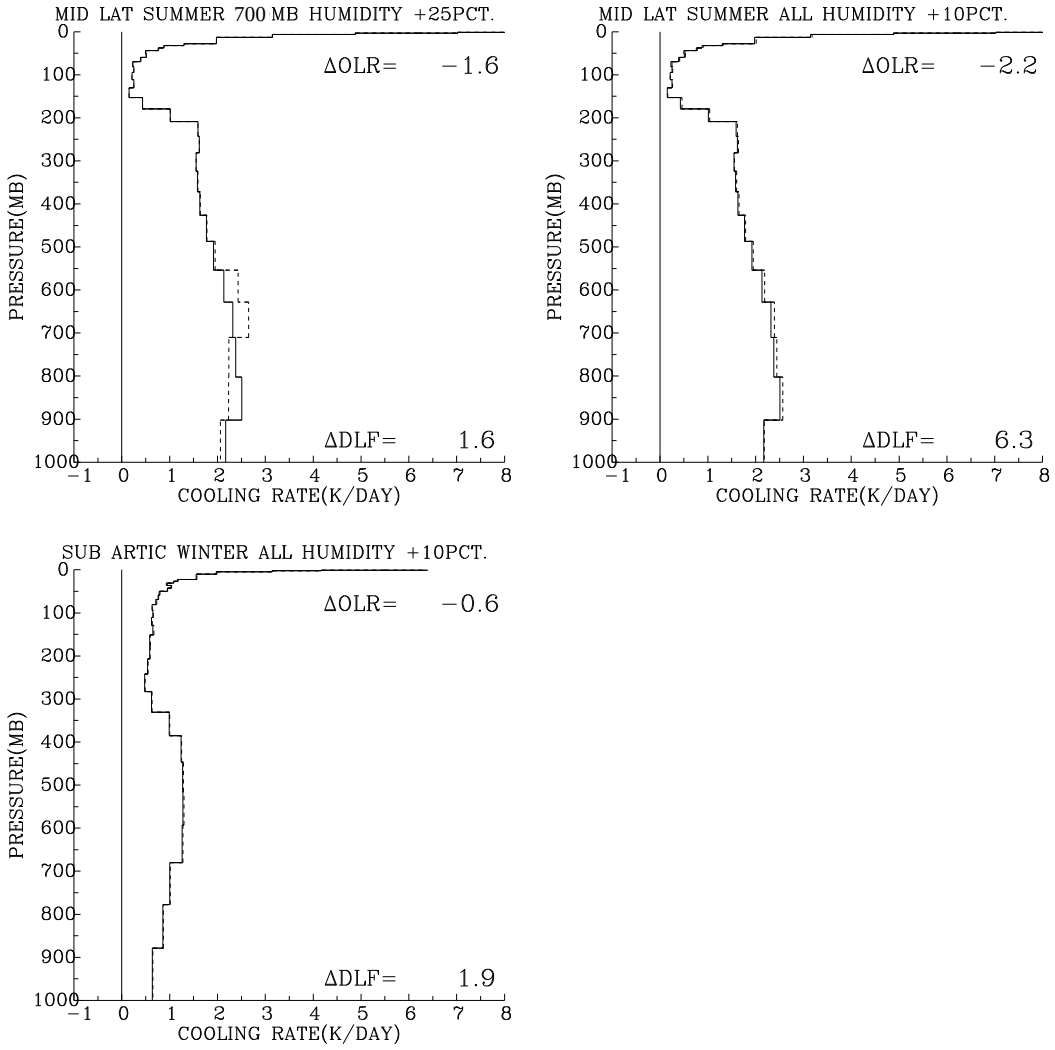


Figure 2 Broadband LW cooling rates (deg K/day) for climatological (dashed) and perturbed (solid) atmospheres. Change in OLR ( as perturbed OLR minus climatological OLR) in upper right of each panel in W/m**2 ; change in DLF in lower right of each panel in W/m**2. Perturbations in panel on upper left (a) for midlatiude summer, an increase in the humidity of the layer at 700 hPa by 25%, on upper right (b) for midlatitude summer, an increase in the humidity of all layers by 10%, and on lower left (c) for subartic winter, an increase in the humidity of all layers by 10%.

The impact of changes in the humidity profile to the LW SARB is shown in Fig. 2a-c. Note that the solid lines in Fig. 2a-b use the same climatological midlatitude summer profile as the solid lines in Figs. 1a-d. By increasing the humidity between 700-800 hPa by 25%, the cooling rate is increased in that layer and decreased in the layer below; the OLR drops by only 1.6 $Wm^{-2}$, and the DLF increases by 1.6 $Wm^{-2}$ (Fig. 2a). In Fig. 2b, the humidity has been increased by 10% at all levels, giving a larger drop in the OLR (2.2 $Wm^{-2}$) and a larger increase in the DLF (6.3 $Wm^{-2}$), but the impact on the cooling rate at any individual level is small. The same 10% increase in humidity has been applied to a subarctic winter profile in Fig. 2c, and the impact is much smaller because in a colder atmosphere, a given increase in relative humidity translates to a smaller increase in absolute humidity and optical depth.

The impact of clouds on the LW SARB, coupled with uncertainties in retrieving the geometric thickness of clouds with a passive satellite observation, poses a formidable obstacle to CERES. We have attempted to assess the consequences of such uncertainties with ISCCP C1 data, using in this case the Wang et al. (1991) LW code. ISCCP C1 bins retrieved clouds into 1 of 7 fixed vertical layers. In each of the 280-km by 280-km equivalent area gridboxes used by ISCCP, we have calculated the LW SARB every 3 hours for October 1986. The cloud forcing (i.e., Charlock and Ramanathan 1985) of the LW cooling rate profile is negative in our assumed, 50-hPa thick, cloud-free boundary layer from pole to pole in Fig. 3a. The monthly and zonally averaged cloud forcing exceeds 1 deg K/day in portions of the extratropics. ISCCP does not provide information on cloud overlap. For Fig. 3a, we have used non-overlapping "thick" clouds, which are idealized in Fig. 4a. A "thick" cloud fully occupies 1 of the 7 fixed vertical layers (50-180 hPa, 180-310 hPa, 310-440 hPa, 440-560 hPa, 560-680 hPa, 680-800 hPa, and 800-950 hPa). In Fig. 3b, the difference of the cooling rate for non-overlapping thick clouds (idealized in Fig. 4a) and randomly overlapping thick clouds (idealized in Fig. 4b) is substantial, exceeding the mean cloud forcing (Fig. 3a) in some areas. In Fig. 3c, the difference of two non-overlapping cloud-forced cooling rates are again compared, but here the difference is for thick clouds (Fig. 4a) and "thin" clouds (Fig. 4c); for the "thin" clouds, the cloud pressure thickness has been reduced by 50%. The effect of maximum overlap (idealized in Fig. 4d) is even more substantial as shown in Fig. 3d, which gives the difference in the cloud-forced cooling rate for non-overlapping thick and maximum overlapping thick clouds.

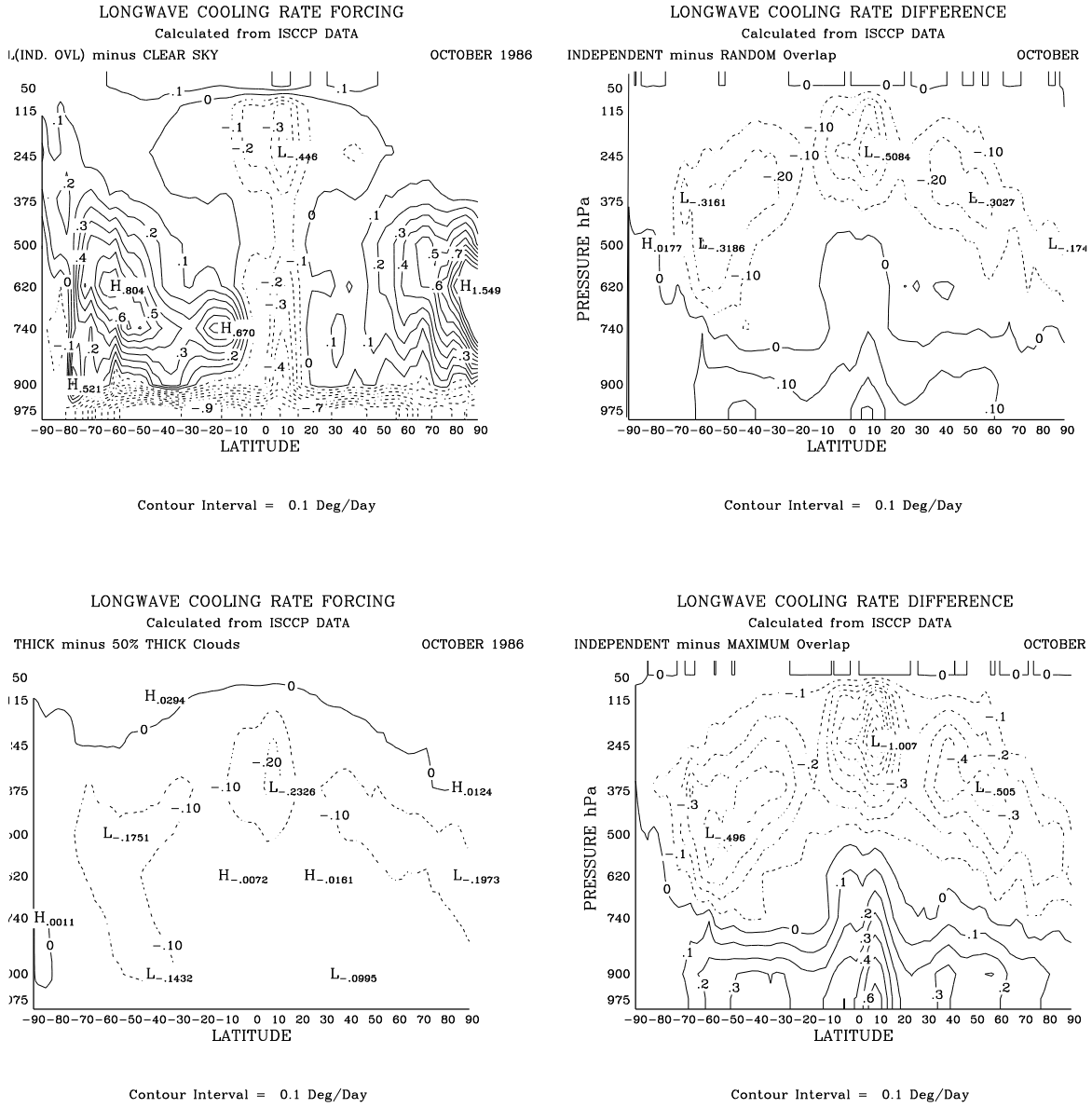


Figure 3 Zonal average of cloud forcing of the LW cooling rate (deg K/day) in upper left (a) fo non-overlapping thick clouds, in upper right (b) for the difference of non overlapping thick clouds minus randomly overlapping thick clouds, in the lower left (c) for the difference of geometricaly thick clouds minus thin clouds, and in the lower left for the difference of non-overlapping thick clouds minus maximum overlap thick clouds.

Despite the uncertainty in the LW cloud forcing to the SARB (Fig. 3a) which is induced by overlap (Figs. 3b and 3d) and geometric thickness (Fig. 3c) at some levels, we note a broad region, centered around 700 hPa, where the integrated lower tropospheric cooling rate is not strongly sensitive to cloud overlap or thickness. Improved estimates of cloud overlap and thickness will be provided by the CERES Cloud Working Group.

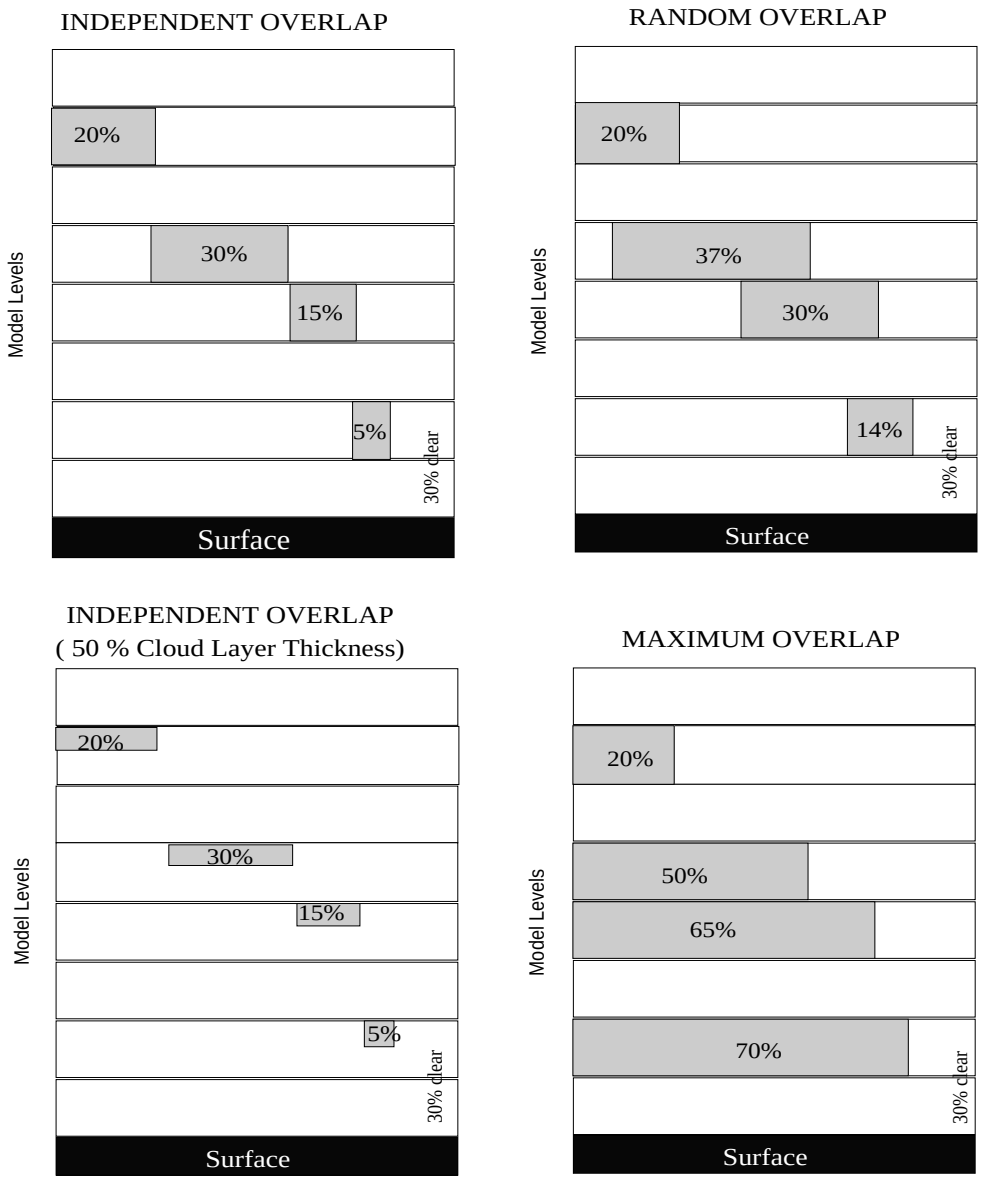


- Cloud Fraction viewed from SPACE is the same in all cases.

Figure 4 Idealization of overlap schemes applied to ISCCP cloud data for calculations of LW cooling rate. In upper left panel (a) for non-overlapping (independent) thick clouds, in the upper right for (b) randomly overlapped thick clouds, in the lower left (c) for non-overlapping thin clouds, and in the lower right (d) for maximum overlap thick clouds.

The LW SARB calculations in Fig. 1c-d and Fig. 3a-d have assumed that the LW radiation from a cloud is black. The Fu and Liou (1993) code accounts for LW scattering and non-black absorption and emission by clouds, and we now use that code to illustrate the importance, in certain cases, of those effects. Fig. 5a shows cloud forcing to DLF (CFdlf) and cloud forcing to OLR (CFolr) for a cloud located 800-850 hPa, as a function of the natural logarithm of the cloud liquid water content (LWC in gm-3). A code that does not explicitly account for non-black clouds would commonly treat a non-black cloud as an effective area fraction of a black cloud. The effective fraction (EF) can be determined from TOA fluxes as

EF = CFolr(cloud)/CFolr(optically thick cloud)

The EF would then be used to determine the cloud's impact on the LW SARB, by treating any cloud forcing as an EF of the cloud forcing for an optically thick cloud. Fig. 5b repeats the CFdlf from Fig. 5a, but it also shows an estimated CFdlf based on the EF above. In some cases, the estimated CFdlf errs by 5 $Wm^{-2}$. This error in the estimated CFdlf shows that, in some cases, one must explicitly account for LW scattering by clouds to provide an accurate determination of the LW surface budget. LW scattering by clouds can also have an impact on fluxes aloft, altering the cooling rate profiles given by the "black cloud, no scattering" assumption used in Fig. 1c-d and Fig. 3a-d.

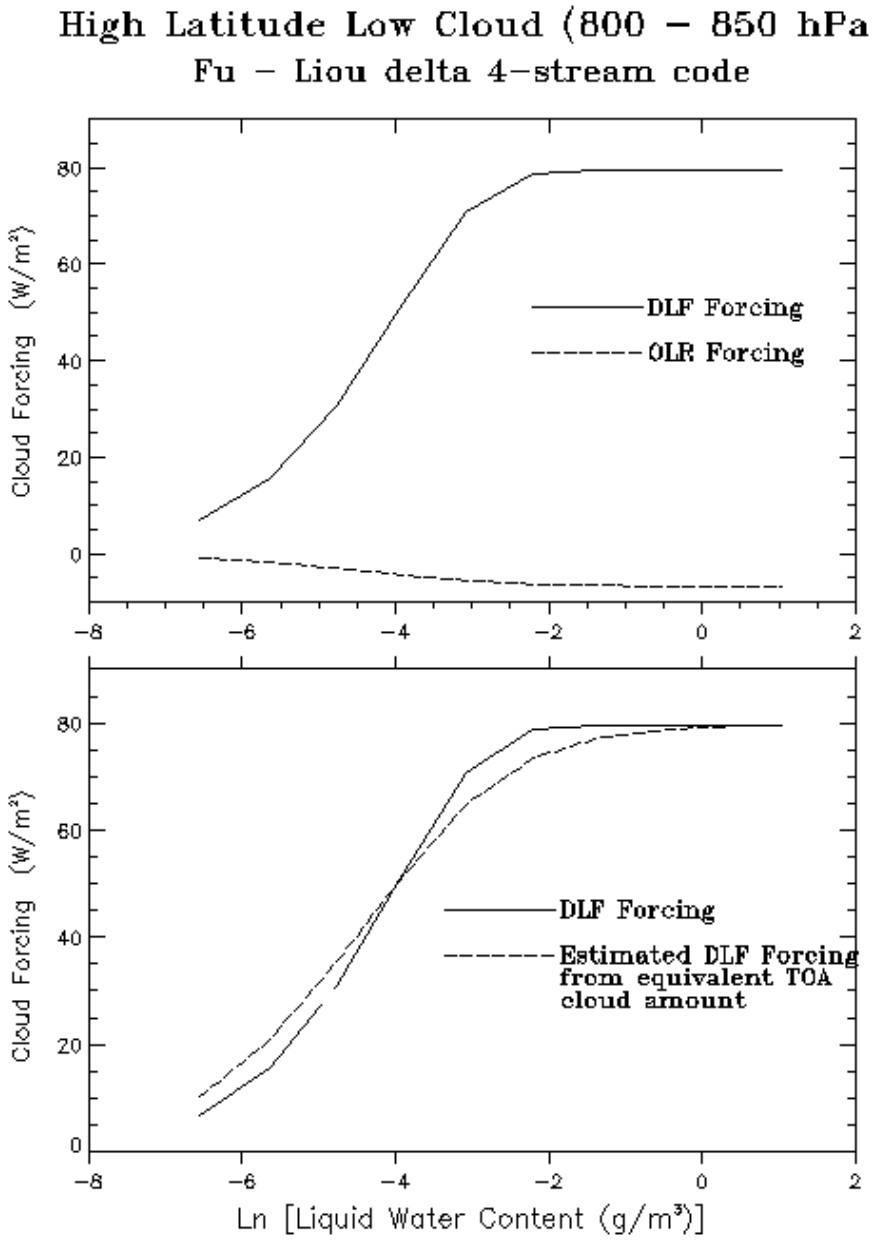


Figure 5 - LW cloud forcing to OLR (TOA) and DLF (surface) as function of cloud liquid water content (a) Directly computed OLR and DLF cloud forcing (b) Estimated DLF cloud forcing from equivalent TOA cloud amount

LW scattering by the surface is most significant over land. Surface emissivity can fall well below 0.90 over some dry, unvegetated soils (Salisbury and D'Aria, 1992). For a fixed atmospheric sounding and a fixed value for the clear sky OLR, there is a corresponding theoretical family of surface skin temperatures and surface broadband LW emissivities; the surface net LW flux is not uniquely determined by the atmospheric sounding and OLR alone. With the Fu and Liou (1993) code and a fixed midlatitude sounding, a clear-sky OLR of 280 $Wm^{-2}$ is consistent with both case A (skin temperature of 291 K; emissivity 1.00) and case B (skin temperature 296 K; emissivity 0.85). The surface net LW in cases A and B differ by 12 $Wm^{-2}$.

**5.3.1.3 SW issues.** The SW heating of the atmosphere, like the LW cooling, is sensitive to variations in humidity and cloud opacity. In the SW, however, clouds primarily scatter radiation (rather than absorb), and their impact on the SW surface budget is not as strongly dependent on cloud altitude as is the LW. Li et al. (1993) have noted that, for a given solar zenith angle (SZA), there is an approximately linear relationship between the SW reflected flux at the TOA and the SW net (absorbed) flux at the surface. Such a relationship permits the ready estimation of surface fluxes from CERES and ERBE TOA observations. The Li et al. (1993) algorithm is used in another component of the CERES processing stream for the determination of SW "surface net only" fluxes.

Here, we have calculated the reflected TOA and net surface fluxes with the Fu and Liou (1993) code in order to illustrate the Li et al. (1993) relationship. The thin solid lines in Fig. 6 have each been calculated for fixed solar zenith angles using various optical depths for a cloud at 800 hPa, and they are quite linear. The linearity is somewhat surprising, but it is not universal. The thick lines of Fig. 6 show the same relationship for two fixed solar zenith angles, but with a cloud at 200 hPa. The relationship for 200 hPa is again approximately linear. We note that it is important, however, to distinguish the case with a low cloud (800 hPa) and a high cloud (200 hPa). Cloud altitude must be accounted for, to place the SW heating at the right vertical level in the atmosphere. The different slopes of the thin (800 hPa cloud) and thick (200 hPa cloud) lines also show that cloud altitude must be taken into account, in order to improve the estimate of SW surface fluxes as well.

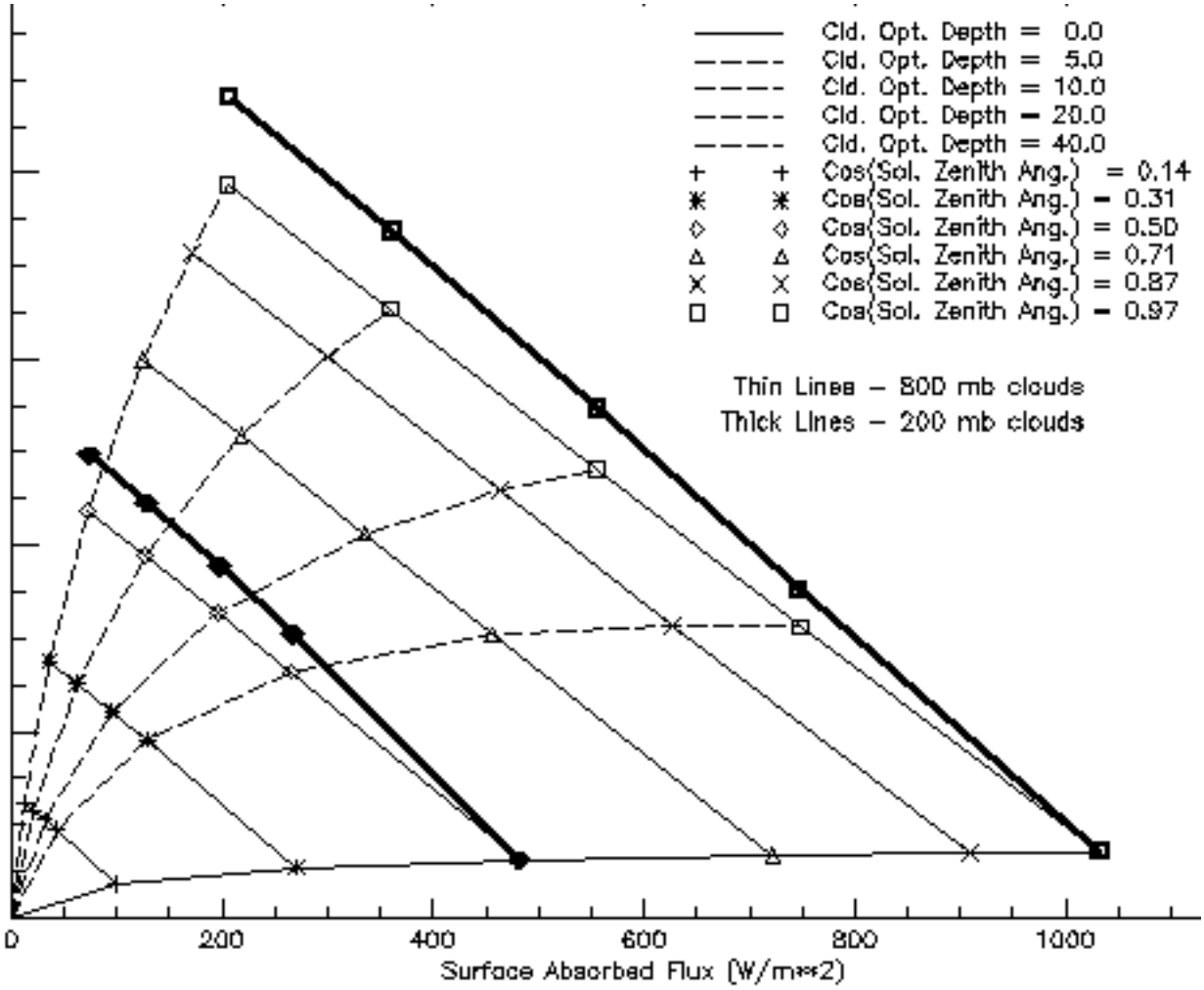


Figure 6 Computed SW reflected flux at TOA and SW surface absorbed (net) flux. Lines sloping downward to right are calculated for a constant solar zenith angle with varying cloud optical depth. Thin lines for cloud at 800 hPa. Thick lines for cloud at 200 hPa.

Ramaswamy and Freidenreich (1992) have studied the effect of the spectral overlap of absorption by water vapor and water droplets on the SW SARB. Most broadband codes are not adequate in their treatments of the spectral overlap, which is influenced by the distribution of water vapor above and within clouds. The corresponding errors in cloud-induced SW atmospheric heating can exceed 35%. The essence of the problem is the lack of effective spectral resolution for cloud single scattering albedo in the broadband radiative transfer codes. Ramaswamy and Freidenreich (1992) have developed a parameterization that partly accounts for the spectral overlap. We are approaching this problem in collaboration with Dr. Liou at the University of Utah. A high resolution code has been developed, and we hope to use simulations with it to guide a subsequent version of the Fu and Liou (1993) code.

Recent comparisons of computed and measured SW fluxes have led to doubts concerning radiative transfer in both clear (Wild et al., 1995; Kato et al., 1996; Kinne et al., 1996) and cloudy (i.e., Cess et al., 1995) skies, wherein the atmosphere appears to absorb considerably more SW than is predicted by models. In contrast, other careful studies have not found discrepancies between calculations and measurements for clear skies in the tropics (Chou and Zhao, 1996) or have not found evidence of "enhanced" SW absorption by clouds (Hayasaka et al., 1995).

Tables 2 and 3 illustrate the CAGEX Version 1.1 bias in SW flux computed with the Fu and Liou (1993) code, the Minnis et al. (1993) LBTM GOES-7 cloud retrievals, and aerosol spectral optical depth from the MFRSR (Harrison et al., 1994). BSRN-like surface radiometric measurements were available at the ARM SGP site (DeLuisi, 1991), including point measurement of surface albedo (which we applied to the entire gridboxes). The temporal domain consists of 26 days in April 1994 with 18 half-hourly comparisons per day. The spatial domain is a 3 by 3 grid ($0.3^o$ on each side) for satellite (TOA) data, but only the central gridbox for the surface radiometric measurements (Fig. 0). The mean TOA downwelling (DWN) was almost 1000 $Wm^{-}2$ for both the total-sky and clear-sky domain. For clear skies, the computed fluxes for surface downwelling (SFC DWN in Table 2) are 27.5 $Wm^{-2}$ greater than the measurements. The inferred biases in atmospheric absorption (ATM ABS) are comparable for total sky (-40.8 $Wm^{-2}$) and clear sky (-29.1$Wm^{-2}$) conditions, here suggesting a problem with enhanced clear sky absorption, as opposed to cloud forcing.

Table 2 SW Statistics (W/m**2) for CAGEX - Version 1.1 (April 1994)

| **FULL SKY** | Average | | Bias | Error (%) | Samples (number) |
|---|---|---|---|---|---|
| | Calculated | Measured | | | |
| SW TOA NET | 584.8 | 602.9 | -18.2 | -3.0 | 4059 |
| SW TOA UP | 386.6 | 368.5 | 18.2 | 4.9 | 4059 |
| SW TOA DWN | 971.4 | 971.4 | 0.0 | 0.0 | 4059 |
| SW TOA ALB | 0.400 | 0.380 | 0.020 | 5.2 | 4059 |
| SW ATM ABS | 170.4 | 211.3 | -40.8 | -19.3 | 330 |
| SW SFC NET | 403.6 | 379.2 | 24.4 | 6.4 | 330 |
| SW SFC UP | 96.9 | 93.8 | 3.1 | 3.3 | 402 |
| SW SFC DWN | 487.3 | 461.1 | 26.2 | 5.7 | 361 |
| SW SFC DIR | 245.1 | 280.4 | -35.2 | -12.6 | 361 |
| SW SFC DIF | 240.1 | 177.8 | 62.3 | 35.1 | 348 |
| LW TOA OLR | 237.3 | 234.9 | 2.4 | 1.0 | 4039 |
| LW SFC NET | -62.1 | -65.9 | 3.8 | -5.7 | 330 |
| LW SFC UP | 388.2 | 400.2 | -12.1 | -3.0 | 402 |
| LW SFC DWN | 325.0 | 332.8 | -7.8 | -2.4 | 361 |

| **CLEAR SKY** | Average | | Bias | Error (%) | Samples (number) |
|---|---|---|---|---|---|
| | Calculated | Measured | | | |
| SW TOA NET | 779.4 | 785.1 | -5.8 | -0.7 | 861 |
| SW TOA UP | 195.2 | 189.5 | 5.8 | 3.0 | 861 |
| SW TOA DWN | 974.6 | 974.6 | 0.0 | 0.0 | 861 |
| SW TOA ALB | 0.204 | 0.198 | 0.007 | 3.4 | 861 |
| SW ATM ABS | 150.3 | 179.5 | -29.1 | -16.2 | 55 |
| SW SFC NET | 651.1 | 627.6 | 23.5 | 3.7 | 55 |
| SW SFC UP | 149.2 | 143.7 | 5.5 | 3.8 | 80 |
| SW SFC DWN | 802.3 | 774.8 | 27.5 | 3.5 | 55 |
| SW SFC DIR | 674.8 | 669.4 | 5.3 | 0.8 | 55 |
| SW SFC DIF | 127.5 | 105.3 | 22.3 | 21.2 | 55 |
| LW TOA OLR | 279.0 | 276.7 | 2.4 | 0.9 | 861 |
| LW SFC NET | -109.7 | -118.5 | 8.8 | -7.4 | 55 |
| LW SFC UP | 384.0 | 411.1 | -27.1 | -6.6 | 80 |
| LW SFC DWN | 271.7 | 289.6 | -17.9 | -6.2 | 55 |

The critereon used to identify clear-sky conditions affects the reported clear-sky bias reported in Table 2. Clear sky conditions have been identified alternately with a more relaxed critereon, labled "test 1" in Table 3. The relaxed clear-sky critereon of test 1 assumes that the LBTM satellite retrieval finds no clouds in the central gridbox for a *single snapshot* centered in the half hour interval of the flux measurement. For test 1 (Table 3), the computed direct beam to a horizontal surface is biased 16.0 $Wm^{-2}$ higher than the measurement (normal incident pyrheliometer NIP multiplied by the cosine of the the solar zenith angle). We applied a stricter critereon ("test 2") in Table 2, and thereby reduced the bias in the direct beam from 16 $Wm^{-2}$ (test 1 in Table 3) to 5.3 $Wm^{-2}$ (test 2 in Table 3). Successively more rigorous screening for clear sky conditions are applied. In test 2, the satellite reports no cloud in the central gridbox for a snapshot within the measurement half hour, and none for the half hours earlier or later. In test 3, we use test 2 plus no clouds in any of 8 adjacent gridboxes for the measurement half hour. In test 4, we use test 3 plus continuous MicroPulse Lidar (MPL; Spinhirne, 1993) cloud screening of the zenith for the half hour interval of the flux measurement. For tests 2-4, the bias in the clear sky diffuse beam is approximately 20%. The bias in the total beam, as measured by combining the NIP and an unshaded pyranometer, is robust. We have not been able to resolve these biases by using a different radiative transfer code (Chou, 1993 and MODTRAN3), by comparing with alternate ARM surface measurements of flux, by reasonable changes in the aerosol optical thickness or absorption, or by using an alternate sounding for water vapor (the Mesoscale Atmospheric Prediction System MAPS from NOAA Forecast Systems Laboratory). For the surface fluxes in LW, however, the biases in Table 2 are considerably reduced when re-computed with MAPS sounding data (see CAGEX on-line tables for details).

Table 3 SW Statistics (W/m**2) for Clear Skies Surface Downwelling (SFC DWN)

| Test | Direct Bias | Total (direct + diffuse) bias | Samples |
|---|---|---|---|
| 1 | 16.0 | 30.8 | 89 |
| 2 | 5.3 | 27.5 | 55 |
| 3 | 2.5 | 26.4 | 42 |
| 4 | 6.8 | 28.1 | 25 |

Tests:
1) LBTM cloud fraction = 0
2) 1), + LBTM fx=0 during 1/2 hour before and 1/2 hour after time
3) 2), + LBTM fx=0 in all 9 grids (applies to center grid only)
4) 3), + lidar temporal fx=0 (applies to center grid only)

Preliminary comparisons by CERES (Alberta et al., 1997) and other groups are similar for clear skies using data from the ARM Enhanced SW Experiment (ARESE), which was conducted in October 1995. To deduce the clear sky insolation, we have used a combination of the NIP and a shaded pyranometer, as specified by WCRP. Commonly stated measurement accuracies for well-maintained instruments are 1% for the NIP and 3-5% for pyranometers. A recent test of NIP instruments with a cavity radiometer at ARM SGP CART by Michalsky et al. (1997) found that the NIP referred to as "BSRN" read too low by 1%, while the a "SIROS" NIP read too low by almost 3%. In the domain of the ARM SGP CART site, we have not resolved code versus measurement discrepancies or instrument versus instrument discrepancies, even using the new radiometers from the Atmospheric Research Laboratory at Scripps (Valero et al., 1996). We may be facing an unexpected sum of errors due to broadband radiative transfer approximations, instrument operation and calibration, and inadequate sensing of atmospheric composition. CERES is attempting to stay abreast of developments in this fast-paced area with the on-line CAGEX activity (http://snowdog.larc.nasa.gov:8081/cagex.html). Some of the latest figures and tables are in Section 5.5 Strategic Concerns.

A number of researchers (including J. J. Morcrette at ECMWF, H. Leighton at McGill, and R. Stuhlmann at GKSS) have confirmed our reported clear sky SW insolation bias with independent radiative transfer calculations based on CAGEX Version 1.0 April 1994 files. Our preliminary clear sky insolation biases for October 1995 are consistent with independent calculations (not based on CAGEX) by respectively, S. Kinne and associates at NASA Ames, and S. Kato and T. Ackerman at Penn State.

### 5.3.2 Framework of CERES Calculations

**5.3.2.1 Some definitions.** CERES calculations for the SARB are performed at the footprint (also called Field Of View FOV) scale of the broadband ERB measurement of the same TOA flux by ERBE (Release 1) and CERES (Release 2 and onward). For ERBE, the minimum footprint (FOV) at nadir was about 30 km.

The Meteorlogy, Ozone, and Aerosol (MOA) sounding data for the SARB calculation is based on the NCEP Reanalysis for Release 1 and on the NASA Goddard Data Assimilation System ( DAS) or on NCEP for Release 2. The Subsystem 12 documentation describes MOA, which is referenced in Appendix A (Input Data Products) of this Subsystem 5 document. At present in Release 1, the 6-hourly NCEP Reanalysis is interpolated by MOA to the nearest hour of the CERES grid ($1.25^o$ in Release 1 and $1^o$ in Release 2) in 58 vertical levels. In the Release 1 calculations shown later in this document, the MOA ozone column loading was obtained from the October 1986 ISCCP/TOVS. Release 2 ozone will be based on the the vertical profiles from the NCEP Stratospheric Monitoring Group Ozone Blended Analysis (SMOBA), which are based on measurements from the height resolving SBUV/2, a nadir instrument. The aerosols in MOA are described at the end of the following section (5.3.2.1).

The cloud optical properties for the SARB calculations are produced by AVHRR (Release 1), VIRS (Release 2), or MODIS (Release 3) high resolution cloud imager pixels. The CERES convention distinguishes high resolution cloud imager *pixels* from the coarser resolution ERB *footprint* or FOV. Subsystem 4 produces an instantaneous Single Satellite Footprint, TOA and Surface Flux, and Clouds (SSF) product for each ERB footprint. Appendix A (Input Data Products) of this document lists the many SSF parameters. The cloud optical property retrievals on the footprint-scale SSF product have been adjusted with the appropriate ERB Point Spread Function (PSF). Instrument response is not uniform across the ERB footprint, and the PSF provides the appropriate spatial weighting for cloud imager products within the footprint. SSF contains the broadband TOA measured flux for the footprint and estimates for the surface LW (Inamdar and Ramanathan, 1994) and surface SW (Li et al., 1995) from fast surface-only retrieval algorithms. The cloud properties and broadband TOA flux are used in the Fu and Liou (1993) calculations for the entire vertical profile as described in this document.

As potential input manifests for the Fu and Liou (1993) code, the MOA (sounding) and especially the SSF (cloud property) listings in Appendices are ponderous for the reader. CERES Appendices are keyed to Release 2. The Release 1 calculations presented here are based, however, on the limited subset of FOV-scale SSF data in Table 4.

Table 4 SSF parameters for Release 1 radiative transfer calculations

| SSF | Description of parameter |
|---|---|
| | |
| 7 | Earth-Sun distance |
| | |
| 3 | Colatitude of satellite at observation |
| 4 | Longitude of satellite at observation |
| 23 | CERES(ERBE) solar zenith at TOA |
| 39 | CERES(ERBE) SW flux at TOA, upwards |
| 40 | CERES(ERBE) LW flux at TOA, upwards |
| 52 | CERES(ERBE) spectral reflectivity *(from references in 5.3.2.2 below)* |
| 54 | CERES(ERBE) LW surface emissity *(from references in 5.3.2.2 below)* |
| 56 | Imager based surface skin temperature |
| | |
| | *The following parameters are arrays of cloud categpories (4 categories, or kinds of clouds, are allowed per FOV in Release 1 only 2 categories are allowed per FOV in Release 2):* |
| | |
| 77 | Cloud category percent coverage |
| 84 | Mean logarithm of cloud visible optical depth |
| 96 | Mean cloud effective temperature |
| 102 | Mean water particle radius |
| 104 | Mean ice particle effective diameter |
| 106 | Mean cloud particle phase |

The descriptions of header parameter 7 and parameters 4, 23, 29, 39, and 40 in Table 4 should be adequate. The reference values for surface spectral reflectivity (52 in Table 4) and LW surface emissivity (53 in Table 4) are described in the following section 5.3.2.2.

When the cloud imager indicates clear conditions for an ERB footprint (Subsystem 4 documents), a surface skin temperature is retrieved (parameter 56 in Table 4). The Release 1 CERES skin temperature retrieval is based on AVHRR 11 μm radiance, the satellite view angle, and the precipitable water (PW). Preliminary studies indicate that the OLR computed with this satellite-based skin temperature is more suitable over land than the model output from DAS. For cloudy skies, we use DAS for skin temperature. Over the oceans, this is essentially the NOAA Climate Analysis Center (CAC) SST (Reynolds and Smith, 1994). The bucket (CAC) SST is close to the sea skin temperature in most cases, excepting clear skies and light winds.

The cloud parameters in Table 4 are unique to the CERES experiment: cloud properties based on high resolution imager pixels fitted to a larger broadband ERB footprint. Each cloudy pixel is grouped according to a "cloud category" (Table 4). The cloud categories in CERES are high (H; effective pressure < 300 hPa),

upper-middle (UM; 500 hPa > effective pressure > 300 hPa), lower-middle (LM; 700 hPa > effective pressure > 500 hPa), and low (L; effective pressure > 700 hPa). All Release 1 radiative transfer calculations described in this Subsystem 5 document are performed at the cloud category scale within a footprint, rather than at the higher resolution individual cloud pixel scale. In Release 1, a single ERB footprint may contain clear sky and as many as all 4 cloud categories. For a footprint, Release 1 radiative transfer may be run for as many as 5 cases (one clear and 4 cloudy). There is no cloud overlap in Release 1 (i.e., no footprints with H cloud overlapping, or sitting directly on top of, L cloud). The planned Release 2 will permit cloud categories to overlap within a large ERB footprint. However, Release 2 will permit only up to 2 (of the possible 4) cloud categories per footprint. For a footprint, Release 2 radiative transfer may be run for as many as 4 cases (one clear, 2 cloud categories, and one overlapped condition of the 2 cloudy categories).

For each cloud category (H, HM, LM, or L) in the large ERB footprint, the percent area of the cloud category is given with the category means for the logarithm of cloud optical thickness, the cloud effective temperature, the liquid particle radius, the ice particle radius, and phase. With the visible optical depth, particle size, and phase, we determine the liquid water path (LWP in $gm^{-2}$) or ice water path (IWP) for the cloud category. The cloud geometrical thickness is then estimated in Subsystem 5 using an empirical relationship between geometrical thickness and visible optical depth devised by Minnis et al. (1993a-b). From the cloud effective temperature (near the cloud top) and the MOA sounding profile, we determine the cloud top pressure for input to the Fu and Liou (1993) code. The cloud top pressure, estimated geometrical thickness of the cloud, and the MOA sounding are used to determine the cloud base pressure. The LWP is then distributed homogeneously as a LWC (liquid water content in $gm^{-3}$) from cloud top to cloud bottom.

Subsystem 4 retrievals identify each cloudy pixel as ice or liquid. This yields the mean cloud particle phase for each cloud category (parameter 106 in Table 4). The present Subsystem 5 regards an individual cloud category as all liquid or all ice, from cloud top to cloud base, according to the mean cloud particle phase. It is recalled that with the Fu and Liou (1993) broadband code, we treat ice particles as hexagonal cylinders and account for their sizes.

Cloud top and bottom are floating layers as shown in Fig. 7. Cloud top and bottom are assigned to their exact pressure levels for the radiative transfer calculation. Most of the other levels are fixed, with the exception of the floating boundary layers of thickness 10 hPa and 20 hPa. When the surface rises (or when the surface pressure falls), the thickness of the layer immediately above the 20 hPa boundary either expands or contracts; as it moves upward, it successively entrains the fixed levels by eliminating the bottoms of the fixed levels. Fig. 7 shows two overlapping cloud categories, as is possible in the planned Release 2, and for which we here have the maximum number (34) of permitted levels. For Release 1 (2) the 58-level sounding data from MOA has been (will be) interpolated into a coarser vertical grid.

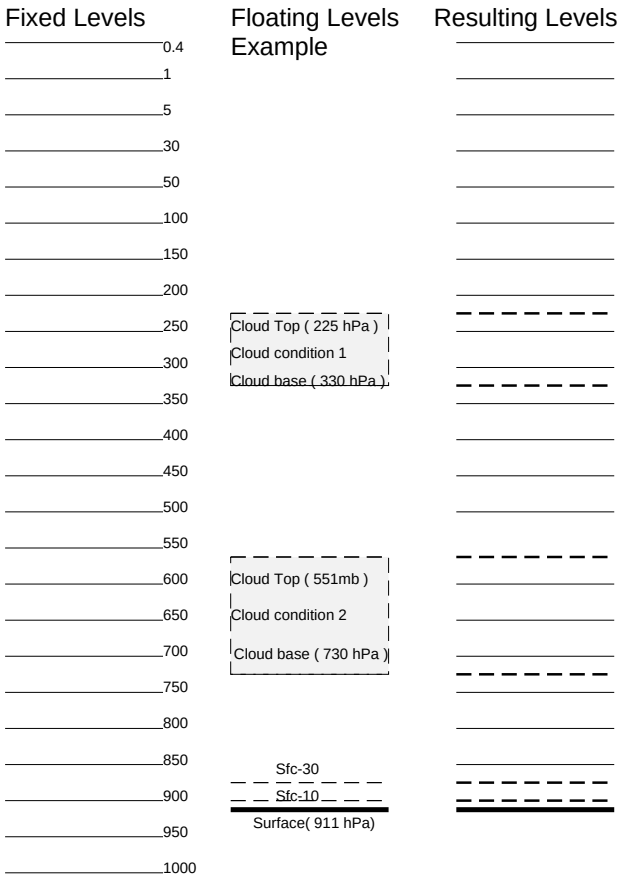


Figure 7 - Fixed and floating (terrain, boundary layer, clouds) levels

**5.3.2.2 Reference Optical Properties of Aerosols and Surfaces.** The uncertainty to anthropogenic climate forcing posed by aerosol and surface optical properties has been noted. CERES Releases 1 and 2 address both problems to first order, by solving for the aerosol optical depths and broadband surface albedos which are most consistent with observed TOA broadband fluxes and available ancillary data. To approach such first order problems globally, procedures are needed to estimate "second order" effects used in the calculations.

A set of reference optical properties is needed for aerosols and surfaces. The reference optical properties are used in the initial, unconstrained radiative transfer calculations. A subset of the optical properties, the aerosol optical depth and surface albedo/reflectance, are subsequently constrained (adjusted) in some footprints. In Release 1 and Release 2 calculations, the only aerosol parameter provided to Subsystem 5 (SARB) is the optical depth in the visible. Reference optical properties are used to scale the aerosol visible optical depth throughout the 6 SW and 12 LW spectral intervals of the Fu and Liou (1993) code; to distribute the optical depth among the vertical layers; to specify the single scattering albedo and asymmetry factor of the aerosol in each wavelength band for the calculation. In Release 1 and 2, the reflectance of the surface must be specified for the same 6 SW and 12 LW spectral intervals.

Both the aerosol visible optical depth and the surface reflectance may be adjusted (constrained) after the first radiative transfer calculation. But if the aerosol optical depth is constrained in the visible, this is simply scaled into proportional changes in the other bands; the optical depth scales up or down by a factor that is constant with wavelength. The single scattering albedos and the asymmetry factors are not constrained for

any wavelength intervals at present. When the reflectance of the surface is constrained to produce a surface albedo needed for energy balance constraints, the reference spectral shape of the surface reflectance is retained.

The d'Almeida et al. (1991) compilation furnishes a global climatology, based on external mixtures, of 12 aerosol types. Importantly, the compilation includes the relative humidity dependence of aerosol optical properties (Fig. 8). This compilation was approved by J. Lenoble as President of the Radiation Commission of the International Association of Meteorology and Atmospheric Physics (IAMAP). One of the co-authors, E. Shettle, has advised CERES that another compilation is under development. We use 2 of the 12 d'Almeida et al. (1991) types in Release 1: clean continental for land and clean maritime for sea. For subsequent Release 2 processing in 1997, additional d'Almeida et al. (1991) aerosol types will be used. Release 2 cloud retrieval algorithms (Subsystem 4) include provision for the identification of smoke for clear sky footprints. The optical properties of smoke will be assumed from the d'Almeida et al. (1991) urban aerosol. Further in the post-launch time frame (Releases 3 and 4), we plan to generate models for aerosol optical properties using Mie routines provided by S.-C. Tsay and run by CERES colleague Yong-Xiang Hu; these will eventually replace some of the d'Almeida et al. (1991) models.

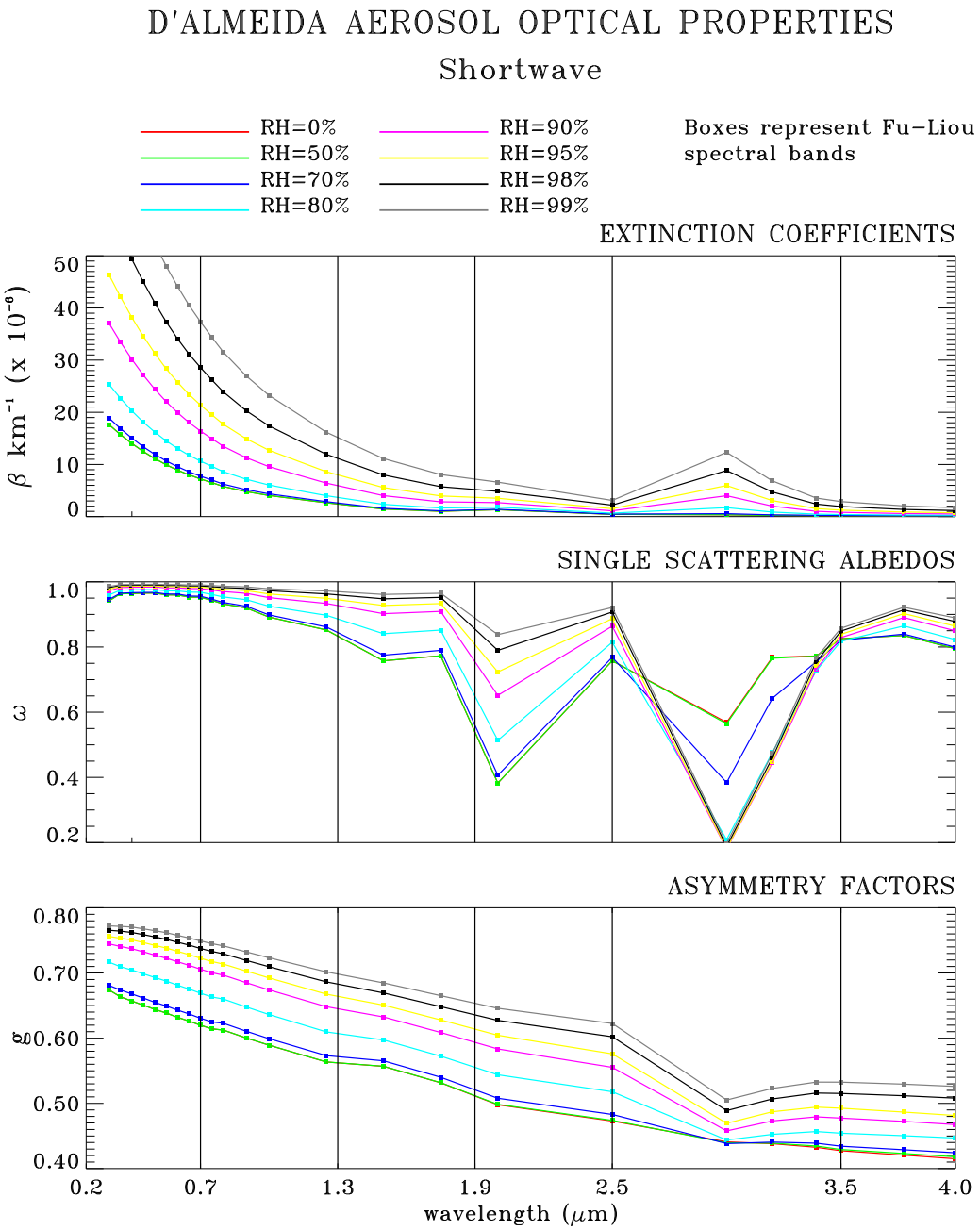


Figure 8 - Variation of d'Almeida aerosol properties with relative humidity and wavelength

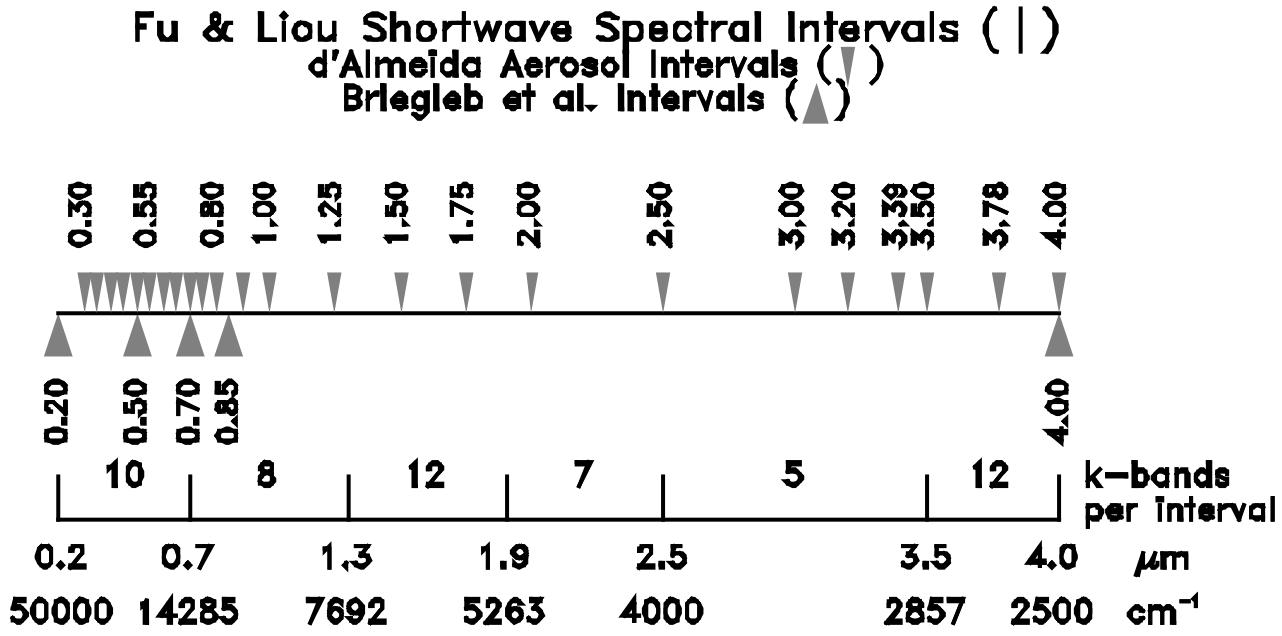


Figure 9 - SW spectral intervals for radiative transfer calculations, reference aerosol properties, and reference surface properties

A formal interpolation routine is used to distribute optical properties from the wavelength bands of the d'Almeida et al. (1991) compilation to the Fu and Liou (1993) spectral intervals. For a standard atmosphere and solar zenith angle of $60^{o}$, the surface insolation has been calculated at high resolution with the MODTRAN3 program using 8-point Gaussian quadrature. Optical properties in each d'Almeida et al. SW band were assigned as spectrally flat across the large number of MODTRAN3 intervals for the d'Almeida bands (Fig. 9). From the tight MODTRAN3 intervals, the optical properties were assigned to the coarser Fu and Liou (1993) SW bands, with a further refinement to account for the new splitting of the 0.2-0.7 μm into 10 sub-intervals . For clear sky conditions, the transfer algorithm for spectral interpolation was found to have surprisingly small dependence on SZA and the atmospheric sounding. The corresponding spectral intervals for the LW are shown in Fig. 10.

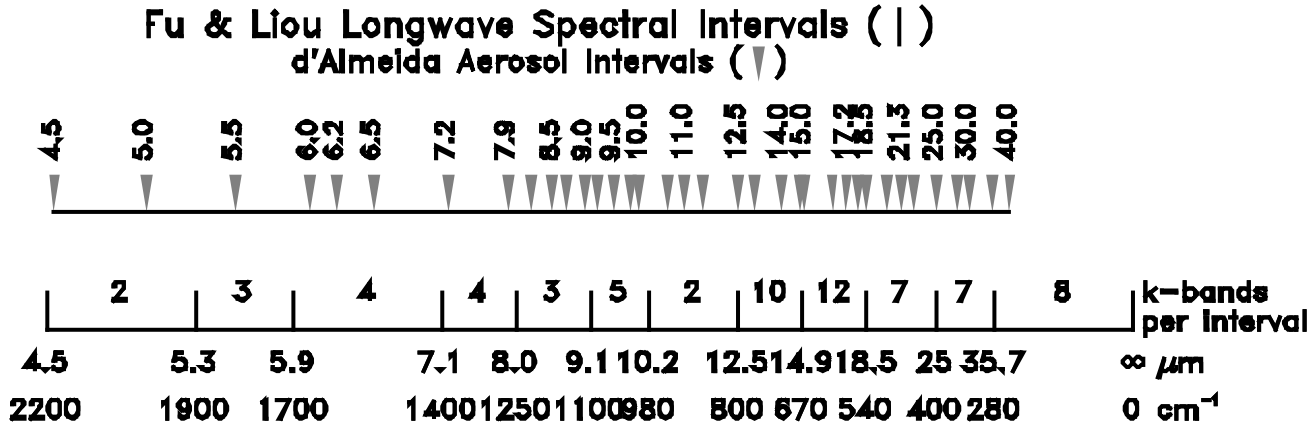


Figure 10 - LW spectral intervals for radiative transfer calculations, reference aerosol properties, and reference surface properties

Release 1 distributes the d'Almeida et al. (1991) aerosol with height using the provisional analytical model of Spinhirne (1991) for the smooth background component of aerosol scattering. In Release 2, a more sophisticated (but still provisional) height distribution model by Spinhirne et al. (1997) will be used. Release 2 will include a switch permitting the insertion of large optical thicknesses of aerosol in the stratosphere to simulate the effects of a volcanic eruption.

Aerosols in Releases 1 and 2 have default visible optical depth climatologies for the integrated total column. The algorithms based on d'Almeida et al. (1991) and Spinhirne (1991) are applied to column optical depths and distribute aerosol properties with wavelength and altitude. The default optical depths are the only total column optical depths available in Release 1. The default optical depths are used as a first guess, in the event that other input data is not available, in Release 2. In Release 2, CERES Subsystem 4 will retrieve, for clear-sky footprints over the seas, the column optical thickness of aerosols with the Ignatov et al. (1994) algorithm due to CERES Co-I L. Stowe. For the seas, the visible aerosol optical depth climatology based on the Ignatov et al. (1994) AVHRR-based retrievals for October 1989 is used. For the visible aerosol optical depth land climatology, Releases 1 and 2 use the Pinker and Laszlo (1992) estimation from the GEWEX SRB Project.

The reference optical property map for surfaces can be found on a web page (http://tanalo.larc.nasa.gov:8081/surf_htmls/SARBdscpt.html) developed by David A. Rutan. We are aware that whatever optical property we specify for a given spot, a local expert is liklely able to provide a more accurate one. The CERES SARB surface optical property web page is intended as a tool for communicating with such parties. The present web page has "point and click" maps, giving the classisfication of surface type, the assumed spectral relectance in the 6 SW bands of the Fu-Liou code, and the assumed broadband surface emissivity. Release 1 used this information in developing the Figures for this document. For Release 2, David P. Kratz and Shashi Gupta generated emissivities for all 12 LW bands of the Fu and Liou code.

The reference surface optical property map is stunted: high spatial resolution, modest spectral resolution, no seasonal data, and minimal angular information. The International Geosphere Biosphere Program (IGBP) land cover types are placed in a 10'x10' array for 17 types as evergreen needleleaf forest, evergreen broadleaf forest, deciduous needleleaf forest, deciduous broadleaf forest, mixed forest, closed shrubland, open shrubland, woody savanna, savanna, grasslands, permanent wetlands, croplands, urban, cropland/mosaic, snow and ice, barren, or water bodies. CERES has judiciously matched the 17 IGBP types with the spectral optical properties taken from the literature according to the classification of Table 5.

Table 5 Source of Spectral Optical Properties for Surfaces

| CERES/SARB Scene Type | Source of Spectral Curve |
|---|---|
| ---------- | ---------- |
| farm | Briegleb et al. (1986) |
| shrub | Briegleb et al. (1986) |
| meadow | Briegleb et al. (1986) |
| evergreen forest (needle leaf) | Briegleb et al. (1986) |
| mixed deciduous forest | Briegleb et al. (1986) |
| deciduous forest | Briegleb et al. (1986) |
| tropical evergreen forest (broad leaf) | Briegleb et al. (1986) |
| woodland | Briegleb et al. (1986) |
| desert | Briegleb et al. (1986) |
| tundra | Briegleb et al. (1986) |
| irrigated soil (rice) | Briegleb and Ramanathan (1982) |
| water | Bowker et al. (1985), Payne (1972) |
| permanent snow (ice) | Grenfell et al. (1984) |
| fresh snow | Bowker et al. (1985) |
| sea ice | no reference |

Table 5 is used to determine the *shape* of the spectral curve of surface reflectance in the SW. As with the aerosol spectral properties, an algorithm has been applied to apportion the spectral reflectance from the source (Table 5) to the 6 SW intervals of the Fu and Liou (1993) code.

Some of the Briegleb et al. (1986) surface types can be adjusted with a SZA-dependent canopy model (Dickinson, 1983) to estimate a spectral surface albedo.

$$A(\mu) = A(\mu o=0.5)\ [1 + d]/[1 + d\ \mu]$$

Appropriate d factors have been determined from ScaRab (Scanner for Radiation Budget) and ERBE data and placed on the aforementioned reference optical property home page. Rather than applying this canopy model as in Rutan and Charlock (1997), Release 1 estimated the broadband suface albedo itself from the broadband surface albedo retrieval technique of Staylor and Wilber (1990). The Staylor and Wilber (1990) surface albedo is based on the TOA SW ERB, the SZA, the column precipitable water, and the column ozone. The spectral shape from Table 5 was used with the broadband surface albedo of Staylor and Wilber (1990) to yield an estimate of spectral reflectance for the very SZA and footprint in question. The Staylor and Wilber (1990) retrieval is based on the large ERB footprint. For this large ERB footprint, the many 10'x10' spectral shapes that spatially comprise the footprint are convolved with the ERB Point Spread Function (PSF). The result for clear sky conditions is a set of 6 SW spectral reflectances for the footprint; broadband and directional aspects of the reflectances are determined from ERB measurement; relative spectral shape is determined from the literature.

If cloud cover within the ERB footprint exceeds 5%, the Staylor and Wilber (1990) techniuqe was not applied. For a cloudy footprint, Release 1 uses a total-sky surface spectral reflectance as determined by the 10'x10' gridbox in the center of the footprint. We plan to develop a short-term "memory" of surface relectance in

Release 2. This will permit an estimation of the SZA dependence of surface reflectance (through the above d factors) for footprints which are not clear, but which have been observed previously under clear conditions.

The surface LW emissivity map in Release 1 is broadband only. It is based on a matching of the laboratory data of Salisbury and D'Aria (1992) to the CERES grid. Typical broadband values are 0.98 for the ocean, 0.96 for much of the land, and 0.90 for all deserts. The value of 0.90 is probably too high for the Saraha. A small, focused study is planned to provide a better estimate of the emissivity for the Saraha in Release 2. This study will use October 1986 clear sky LW broadband *and AVHRR* simulations from the Fu and Liou (1993) code. The software to simulate the AVHRR channels with the Fu and Liou (1993) code is on hand, courtesy of Drs. Liou and Rao, and Kratz (1995) has developed correlated k's for these channels. A further modification will produce clear-sky *radiances* with the code. Simulated broadband and AVHRR radiances will be compared with ERBE and AVHRR measured radiances. Because the surface skin temperature is the same throughout the spectrum, a fit of simulated and measured radiances will permit the estimation of the effective broadband and AVHRR surface emissivities. Collaboration is also underway with the MODIS surface temperature group through David P. Kratz of the CERES "Surface-only" group.

### 5.3.3 Constrainment Algorithm

An objective constrainment algorithm (Rose et al., 1997) is used to adjust radiative transfer model inputs to obtain fluxes consistent with satellite-observed TOA fluxes. In this algorithm, random errors between the modeled and observed fluxes are reduced to a specified standard deviation. The random error for a single instantaneous footprint can be large, but we assume that the mean errors are small. The constrainment algorithm adjusts a selected set of model inputs within their assessed range of uncertainty. A set of initial, unconstrained broadband radiative transfer calculations, is made for each instantaneous footprint. The constrainment algorithm then uses these calculated fluxes and an additional database of pre-computed partial derivatives of fluxes. The partial deviatives of flux have been determined w.r.t. each radiative transfer model input parameter that is a candidate for adjustment. Simultaneous equations describing the flux errors, the mininimization of adjustment and minimization error are solved by the technique of Lagrange multipliers. Such techniques have been developed in the wide field of constrained optimization (Polak, 1971). The algorithm does not generate a unique solution for the SARB (Charlock et al., 1997).

The algorithm is flexible. In field expermients, the algorithm can constrain the column using various combinations of available measured fluxes, such as those from surface radiometers. Constrainment of model-calculated fluxes with satellite-observed fluxes ensures that the calculated, constrained estimate of the SARB is consistent with the observed fluxes at TOA. Consistency with TOA observed fluxes is sought for the ensemble mean of a large spatial and temporal domain with many samples. It must be recalled that for an individual ERBE or CERES footprint, a large error in the instantaneous flux is expected because of uncertainty in the ADM. The satellite observes the radiance at one angle, and this is used to estimate the flux from all angles. In ERBE, the instantaneous footprint standard errors for TOA flux have been estimated as 38 $Wm^{-2}$ for SW (daytime only) and 12.7 $Wm^{-2}$ for LW.

In CERES, these instantaneous TOA errors will be reduced, but not eliminated. Hence, an attempt to force an exact match of modeled and observed fluxes at every footprint would force an unrealistic over-adjustment of model input values. Noise in the radiometric inversion from radiance to flux would generate noise in constrained model input variables like cloud optical depth and humidity. To partially remedy this, we constrain a simultaneous match of one or more modeled fluxes to their observed counterparts within an allowed range of random error while minimizing the adjustment of the set of model inputs relative to their assessed uncertainty. A priori uncertainties are assigned to observed TOA fluxes, as well as to radiative transfer input parameters like cloud optical depth. The values of these a priori incertainties affect the constrainment process substantially. If large (small) a priori uncertainties are assigned to observed fluxes and small (large) a priori uncertainties are assigned to model input parameters, an individual constrained result will have a large (small) difference from the observed TOA flux and small (large) adjustments to the model input parameters.

The derivative tables used in the SARB constrainment algorithm are a set of off-line calculations showing the sensitivity of TOA LW and SW flux to perturbations of relevent adjustment variables. There are seperate tables and associated relevent variables for clear-sky LW, overcast LW, clear-sky SW, overcast SW. Each of these tables can be thought of as a sensitivity analysis for a wide range of variables that would be encountered globally for any meterological, surface or cloud "state". It is recognized that these tables can not encompass all variability of sensitivity, but it is hoped that they include the dominant variables under most scenarios.

Derivative Table "State" Variables:

1) Clear-sky longwave
   - Skin temperature
   - Precipitable water.
2) Overcast Longwave
   - Skin Temperature
   - Precipitable water
   - Cloud Water path
   - Cloud top temperature
   - Cloud particle size
   - Cloud phase
3) Clear-sky Shortwave Albedo
   - Solar zenith angle
   - Surface albedo Broadband
   - Aerosol Optical Depth
   - Aerosol Type ( Continental, Marine, Urban)
4) Overcast Shortwave Albedo
   - Solar zenith angle
   - Surface albedo broadband
   - Cloud water path
   - Cloud top temperature
   - Cloud particle size
   - Cloud phase

Model calculations are made as either clear or overcast. Partial cloud conditions are handled as a linear combination of clear and cvercast.

CERES fluxes are constrained at the ERB footprint level. Within each ERB footprint, there are many cloud imager pixels. Hence there are often multiple cloud conditions $i$ within a single ERB footprint. The Release 1 footprint-scale SSF product (see ATBD 4.0 and following) can contain clear sky and up to distinct 4 cloud conditions $i$ (clear, low cloud, low-middle, middle, middle-high, and high cloud). In Release 2 a footprint may contain clear sky and no more than 2 of the permitted 4 cloud conditions. For all Releases, this size difference between the cloud imager pixels and the ERB footprint requires that separate radiative transfer calculations be done for the distinct cloud conditions $i$ within the footprint. $C_i$ is the fraction of the footprint covered with cloud condition $i$.

The next step in constrainment is an error equation for each component $k$ of the flux. For example in Release 1, there are two flux components $F_k$ , the broadband SW and LW fluxes at TOA. Sometime after launch, the 8-12μm window channel will be an additional flux component $F_k$; Kratz (1997) has developed the correlated k's for the CERES window channel. Error equations (1) are now defined for each of the flux components $F_k$ as

$$\sum_{i=0}^{n} (F_{ki}\,\Delta C_i + C_i\,dF_{ki} + \Delta C_i\,dF_{ki}) - \Delta F_k = \varepsilon F_k \qquad (1)$$

for the $n$ total cloud conditions, each of cloud fraction $C_i$ , comprising the footprint. For each of the $i$ cloud conditions, there can be an adjustment $\Delta C_i$ to the fractional area (this gives the term $F_{ki}\,\Delta C_i$ ). $dF_{ki}$ is the total adjustment to flux component $k$ for cloud condition $i$ by adjusting model inputs (this gives the term $C_i\,dF_{ki}$ ). Corresponding second order adjustments for the $i$ cloud conditions are given by $\Delta C_i\,dF_{ki}$. The term $\Delta F_k$ is the flux mismatch to be allowed by the constrainment algorithm (this is not the a priori uncertainty, or estimate of error, in the observed flux component $F_k$.) By allowing the mismatch $\Delta F_k$ to be non-zero, we obtain a solution that is not overly constrained by random error. $\varepsilon F_k$ is the initial mismatch between the observed and modeled flux component $F_k$. $\varepsilon F_k$ is simply the difference between the measured flux and the flux calculated with initial, unconstrained radiative transfer parameters.

Equation (1) is simplified by assuming that the second order terms $\Delta C_i\,dF_{ki}$ in cloud fractional area and flux are small compared to their initial values. In the second term ($C_i\,dF_{ki}$ ) of Eq. (1), flux adjustment $dF_{ki}$ is then expressed as the sum of the partial derivatives ($\delta F_{ki}/\delta\nu_j$) w.r.t. selected radiative transfer model input parameters $\nu_j$ and the adjustments $\Delta\nu_j$ to those parameters ($j=1,m$). This yields

$$\sum_{i=0}^{n} (F_{ki}\,\Delta C_i) + \sum_{i=0}^{n} C_i \sum_{j=1}^{m} ((\delta F_{ki}/\delta\nu_j)\Delta\nu_j) - \Delta F_k = \varepsilon F_k \qquad (2)$$

for any flux component $k$ of the footprint over cloud conditions $i$ , expressed in terms of selected radiative transfer model parameters $j$.

The key of the algorithm is the minimization of the sum of the square of the normalized adjustments to the selected model variables and the constraining of the sum of the square of the normalized flux error (Rose et al., 1997). The normalization is taken with the standard deviation ($\sigma$) random error allowance for each of the selected model variables or flux components. $\sigma C_i$ is the expected random error in the fractional cloud cover $C_i$ (i.e., the anticipated random error in the satellite retrieval of the fractional area of high cloud is 5%). $\sigma\nu_j$ is the random error in a selected input parameter for radiative transfer (i.e., 5K for land skin temperature). The random error $\sigma F_k$ in a flux component will be mostly due to the uncertainty in the ADM. The random error minimization constraint is expressed as

$$Z = \sum_{i=0}^{n} (\Delta C_i/\sigma C_i)^2 + \sum_{j=1}^{m} (\Delta\nu_j/\sigma\nu_j)^2 + \sum_{k=1}^{l} (\Delta F_k/\sigma F_k)^2 \qquad (3)$$

where on the r.h.s. the first term represents the cloud fraction adjustments, the second term the radiative transfer model variable adjustments, and the third term the flux component error allowances.

Equation (4) below restricts the solution such that the sum of the cloud fraction adjustments will equal zero. This prevents unrealistic solutions (i.e.., sum of adjusted total fractional area departing from unity).

$$X = \sum_{i=0}^{n} \Delta C_i = 0 \qquad (4)$$

Here multiple forms of equation (2) for any number of flux components (i.e., equations for the two flux components, TOA SW reflected flux and OLR, in Release 1) are combined with equations (3) and (4) using the technique of Lagrange multipliers to form a single equation (5).

$$Y = Z + X\,\lambda_o + \sum_{k=1}^{l} [\textit{Flux error equation (k)}]\,\lambda_k \qquad (5)$$

The next step is setting the derivative of $Y$ w.r.t. each of the $\lambda$'s and normalized adjustments equal to zero and solving the resulting matrix set of simultaneous partial differential equations. The solution can be determined analytically or solved numerically using LU decomposition (Press, 1986).

While seemingly intricate, the algorithm can be summarized with the following highlights:
(a) A small number *k* of observed target fluxes, such as broadband TOA reflected and OLR are used.
(b) Initial estimates of the target fluxes are made with formal radiative transfer calculations for *n* cloud conditions based on input variables.
(c) In the constrainment process, radiative transfer is next expressed in terms of perturbations about the initial formal radiative transfer calculation using pre-computed derivatives of a small number of selected variables *m* (i.e., the derivative of OLR w.r.t. cloud area, cloud top height, and SST).
(d) A priori uncertainties ($\sigma$) are assigned to the observed fluxes, the cloud fractions, and the selected constrainment variables.
(e) The solution minimizes the sum of square of the normalized adjustments and does not produce an exact match to the observed fluxes, cloud fraction, or radiative transfer inputs.
(f) CERES archives the observed TOA fluxes; the initial unconstrained radiative transfer fluxes and input variables used to compute those fluxes; and the constrained fluxes and adjustments to the radiative transfer input parameters

The concept of the trickier parts (i.e., step e) of this process is illustrated in Fig. 11. A hypothetical constrainment is done for SW and LW fluxes over a partly cloudy footprint. The open circle in the upper left shows that the initial, unconstrained radiative transfer calculation is considerably displaced from the TOA SW and LW observations. In the present algorithm, 7 radiative transfer model input variables ($m=7$) are selected for constrainment. Depending upon the scene, the partial derivatives of flux ($\delta F_{ki}/\delta\nu_j$) w.r.t. 7 variables are examined and compared with their corresponding uncertainties $\sigma\nu_j$ . The constrainment process is idealized in Fig. 11 for a hypothetical case of only 3 ($m=3$) variables. In Fig. 11, we close upon an observed flux by adjustments to cloud fraction (diagonal arrow shows effect on SW and LW), surface albedo (vertical arrow shows effect on only the SW), and the surface skin temperature (horizontal arrow shows effect on only the LW). The final constrained SW and LW flux is depicted by the solid circle. Note that the constrained solid circle is still displaced from the observed condition in the center. There is a mismatch of constrained and observed fluxes. This mismatch is small for the mean of many footprints. For an individual footprint, the mismatch can be regarded as a compromise among the weighted uncertainties $\sigma$ of the observed fluxes and input variables. Modeled partial derivatives of flux ($\delta F_{ki}/\delta\nu_j$) are tools in obtaining the weights.

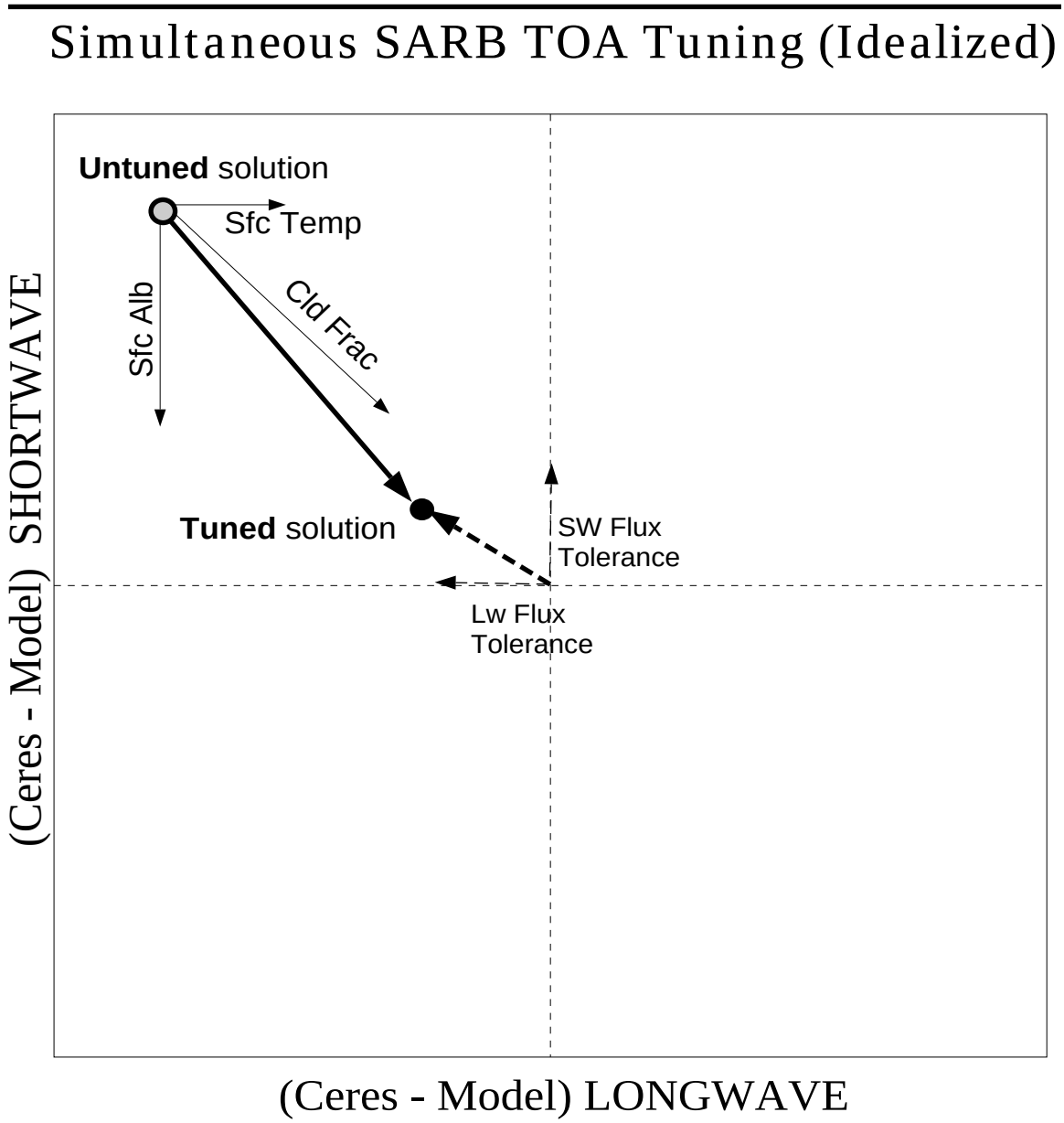


Figure 11 - Idealization of SARB tuning for case with SW TOA, LW TOA, and only 3 adjustable input parameters

The values used for the uncertainty σ parameters in Release 1 are given in Table 6. The initial σ values for TOA fluxes are stated in percent, but they are required to be at least 2 $Wm^{-2}$. The σ values for PW, cloud LWP (or IWP), and aerosol optical depth are specified as fractions because the constrainment algorithm employs logarithmic derivatives of these parameters.

Table 6 Uncertainty σ values for constrainment in Release 1

| | |
|---|---|
| | *TOA parameters* |
| 5.0% | SW TOA |
| 2 $Wm^{-2}$ | minimum value for SW TOA |
| 2.0% | LW TOA |
| 2 $Wm^{-2}$ | minimum value for LW TOA |
| | |
| | *ocean/atmosphere parameters* |
| 1.0 K | skin temperature |
| 0.15 | PW (logarithmic derivative) |
| 0.002 | surface albedo |
| 0.15 | cloud LWP (logarithmic derivative) |
| 2.0 K | cloud top temperature |
| 0.5 | aerosol optical depth (logarithmic derivative) |
| 0.025 | cloud fraction |
| | |
| | *land/atmosphere parameters* |
| 4.0 K | skin temperature |
| 0.10 | PW (logarithmic derivative) |
| 0.015 | surface albedo |
| 0.15 | cloud LWP (logarithmic derivative) |
| 1.0 K | cloud top temperature |
| 0.1 | aerosol optical depth (logarithmic derivative) |
| 0.025 | cloud fraction |

The uncertainty σ in Release 1 for SW TOA flux has been selected as 5%. The σ values for SW TOA and the other parameters are still the subject of experimentation. In Release 4, with the new ADMs, we are confident that σ for SW TOA will be reduced. Recent study of ERBE by Collins and Inamdar (1995) would suggest that the uncertainty σ for LW TOA should be larger than in Table 6, especially for clear skies. In Release 3, window TOA flux (the special CERES 8-12 μm channel) will also be used for constrainment. Uncertainties for the window flux will be specified as smaller in $Wm^{-2}$ than the broadband LW TOA counterpart. Release 2 can constrain to three observed fluxes; as an option, one target can be an observed *surface* flux.

The Release 1 uncertainty σ for skin temperature over land (4 K) was much larger than over the sea (1 K). The large σ for land reflects the uncertainties in both surface emissivity (here fixed) and the directional dependence of canopy emission (Sellers and Hall, 1992). The later is due to the existence of a temperature gradient in a vegetation canopy, with different view angles exposing different temperatures. The land-sea contrast is also apparent in the σ values selected for surface albedo; sea albedo is much better known (i.e., Payne, 1972). ECMWF has experimented with the use of sea state models of waves as an input for the parameterization of sea surface reflectance (Janssen, personal communication); we may try this in Release 2 or 3. In Release 2 the variables (skin temperature, precipitable water, surface albedo, and aerosol optical depth)

will only be adjusted when the footprint is completely clear (<5% cloud). Under non-clear conditions, uncertanties in cloud optical properties and cloud fraction are assumed to predominate.

In Release 1, the $\sigma$ for land and sea cloud LWP are large, and they will remain large for Releases 2, 3, and 4. Cloud top temperature is probably retrieved with more confidence in CERES than is any other cloud parameter. Release 1 uses different cloud top temperature $\sigma$ values for sea (2 K) and land (1 K), but they will be equal in Release 2. The present $\sigma$ value for the logarithm of the aerosol optical depth is larger over the sea (0.5) than over the land (0.1), simply because in clear skies we seek aerosol adjustments over the sea and surface albedo adjustments over land. Aerosol $\sigma$ values for land and sea in Release 2 will be more nearly equal.

### 5.4 Algorithm Applications

Two sections previous (5.3.2 on the Framework of CERES Calculations), we described how the Fu and Liou (1993) code would be set up with CERES data for an initial, unconstrained calculation of the SARB. The following section (5.3.3) described the constrainment algorithm. Two examples are given below. The first example shows unconstrained and constrained results from a pre-launch but formal, CERES-wide, Release 1 production run with large-scale data; a more accurate and extensive full-day simulation (Release 1.5) has been presented informally to the CERES Science Team (but not in this document). The second example is a focused illustration of the capabilities and limitations of radiative transfer and constrainment over the ARM SGP CART site in Oklahoma; this simulation has also been superceeded by more accurate results shown to the ARM Science Team (but not in this document).

#### 5.4.1 Release 1 Results.

While the many figures in this section present only footprint scale CRS results, the reader is advised to review a broader perspective of CERES processing at this point. Please note the "CERES Top Level Data Flow Diagram," a flow chart with bubbles and boxes at the start of this document. This section describes Release 1 results for bubble 5, Clouds and Radiative Swath (CRS), which the figure notes to "Compute Surface and Atmospheric Radiative Fluxes." CRS is an instantaneous set of radiative transfer and constrainment calculations for a single ERB footprint. Much of the sounding data for the CRS calculation is obtained from the nearest hour and CERES gridbox of Meteorology, Ozone, and Aerosol (MOA) data. MOA is a box to the right (and slightly below) CRS. As noted in 5.3.2.1, a single footprint of ERB and cloud property data, labled Single Satellite Footprint (SSF), is an important input for the CRS bubble from above. Note the bubbles FSW and SYN below CRS. FSW is a gridded version of CRS, and FSW is produced to the nearest hour of instantaneous satellite overpass. Further below and to the right of FSW, note SYN. SYN is a gridded 3-hourly synoptic product. SYN is based on the interpolations of FSW, on geostationary satellite imager data, and on another round of SARB radiative transfer calculations.

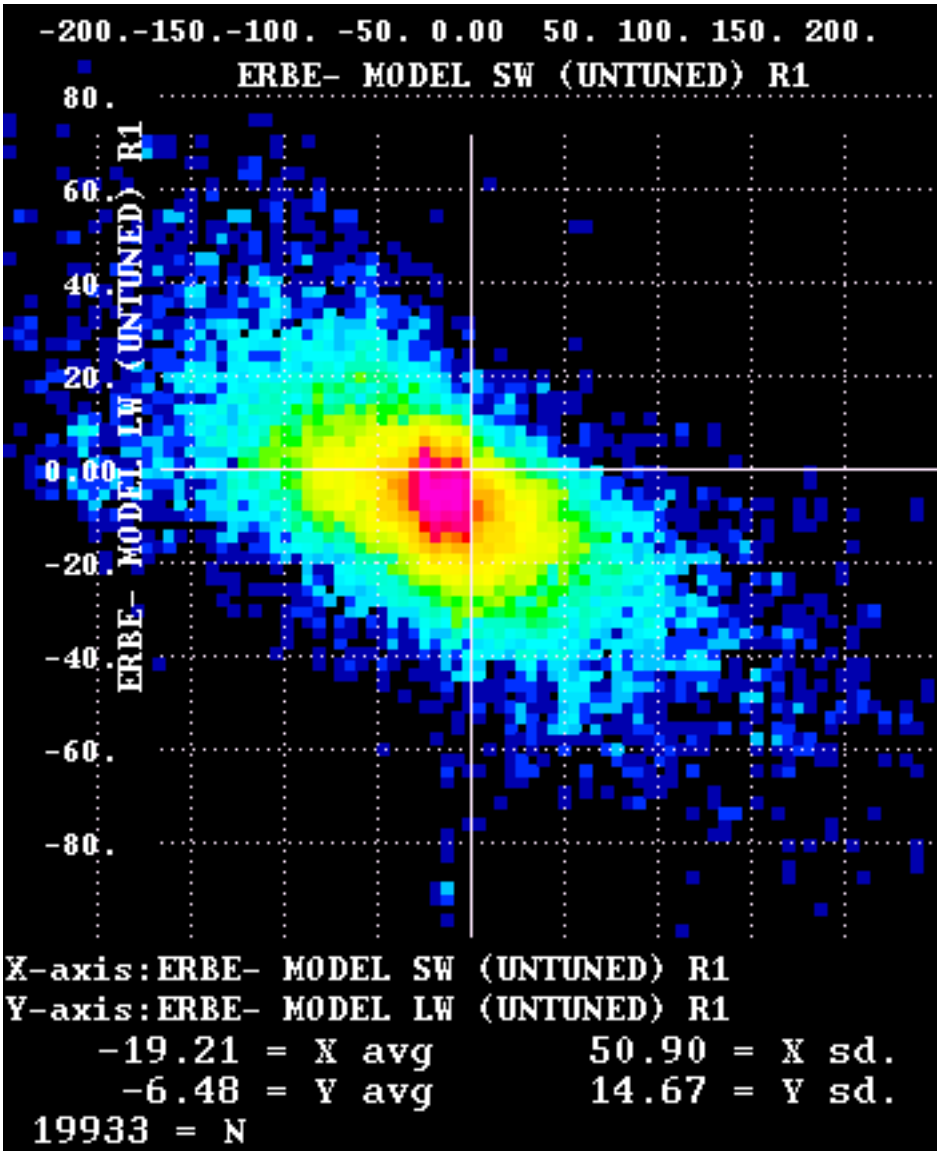


Figure 12 - Total-sky scatterplot of SW (ERBE-Model) vs LW (ERBE-Model) for 19933 untuned footprints

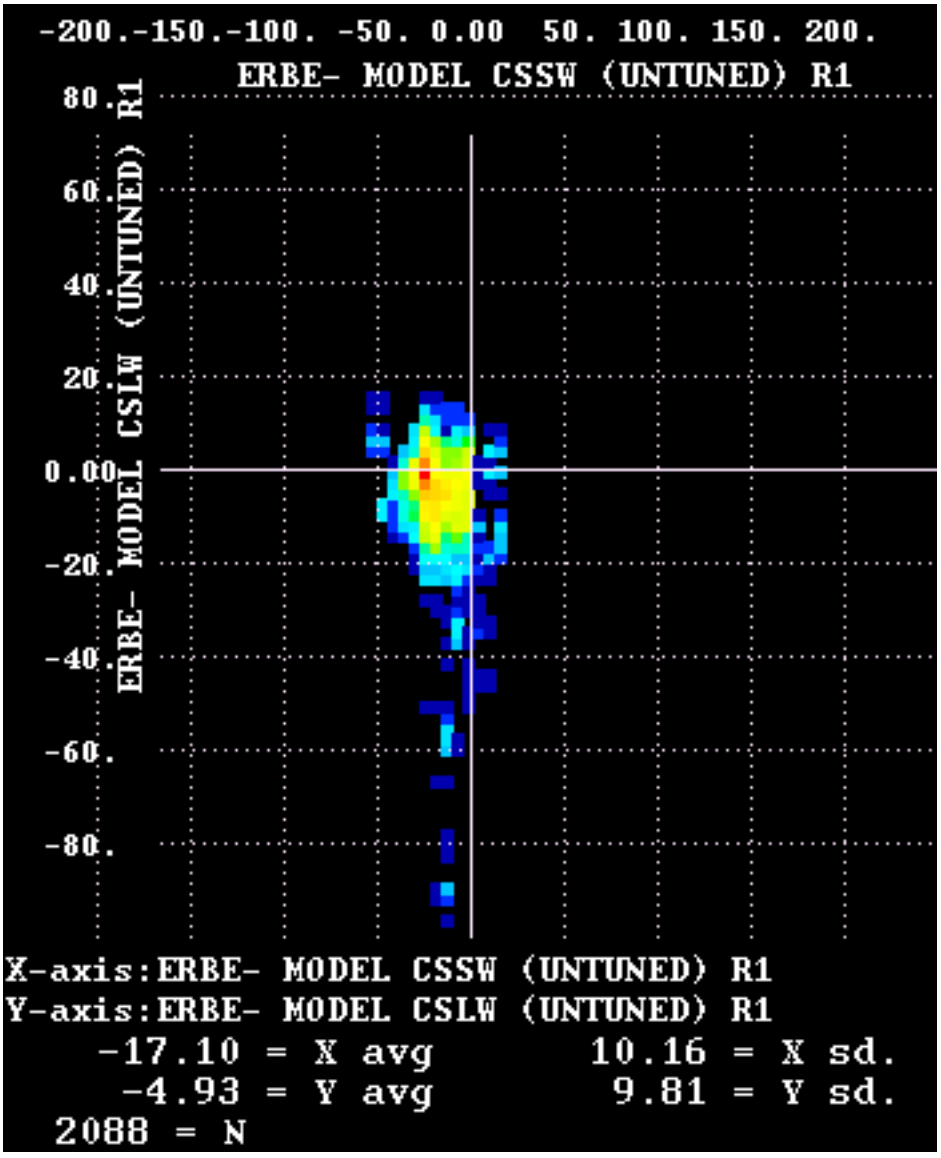


Figure 13 - Clear-sky scatterplot of SW (ERBE-Model) vs LW (ERBE-Model) for 2088 untuned footprints

Preliminary results with a fraction of an orbit of Release 1 CRS calculations are shown as scatterplots in Fig. 12 for total-sky and Fig. 13 for clear-sky footprints. Flux difference plots (ERBE-Model) for SW TOA (Fig. 14) and LW TOA (Fig. 15) indicate the spatial domain of this exercise with October 1, 1986 retrospective data. SW TOA (ERBE-Model) is the difference of *reflected* SW as observed (ERBE) and calculated (Model) with the initial, unconstrained inputs driving the Fu and Liou (1993) code. LW TOA is the OLR. The tabulations at the bottoms of the scatterplots indicate that the unconstrained SW calculation reflects too much SW, both for total sky (in Fig. 12 ERBE-Model is -19.21 $Wm^{-2}$) and clear sky (in Fig. 13 ERBE-Model is -17.10 $Wm^{-2}$). The same tabulations show the calculated OLR exceeds the ERBE observations for total sky (in Fig. 12 ERBE-Model is -6.48 $Wm^{-2}$) and clear sky (in Fig. 13 ERBE-Model is -4.93 $Wm^{-2}$). We suspect that the input PW, here from the NCEP Reanalysis, is too small in this limited swath. A similar effect could be produced by a deficit in the upper tropospheric humidity field (i.e., Soden et al., 1994), which is especially dif-

ficult to account for in operational analyses if LW sounder data is not assimilated. A bias in the input PW for the swath could also account for some of the excess in the model reflected SW for clear-sky conditions (Fig. 13). In the clear-sky scatterplot (Fig. 13), the points at the bottom reveal a small number of huge excesses in the model OLR, possibly due to scene identification error.

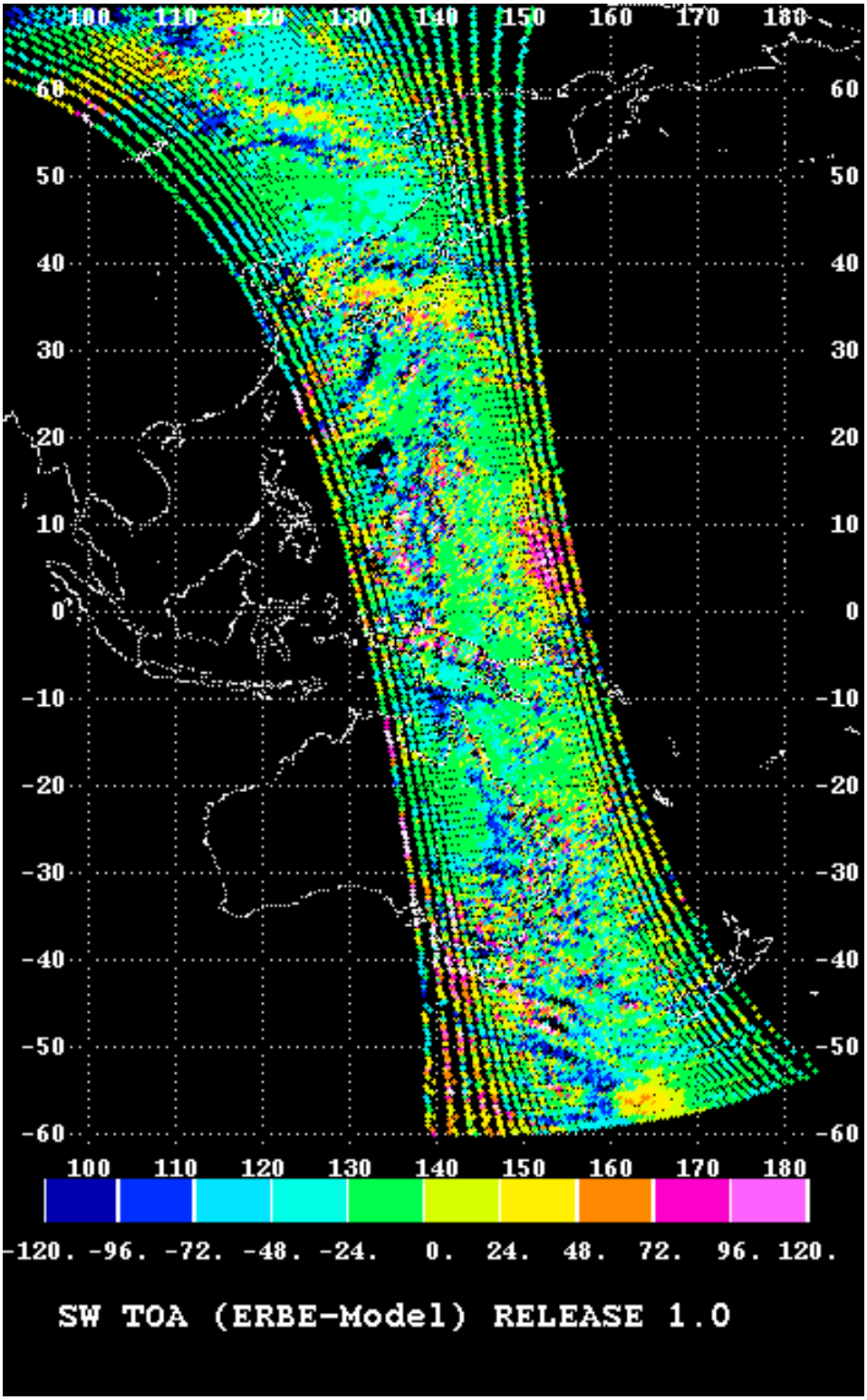


Figure 14 - Difference of total-sky reflected SW as ERBE minus untuned model

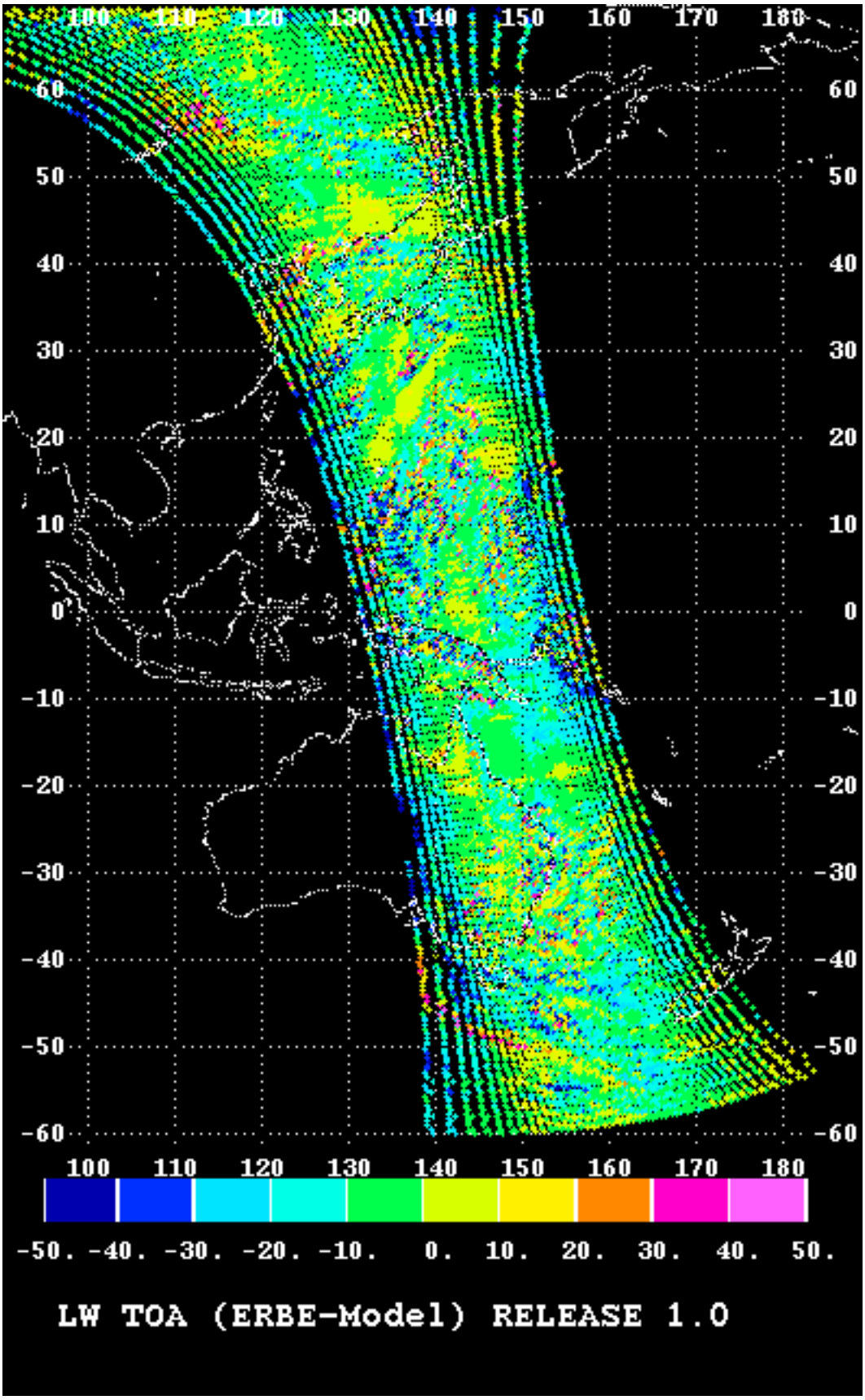


Figure 15 - Difference of total-sky reflected SW as ERBE minus untuned model

In the total sky scatterplot (Fig. 12), the points are grouped downward toward the right. If axes were re-drawn about the center of the cluster, the upper left and lower right quadrants would be the most populated. This suggests that much of the large, apparently random scatter is consistent with a cloud effect. For points in the upper left quadrant, the model OLR is too small, and the model reflected SW is too large; to first order this could be remedied by removing cloud, which would increase the model OLR and decrease the model reflected SW. For points in the lower right quadrant, the model OLR is too large, and the model reflected SW is too small; this could be remedied by adding cloud, which would decrease the model OLR and increase the model reflected SW. Much of the footprint scale difference between ERBE and the model is likely due to random error in the calculation of cloud forcing. The hypothesized random error in cloud forcing may be due to the cloud retrieval, but it could also be due to noise in the angular distribution of radiance (i.e., a result of the ERBE ADM). In the tables at the bottoms of Fig. 12 and Fig. 13, the reported standard deviations of (ERBE-Model) were computed by first subtracting the mean differences. The more recent Release 1.5 results (not shown) indicate a closer match (ERBE-Model), and the grouping of points downward toward the right (as in Fig. 12) has been eliminated.

A few regions in the difference plots of SW TOA (Fig. 14) and LW TOA (Fig. 15) are noteworthy. At approximately $7^{o}$ N, $150^{o}$ E the large positve ERBE-Model SW TOA mismatch (Fig. 14) indicates that the model is not reflecting nearly enough SW. In the same area, the model LW TOA(OLR in Fig. 15) is too large by approximately 20 $Wm^{-2}$. Release 1.0 retrievals of ice particle size are known to contain significant errors in the backscatter direction, which is the case for some of the right-hand side of this orbit swath.

In Australia near $25^{o}$ S, $140^{o}$ E the reflected SW TOA (Fig. 14) and the model LW TOA (Fig. 15) are both too high. This is likely a dual effect of surface albedo and skin temperature for generally clear skies. The first guess surface albedo under clear sky conditions is a retrieval from the Staylor and Wilber (1990) algorithm and ERBE data from SSF at the footprint scale. With the resulting surface albedo, the Fu and Liou (1993) based calculation reflects too much SW. Over this region, the aerosol optical depth assumed by the Staylor and Wilber (1990) algorithm is lower than the optical depth retrieved by Pinker and Laszlo (1992) in the GEWEX SRB Project (Whitlock et al., 1995). We use the GEWEX SRB aerosol, which may account for the excess clear sky reflection in this initial CRS calculation. The constrainment algorithm also significantly reduces the surface skin temperature in this area (Fig. 16). The adjustment to the PW in this same area is small (Fig. 17), because of the relatively high uncertainty $\sigma$ assigned to the skin temperature for constrainment over land (Table 6).

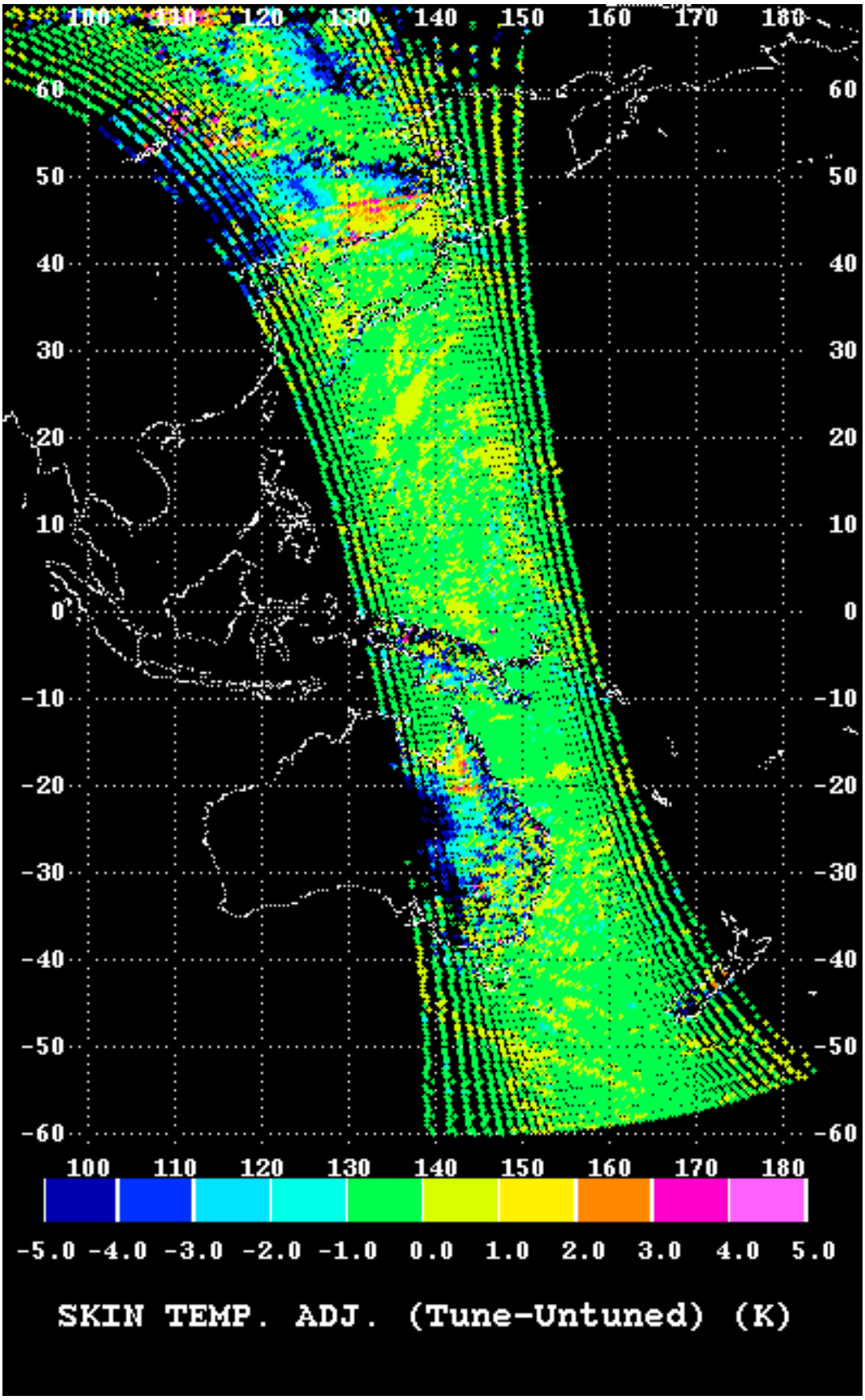


Figure 16 - Tuning of surface skin temperature (total sky)

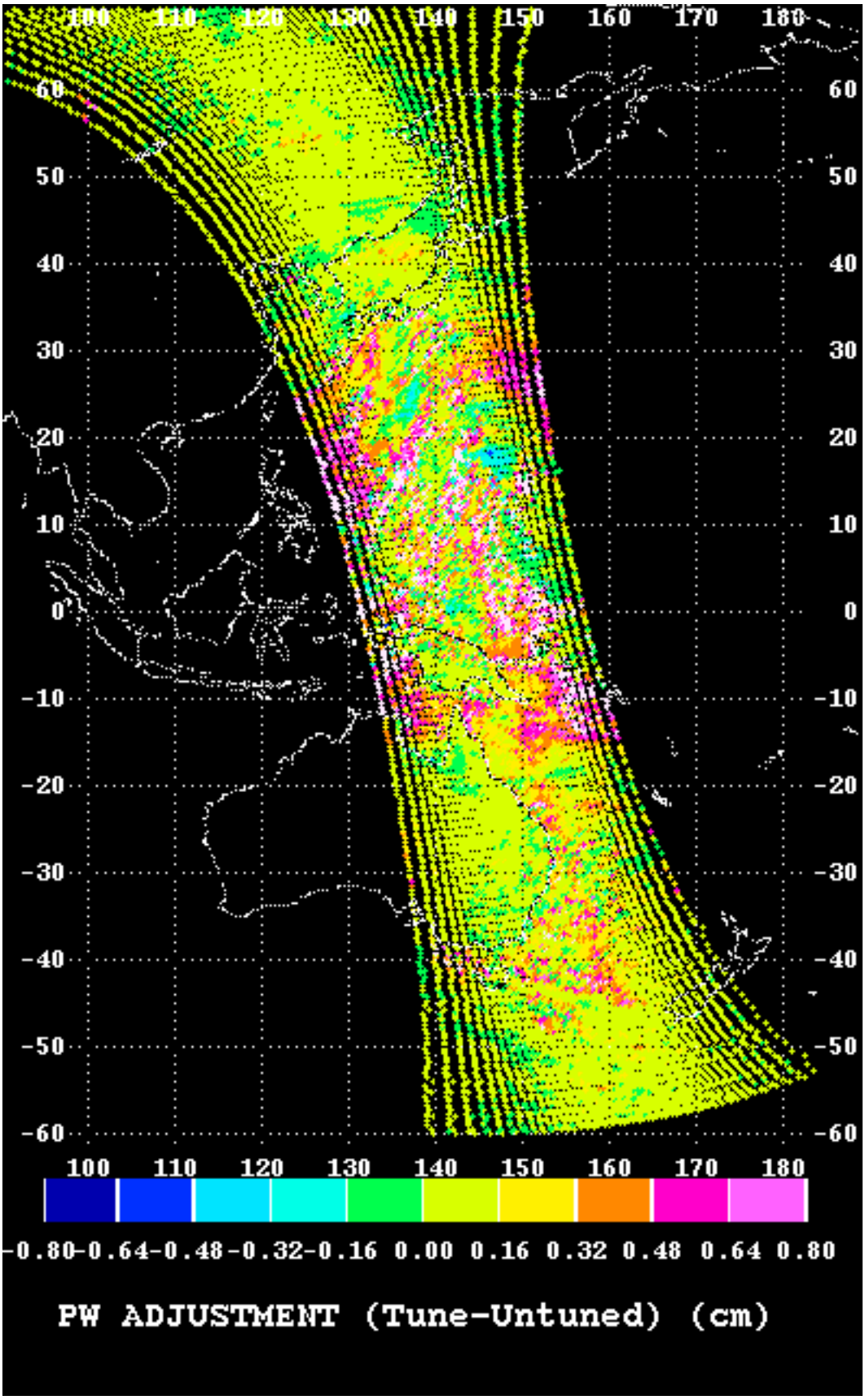


Figure 17 - Tuning of precipitable water (total sky)

Over the oceans, the uncertainty σ assigned to the skin temperature is small (Table 6). We find correspondingly large adjustments to PW in ocean regions near both $10^{o}$ S, $155^{o}$ E and $25^{o}$ N, $150^{o}$ E (Fig. 17). There is significant adjustment to the surface downward LW as well in both ocean regions (Fig. 18). It should be noted that the total-sky constrainment to surface downward LW is driven by adjustments to cloud, rather than to PW, over most of the swath.

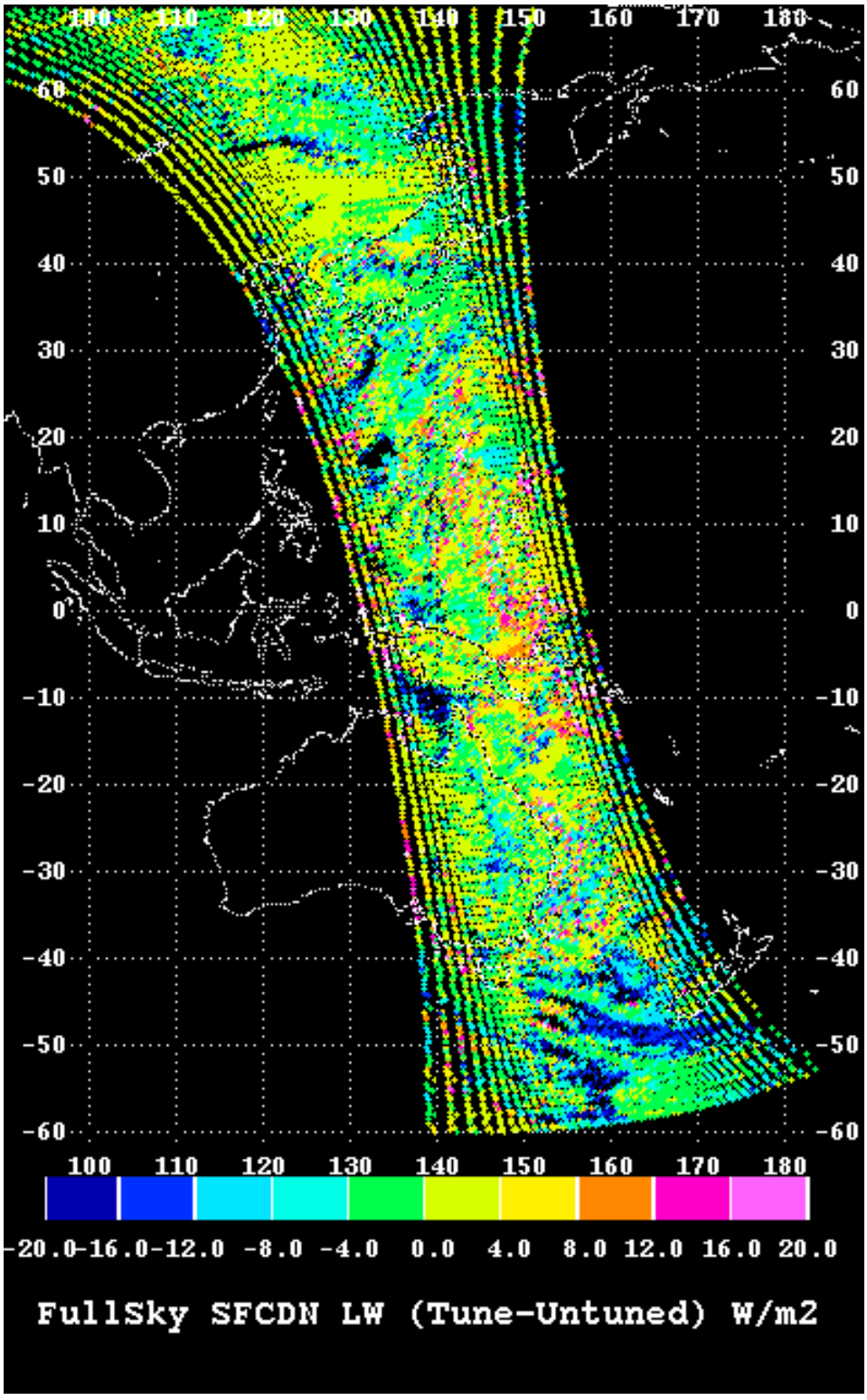


Figure 18 - Tuning of surface downward LW (total sky)

This analysis of Release 1 is incomplete  Also, because of doubts concerning SW fluxes noted earlier, most remarks are confined to the LW here.

Because of the difficulties of determining the geometric thickness of clouds (locating cloud base, as well as cloud top) with passive satellite remote sensing, we anticipate substantial uncertainties in the SARB that CERES determines below cloud tops.  By adding passive microwave to CERES, some advances can be expected.  Cloud LWP can be retrieved with microwave data, and the LWP can in turn be used to estimate the cloud geometric thickness.  CERES plans to buttress VIRS-based cloud retrievals with microwave information from TRMM.  Even without such microwave sensing, there are good prospects for producing a reliable vertical profile of the radiation budget above the cloud tops.  Fig. 19 gives an example of the significant impact of tropospheric clouds on the LW budget at 30-50 hPa in the stratosphere.  Because radiative relaxation times are small in the stratosphere (Ramanathan 1987), the small radiative perturbations that are induced by tropospheric clouds can have a large impact on the equilibrium stratospheric temperature.  The radiation budget near the tropopause has received relatively little attention in global satellite-based retrieval programs to date, but the budget in the upper troposphere and lower stratosphere is an important forcing of the climate.  The radiation budget in the vicinity of the tropopause will be a key CERES product.  Fig. 19 suggests that the detailed cloud property retrievals that CERES provides, in addition to the broadband TOA fluxes, will be essential in determining the space and time variability of the stratospheric radiation budget.

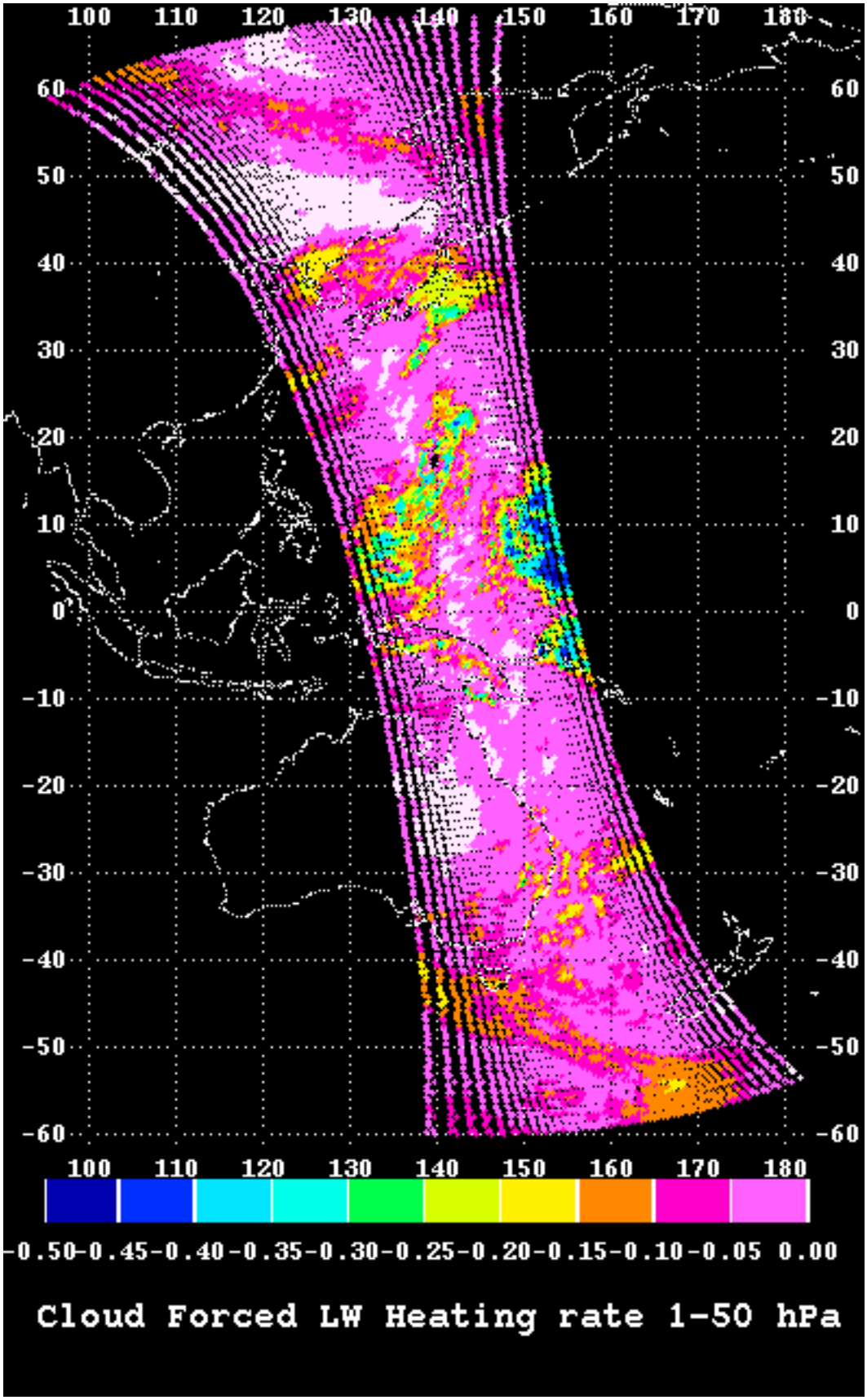


Figure 19 - Forcing of tropospheric cloud to LW heating rate in stratosphere (1-50 hPa)

### 5.4.2 Small-scale Constraiment Exercise.

This section further illustrates present capabilities and limitations of the radiative transfer and constrainment algorithms of Subsystem 5. We focus on the ARM SGP CART site during the April 5-30, 1994 interval of CAGEX Version 1.0. The on-line component of CAGEX Verion 1 (http://snowdog.larc.nasa.gov:8081/cagex.html) is a daylight-only, half-hourly sounding, cloud property, and radiation dataset on a 3x3 grid with validating surface measurements for the central gridbox only. This section will show that the constrainment procedure can readily accomodate different inputs or constraints. The reader is also assured that the constrainment algorithm cannot "fix" fundamental problems in radiation, such as the discrepancy between calculated and measured clear-sky surface insolation noted in 5.3.1.3 and in Table 2.

The mean LW cooling and SW heating profiles for CAGEX Version 1.0 are shown in Fig. 20. The solid lines give the mean LW and SW profiles for the initial, unconstrained fluxes calculated with the Fu and Liou (1993) code and the Minnis et al. (1995) GOES-based cloud retrieval data. Unconstrained fluxes are listed in the second row of the table on Fig. 20. The observed TOA fluxes are from the Minnis et al. (1995) narrowband to broadband conversion with GOES-7. The observed surface fluxes are point measurements at the center of the 3x3 grid. The unconstrained TOA fluxes are close to the observations. There is a huge discrepancy in the total-sky SW surface insolation, 534.3 $Wm^{-2}$ for unconstrained and 457.5 $Wm^{-2}$ for observed.

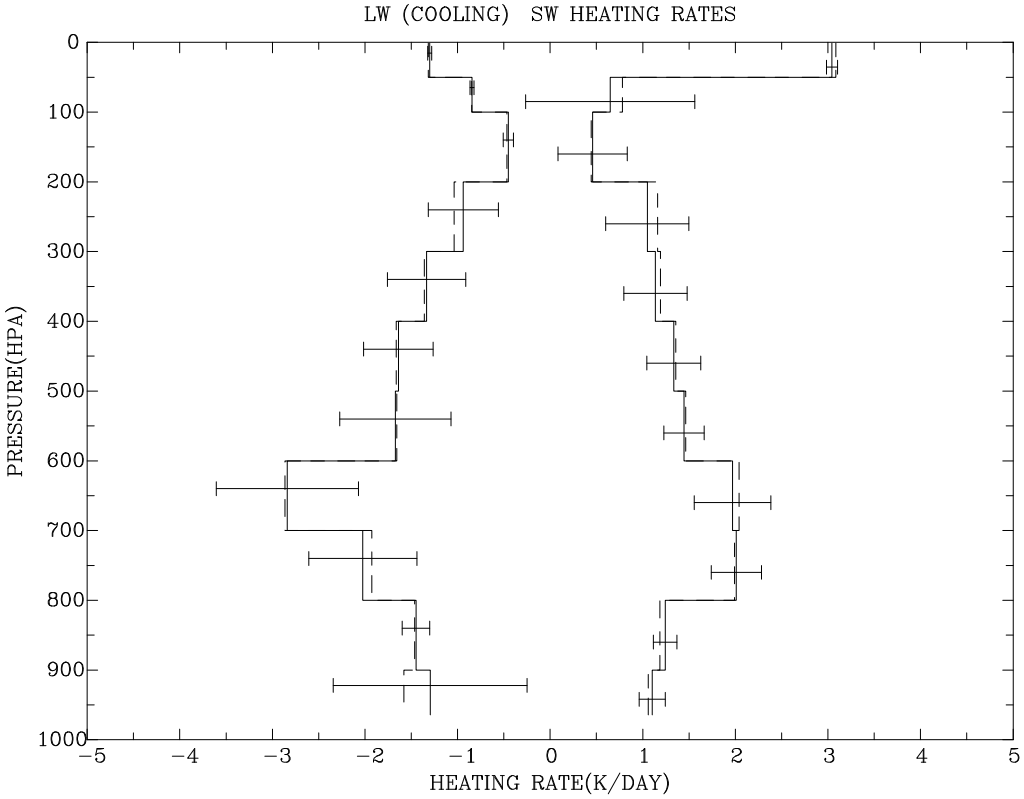


| | AVERAGE | | | | STANDARD DEVIATION | | | |
|---|---|---|---|---|---|---|---|---|
| | TOA SW UP | TOA LW UP | SFC SW DN | SFC LW DN | TOA SW UP | TOA LW UP | SFC SW DN | SFC LW DN |
| OBSERVED | 381.6 | 231.5 | 457.5 | 330.5 | 223.5 | 45.0 | 303.0 | 42.4 |
| UNTUNED | 376.8 | 235.4 | 534.3 | 320.7 | 220.9 | 48.1 | 292.4 | 41.7 |
| TUNED | 397.9 | 233.6 | 503.2 | 322.0 | 242.8 | 47.0 | 319.6 | 41.9 |
| TUNE−UNTUNE | 21.1 | −1.8 | −31.1 | 1.3 | 32.9 | 5.6 | 44.2 | 2.1 |

Figure 20 - Tuning constrained with 3 fluxes (SW TOA, LW TOA, surface SW)

The constrainment algorithm is now applied, constraining to the observed SW TOA and LW TOA as in Release 1, *but also constraining to the measured surface SW insolation.* The discrepancy between the calculated and observed SW surface insolation was the major issue in the earlier Table 2 (for CAGEX Version 1.1, which has new GOES-based retrievals and new MFRSR aerosol data). The table at the bottom of Fig. 20 shows that constrainment has not resolved that issue (for the similar Version 1.0, which has the original GOES-based retrievals and original MFRSR aerosol data). At the surface, constrainment has reduced the discrepancy with the measured SW insolation by 31.1 $Wm^{-2}$, but this has been accomplished by increasing the discrepancy for SW TOA. Each of the three constraining fluxes (SW TOA, LW TOA, and SW at the surface) has an uncertainty $\sigma$, and constrainment does not produce a perfect match to the mean measured value of any of the three.

The dashed profiles in Fig. 20 show the small adjustments to the mean LW cooling and SW heating which are induced by constraining to SW TOA, LW TOA, and SW at the surface. The horizontal bars show the temporal standard deviation of differences between the constrained and unconstrained profiles. The main utility of constrainment, in this case, is apparently a reduction in the noise of the instantaneous LW cooling and SW heating profiles. In CAGEX Version 2, aircraft and additional surface measurements were taken by ARM in the fall 1995 ARESE, and these will help to determine the realism in this hypothesized reduction in noise.

A different constrainment is done for the same profile in Fig. 21, which constrains to LW TOA observations and LW surface measurements (no SW variable as a constraint). The unconstrained results are identical to Fig. 20, which constrained to LW TOA, SW TOA and SW at the surface. With no SW constraint in Fig. 21, the constrainment causes only small changes to the mean and standard deviation fit for SW fluxes. There is very little SW constrainment; the SW discrepancy at the TOA remains small; the SW discrepancy at the surface is essentially unchanged. The further constaint of LW surface measurement hardly improves the constrained LW surface flux (Fig. 21) at all, when compared to the case with no LW surface flux constraint (Fig. 20).

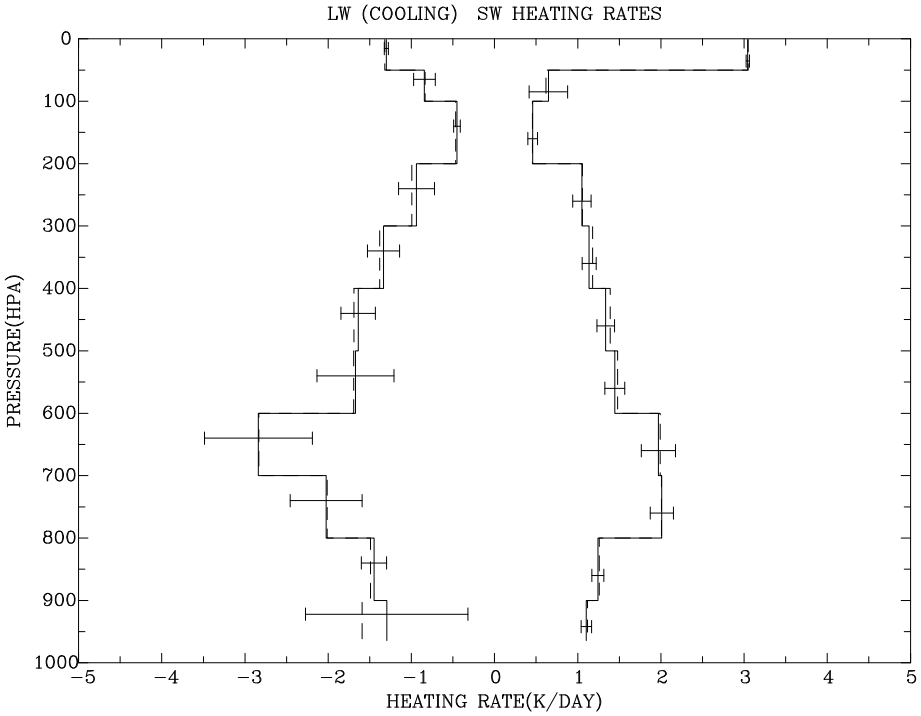


| | AVERAGE | | | | STANDARD DEVIATION | | | |
|---|---|---|---|---|---|---|---|---|
| | TOA SW UP | TOA LW UP | SFC SW DN | SFC LW DN | TOA SW UP | TOA LW UP | SFC SW DN | SFC LW DN |
| OBSERVED | 381.6 | 231.5 | 457.5 | 330.5 | 223.5 | 45.0 | 303.0 | 42.4 |
| UNTUNED | 376.8 | 235.4 | 534.3 | 320.7 | 220.9 | 48.1 | 292.4 | 41.7 |
| TUNED | 375.1 | 234.2 | 533.7 | 323.3 | 219.0 | 45.7 | 288.8 | 41.2 |
| TUNE−UNTUNE | −1.7 | −1.2 | −0.6 | 2.6 | 10.4 | 6.0 | 13.7 | 5.1 |

Figure 21 - Tuning constrained with 2 fluxes (LW TOA and surface LW)

The algorithm is verstile, but the results must be interpreted with care. In a more sophisticated run (not shown), the model was constrained to surface measurements of the separate direct and diffuse beams; the large initial discrepancy of computed and measured diffuse insolation produced a large and probably unrealistic reduction in the aerosol single scattering albedo.

### 5.5 Strategic Concerns

#### 5.5.1 Input data and Radiative transfer

Our calculations of the SARB are performed at the relatively large scale of an ERB footprint using spatially averaged properties of clouds placed in a few idealized atmospheric profiles. The smaller cloud imager pixels have inhomogeneities that generate errors when one attempts (as in Subsystem 4) to retrieve cloud physical and optical properties from pixel-scale data (Wielicki and Parker 1992). It is anticipated that successive generations of CERES cloud retrievals will improve through intercomparison with data from field campaigns such as the First ISCCP Regional Experiment (FIRE). Because of the large impact of ice crystal characteristics on cloud optical properties (Liou 1992), improved retrievals of cloud ice are eagerly awaited. Takano and Liou (1994) have developed a new Monte Carlo/geometric ray-tracing method for calculating the scattering from ice crystals; this approach can be expected to advance both the remote sensing of ice clouds (i.e., Minnis et al. 1993a, b) and the effect of ice clouds on broadband fluxes (Fu and Liou 1993).

There are considerable uncertainties relating to the properties of the surface, aerosols, and meteorological data. As noted earlier, aerosol absorption is one possible source of the (possibly) anomalous absorption by clouds (Stephens and Tsay 1990). We constrain for aerosol optical depth over the sea and land. Virtually any optical property that we infer about the surface is tied to the limitations of the input aerosol data. We await MODIS aerosol retrievals for aerosol optical depths over land. CERES will provide an independent aerosol retrieval with VIRS on TRMM. The Direct Aerosol Radiative Forcing initiative (Ogren, 1995, personal reference; this is an update of IGAC, 1994) and earlier reviews (i.e., Penner, 1994) indicate that the satisfactory measurement of aerosol radiative properties will indeed be a challenge, especially as regards absorption.

Over land, the input surface albedo for clear skies from the ERB and the Staylor and Wilber (1990) algorithm is straightforward, but essentially unvalidated. For cloudy skies, we use the Staylor ERBE-based GEWEX SRB Project surface albedo, which is uniform through the month. Lacking a time history of retrieved albedos for cloudy skies, we have assumed an albedo, and constrained the resulting error into the cloud properties. Some of the problems relating to the SW optical properties of the surface could be resolved with a time history study, wherein a surface albedo record would be developed and successively honed with repeated passes. When we attempt to interpret the partitioning of the SW surface fluxes into upwelling and downwelling components, we are affected by our lack of information on the surface bidirectional reflectance function (BDRF). CERES has also planned a series of helicopter flights over the ARM site in Oklahoma, which will use a scanning SW spectrometer and one LW channel, to determine the BDRF and directional dependence of the emission.

*Our main current problem is the discrepancy of calculated and measured mean SW flux (Table 2).* CAGEX, a community activity, is our track for solving this problem. We will continue to make our resources available to other groups and collaborate with ARM (sponsored by the Biological and Environmental Sciences Program of the Department of Energy) and GEWEX. The intermediate-term focus is on clear sky SW in ARESE, wherein we approach the surface albedo (Rutan and Charlock, 1997; Schuster et al., 1997) and aerosol absorption (Table 7) issues in the above two paragraphs.

Table 7 - Mean biases (calculated minus measured in Wm-2) for SW in ARESE for different aerosol inputs

| V2.0 SW Biases (W/m**2) | FULL-SKY AEROSOL SENSITIVITY | | | | | | | | | | |
|---|---|---|---|---|---|---|---|---|---|---|---|
| | A | B | C | D | E | F | G | H | I | J | K |
| TOA Insolation (W/m**2) | 717 | 717 | 717 | 717 | 717 | 717 | 717 | 717 | 717 | 717 | 717 |
| TOA Net | -20 | -16 | -25 | -18 | -19 | -20 | -22 | -21 | -18 | -14 | -10 |
| TOA Reflected SW | 20 | 16 | 24 | 18 | 19 | 20 | 22 | 21 | 18 | 14 | 10 |
| TOA Albedo | .027 | .021 | .032 | .024 | .025 | .026 | .029 | .027 | .023 | .018 | .013 |
| Atmospheric Absorption | -58 | -62 | -54 | -52 | -61 | -56 | -60 | -57 | -51 | -44 | -36 |
| Atmospheric Transmittance | .063 | .078 | .049 | .058 | .070 | .062 | .065 | .060 | .056 | .052 | .045 |
| SFC Insolation | 45 | 56 | 35 | 42 | 50 | 44 | 46 | 43 | 40 | 37 | 32 |
| SFC Direct Down | -8 | 26 | -38 | -8 | -17 | -8 | -14 | -20 | -21 | -21 | -20 |
| SFC Diffuse Down | 53 | 29 | 73 | 50 | 68 | 52 | 61 | 63 | 62 | 58 | 53 |
| SFC Net | 35 | 44 | 27 | 32 | 39 | 34 | 36 | 34 | 31 | 29 | 25 |
| SFC Reflected SW | 10 | 12 | 9 | 10 | 11 | 10 | 11 | 10 | 9 | 9 | 8 |
| SFC Albedo | .003 | .003 | .003 | .003 | .003 | .003 | .003 | .003 | .003 | .003 | .003 |

| V2.0 SW Biases (W/m**2) | CLEAR-SKY AEROSOL SENSITIVITY | | | | | | | | | | |
|---|---|---|---|---|---|---|---|---|---|---|---|
| | A | B | C | D | E | F | G | H | I | J | K |
| TOA Insolation (W/m**2) | 702 | 702 | 702 | 702 | 702 | 702 | 702 | 702 | 702 | 702 | 702 |
| TOA Net | -22 | -16 | -27 | -19 | -20 | -22 | -24 | -23 | -19 | -15 | -10 |
| TOA Reflected SW | 22 | 16 | 27 | 19 | 20 | 21 | 24 | 23 | 19 | 15 | 10 |
| TOA Albedo | .029 | .022 | .037 | .026 | .027 | .029 | .032 | .031 | .026 | .020 | .013 |
| Atmospheric Absorption | -50 | -54 | -46 | -44 | -53 | -49 | -53 | -49 | -44 | -36 | -27 |
| Atmospheric Transmittance | .056 | .074 | .039 | .051 | .065 | .055 | .059 | .053 | .049 | .044 | .037 |
| SFC Insolation | 39 | 52 | 27 | 36 | 45 | 39 | 41 | 37 | 34 | 31 | 26 |
| SFC Direct Down | 10 | 58 | -31 | 10 | -3 | 11 | 1 | -7 | -9 | -8 | -8 |
| SFC Diffuse Down | 30 | -6 | 59 | 26 | 49 | 28 | 40 | 45 | 44 | 39 | 34 |
| SFC Net | 26 | 36 | 16 | 23 | 31 | 25 | 27 | 25 | 22 | 20 | 16 |
| SFC Reflected SW | 13 | 16 | 11 | 12 | 14 | 13 | 14 | 13 | 12 | 11 | 10 |
| SFC Albedo | .010 | .009 | .010 | .010 | .009 | .010 | .010 | .010 | .009 | .009 | .009 |

- **Column A** – Calculations use core input data.
- **Column B** – Core input, no aerosols.
- **Column C** – Core input, with aerosol optical depth doubled.
- **Column D** – Core input, with aerosol absorption doubled.
- **Column E** – Core input, except d'Almeida et al. ocean model used.
- **Column F** – Core input, except d'Almeida et al. urban model used.
- **Column G** – Core input, except Tegen and Lacis 0.5 micron mineral dust model used.
- **Column H** – Core input, except Tegen and Lacis 1 micron mineral dust model used.
- **Column I** – Core input, except Tegen and Lacis 2 micron mineral dust model used.
- **Column J** – Core input, except Tegen and Lacis 4 micron mineral dust model used.
- **Column K** – Core input, except Tegen and Lacis 8 micron mineral dust model used.

The latest CAGEX results for ARESE (September 25 - November 1, 1995) at the ARM CART site in Oklahoma are shown in Tables 7, 8, and 9 and Figure 22 (Alberta and Charlock, 1997). The results shown here are preliminary. An "official" set of results for CAGEX Version 2 will be re-run using the new, modified Fu et al. (1997) code with the CKD continuum. Each bias in Tables 7, 8, and 9 is the mean difference of computed (Fu and Liou, 1993 code) and measured fluxes at the top-of-the-atmosphere (TOA) or surface (SFC) using the ensemble of half-hourly time blocks spanning September 25 - November 1, 1995. In Column A for the d'Almeida et al. (1991) continental aerosols with the "core" sounding (interpolated ARM radiosondes and MFRSR-measured aerosol optical depth), we note substantial

biases for the surface diffuse insolation of 53 $Wm^{-2}$ for total-sky (which includes clouds) and 30 $Wm^{-2}$ for clear-sky. In the successive columns, the bias is recomputed for cases with no aerosols, doubled aerosol optical depth, doubled aerosol absorption, and with different optical models for aerosols; d'Almeida et al. (1991) maritime and urban aerosols; Tegen and Lacis (1996) mineral aerosols of different sizes. The bias in the downward diffuse flux is quite resistant to reasonable changes in aerosol optical properties.

Table 8 shows that the humidity sounding is not a likely source of this large bias in diffuse insolation; different sources for humidity, such as the NCEP mesoscale Eta model output, the AERI interferometer, or the microwave radiometer also yield the large bias.

Table 8 - Mean biases (calculated minus measured in $Wm^{-2}$) for SW in ARESE using different sources for the atmospehric humidity sounding

| V2.0 SW Biases (W/m**2) | FULL-SKY HUMIDITY SENSITIVITY | | | | | | |
|---|---|---|---|---|---|---|---|
| | A | B | C | D | E | F | G |
| TOA Insolation (W/m**2) | 717 | 717 | 717 | 681 | 693 | 694 | 717 |
| TOA Net | -20 | -13 | -27 | -23 | -23 | -24 | -19 |
| TOA Reflected SW | 20 | 13 | 27 | 23 | 23 | 24 | 19 |
| TOA Albedo | .027 | .017 | .035 | .032 | .031 | .032 | .025 |
| Atmospheric Absorption | -58 | -41 | -74 | -56 | -51 | -52 | -55 |
| Atmospheric Transmittance | .063 | .045 | .081 | .059 | .053 | .055 | .060 |
| SFC Insolation | 45 | 32 | 58 | 40 | 37 | 38 | 43 |
| SFC Direct Down | -8 | -20 | 2 | -14 | -6 | -5 | -10 |
| SFC Diffuse Down | 53 | 52 | 57 | 54 | 42 | 43 | 53 |
| SFC Net | 35 | 26 | 44 | 31 | 26 | 27 | 34 |
| SFC Reflected SW | 10 | 6 | 14 | 9 | 11 | 11 | 10 |
| SFC Albedo | .003 | .000 | .006 | .002 | .006 | .007 | .003 |

| V2.0 SW Biases (W/m**2) | CLEAR-SKY HUMIDITY SENSITIVITY | | | | | | |
|---|---|---|---|---|---|---|---|
| | A | B | C | D | E | F | G |
| TOA Insolation (W/m**2) | 702 | 702 | 702 | 640 | 690 | 690 | 702 |
| TOA Net | -22 | -15 | -27 | -26 | -24 | -24 | -21 |
| TOA Reflected SW | 22 | 15 | 27 | 26 | 24 | 24 | 21 |
| TOA Albedo | .029 | .021 | .037 | .038 | .032 | .033 | .028 |
| Atmospheric Absorption | -50 | -33 | -67 | -52 | -49 | -51 | -47 |
| Atmospheric Transmittance | .056 | .035 | .078 | .058 | .056 | .058 | .053 |
| SFC Insolation | 39 | 24 | 55 | 38 | 39 | 40 | 37 |
| SFC Direct Down | 10 | -6 | 24 | 11 | 9 | 11 | 7 |
| SFC Diffuse Down | 30 | 31 | 31 | 27 | 29 | 29 | 30 |
| SFC Net | 26 | 16 | 36 | 24 | 25 | 26 | 24 |
| SFC Reflected SW | 13 | 8 | 18 | 13 | 13 | 14 | 13 |
| SFC Albedo | .010 | .007 | .013 | .010 | .010 | .010 | .009 |

- **Column A** – Calculations use core input data.
- **Column B** – Core input, with doubled humidity.
- **Column C** – Humidity is half that of the core input.
- **Column D** – Eta sounding dataset used.
- **Column E** – Core input, using AERI humidity below 2 kilometers.
- **Column F** – Core input, using AERI humidity below 2 kilometers. The humidity profile is scaled by the ARM microwave radiometer retrieval of precipitable water..
- **Column G** – Core sounding data, with humidity added to the soundings as follows:
  - 10% was added to the humidity from the surface to 700 mb.
  - 20% was added to the humidity from 700 mb to 500 mb.
  - 30% was added to the humidity from 500 mb to 250 mb.

Radiometric measurements are another point of contention. Table 9 shows the biases (calculated minus measured in $Wm^{-2}$) using different sources for the measured fluxes. WMO recommends that standard instrumentation (i.e., Eppleys) be combined to measure the SW direct and diffuse beams separately; this is compared for the ARM SIROS (see the row with SFC Insolation in Table 9, Column A) with the unshaded flat-plate pyranometer (Column B). Note that the RAMS (Valero et al., 1996) radiometer (Column E) has the smallest bias w.r.t. calculations for clear sky; RAMS uses new technology and is not operated using WMO protocols. Columns F through J use unshaded Eppley pyranometers deployed by Whitlock and Schuster. Fortunately, ARM has recently deployed a radiometric calibration facility to address the measurement issue for SW. The SIROS and "BSRN" NIP records used in Tables 7, 8, and 9 were adjusted as per cavity radiometer checks in April 1996 (Michalsky et al, 1997).

Table 9 - Mean biases (calculated minus measured in $Wm^{-2}$) for SW in ARESE using different sources for the radiometric measurements

| V2.0 SW | FULL-SKY RADIOMETER COMPARISONS | | | | | | | | | |
|---|---|---|---|---|---|---|---|---|---|---|
| Biases (W/m**2) | A | B | C | D | E | F | G | H | I | J |
| TOA Insolation (W/m**2) | 717 | 717 | 717 | 717 | 717 | 717 | 717 | 717 | 717 | 717 |
| TOA Net | -20 | -20 | -20 | -20 | -20 | -20 | -20 | -20 | -20 | -20 |
| TOA Reflected SW | 20 | 20 | 20 | 20 | 20 | 20 | 20 | 20 | 20 | 20 |
| TOA Albedo | .027 | .027 | .027 | .027 | .027 | .027 | .027 | .027 | .027 | .027 |
| Atmospheric Absorption | -58 | -72 | | | | -81 | -39 | -76 | -82 | -70 |
| Atmospheric Transmittance | .063 | .081 | .054 | .069 | .057 | .067 | .072 | .077 | .085 | .075 |
| SFC Insolation | 45 | 58 | 39 | 50 | 44 | 48 | 51 | 55 | 61 | 54 |
| SFC Direct Down | -8 | | -2 | | | | | | | |
| SFC Diffuse Down | 53 | | 40 | | | | | | | |
| SFC Net | 35 | 48 | | | | 56 | 17 | 51 | 57 | 46 |
| SFC Reflected SW | 10 | 10 | | | | -9 | 35 | 3 | 4 | 8 |
| SFC Albedo | .003 | -.004 | | | | -.045 | .059 | -.019 | -.022 | -.007 |

| V2.0 SW | CLEAR-SKY RADIOMETER COMPARISONS | | | | | | | | | |
|---|---|---|---|---|---|---|---|---|---|---|
| Biases (W/m**2) | A | B | C | D | E | F | G | H | I | J |
| TOA Insolation (W/m**2) | 702 | 702 | 702 | 702 | 702 | 702 | 702 | 702 | 702 | 702 |
| TOA Net | -22 | -22 | -22 | -22 | -22 | -22 | -22 | -22 | -22 | -22 |
| TOA Reflected SW | 22 | 22 | 22 | 22 | 22 | 22 | 22 | 22 | 22 | 22 |
| TOA Albedo | .029 | .029 | .029 | .029 | .029 | .029 | .029 | .029 | .029 | .029 |
| Atmospheric Absorption | -50 | -71 | | | | -84 | -28 | -75 | -87 | -68 |
| Atmospheric Transmittance | .056 | .084 | .045 | .058 | .034 | .068 | .068 | .075 | .086 | .074 |
| SFC Insolation | 39 | 59 | 32 | 41 | 26 | 48 | 48 | 52 | 60 | 52 |
| SFC Direct Down | 10 | | 11 | | | | | | | |
| SFC Diffuse Down | 30 | | 22 | | | | | | | |
| SFC Net | 26 | 46 | | | | 58 | 5 | 49 | 61 | 43 |
| SFC Reflected SW | 13 | 13 | | | | -10 | 43 | 4 | -1 | 9 |
| SFC Albedo | .010 | .001 | | | | -.042 | .067 | -.016 | -.029 | -.005 |

- **Column A** – SIROS, using pyrheliometer + shaded pyranometer combination for surface insolation.
- **Column B** – SIROS, using pyranometer for surface insolation.
- **Column C** – BSRN, using pyrheliometer + shaded pyranometer combination for surface insolation.
- **Column D** – BSRN, using pyranometer for surface insolation.
- **Column E** – RAMS surface radiometry.
- **Column F** – LSRN, site DWA
- **Column G** – LSRN, site FRA.
- **Column H** – LSRN, site KYL.
- **Column I** – LSRN, site TOM.
- **Column J** – LSRN, average of the four sites.

ARESE confirms that there are enormous discrepancies between computed and measured SW insolation for some cloudy sky cases. Figure 22 compares the reflected SW at TOA computed (code from Fu and Liou, 1993) and measured (GOES-8 narrowband to broadband conversion from Minnis et al., 1995) and the surface insolation as computed (code from Fu and Liou, 1993) and measured (see Table 9) for October 31, 1995 The cloud optical depths were taken from GOES-8 narrowband retrievals of Minnis et al. (1995). This cloudy day appears to confirm the large "anomalous SW absorption by cloud" described earlier by Cess et al. (1995), Ramanathan et al. (1995), and Pilewskie and Valero (1995). When integrated over the whole ARESE period, however, the biases in surface insolation for total-sky (full-sky) and clear-sky are comparable (SFC Insolation row in above Tables 7, 8, and 9), suggesting significant problems with SW radiation in both cloudy and clear conditions.

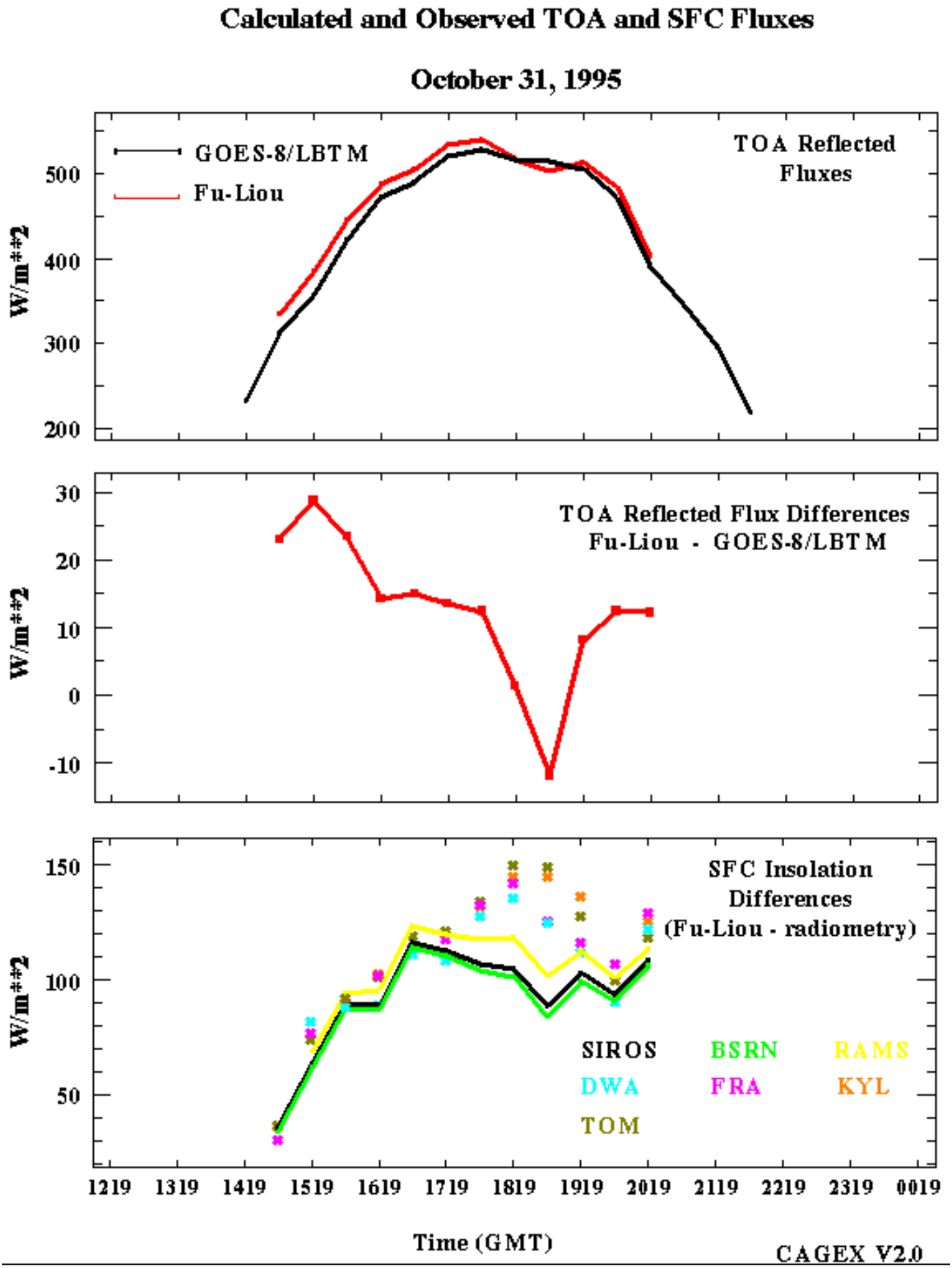


Figure 22 - Calculated (Fu-Liou code) and observed SW fluxes at TOA and surface for October 31, 1995 at the ARM CART site in Oklahoma

Further work will interpret these measurements with new aerosol profiling data from lidar (Hlavka et al., 1997) over the ARM site, the ARM SIROS radiometer network, and the ARESE Scripps Atmospheric Research Laboratory RAMS (Valero et al., 1996) broadband radiometer from ARESE Twin Otter, Egret, and ER-2 flights. This will be a combined approach to clear-sky aerosol and surface SW effects. Clear-sky SW constrainment exercises will be used.

There are different problems with the surface LW. Sellers and Hall (1992) noted the strong directional dependence of LW emission from the surface itself, which suggests that a constrainment at one satellite angle may not be representative of the hemispherically integrated flux. As noted earlier, the effect is produced by a vegetation canopy, which commonly has a vertical temperature gradient; by observing at different viewing angles, one sees different parts of the canopy, which have different temperatures. While our surface emissivities are non-black, they are uncertain, which again will generate an error in the surface flux (Wan and Dozier 1989; Prata, 1993). MODIS will retrieve the surface emissivity, but some care will be needed in such a retrieval because of the aforementioned directional dependence. In analyzing the LW flux and directional radiance data from the forthcoming CERES helicopter measurements over ARM, we will experiment with the retrieval of surface temperature and emissivity. The NCEP and DAO data for atmospheric temperature is generally regarded as accurate to within 1 or 2 deg K. Under most circumstances, other parameters will induce larger errors. Uncertainties in water vapor are known to have a great impact on fluxes; GEWEX (Chahine 1992) has been organized, partly because of these uncertainties. Our constrainment of PW to match TOA broadband fluxes is a small step forward. Microwave water vapor data for the actual CERES mission and constrainment to narrowband (in addition to broadband) would yield further advances. The development of correlated-k's for use in the AVHRR channels (Kratz, 1997) with the Fu and Liou (1993) code will permit the testing of this concept before launch. CAGEX will investigate sounding input issues for LW intensively over the ARM site in Oklahoma. The ARM program includes special radiosonde launches, a nearby network of National Weather Service (NWS) remote profilers, and on-site microwave and Raman lidar retrievals of water vapor. Through GCIP, NWS mesoscale Eta model outputs with hundreds of parameters at nested points around the ARM site are archived hourly (July - August 1994 and indefinitely after April 1995); these include analyses from the Eta Data and Assimilation System (EDAS), as used in Table 8 above for SW.

We will compare our Release 1.5 results with more temporally extensive efforts like ISCCP and the GEWEX SRB Project. The CERES retrievals of clouds and fluxes are quite different than in ISCCP and the SRB Project, and it will be scientifically interesting to analyze the cloud to flux correlations in these other global retrievals.

### 5.5.2. Inhomogeneities and 3-D Effects

Release 1 SARB calculations do not account for the differences in cloud optical depth between the groups of cloud imager pixels. We simply average them over the ERBE footprint to the mean properties of High, Upper Middle, Lower Middle, and Low clouds, thereby introducing a systematic error. We further assume that the world is plane parallel, both with regard to the CERES cloud retrievals used as inputs and the broadband radiative transfer codes used to calculate the SARB itself. Three-dimensional calculations by Schmetz (1984) suggest that under some circumstances, 3-D effects may be accounted for in the SW with minor adjustments to plane-parallel calculations. Heidinger and Cox (1994) have reported some success in accounting for finite (3-D) cloud effects on surface DLF. O'Hirok and Gautier (1996) have computed comprehensive 3-D radiative profiles for a few cases.

We regard cloud inhomogeneity and finite geometry as the most formidable barriers to our effort to retrieve the *instantaneous* radiative flux divergence in the troposphere. Cloud geometry is a strong forcing on the short term variability of flux. Some advance is expected through CERES participation in the ARM program. Our initial goals have been met: a determination of the error in satellite-based, plane-parallel SARB calculations in various space-time domains (i.e., Tables 2, 7, 8, and 9 and Figs. 20 and 22). To further approach the multi-dimensional cloud problem, we have the preliminary resource of approximately 70 hours of joint flight time with RAMS SW broadband measurements on Twin Otter, Egret, and ER-2 in ARESE. Hayasaka

et al. (1995) have shown that care is needed in the interpretation of such measurements. Another resource in determining how simple, plane parallel results can be best interpreted will be the scores of broadband Licor measurements in the Oklahoma mesonet around ARM.

The widely dispersed, SW and LW BSRN radiometers will generate another database for CERES validation at about 30 locations worldwide. The "finite" cloud effect of uncertainty in satellite-observed cloud geometric thickness has an enormous impact on assessments of the LW SARB especially. A satellite-borne CPR would be needed to provide a reliable global survey of cloud geometric thickness for optically thick clouds. For optically thin clouds, a space-borne lidar is needed. The present Automated Surface Observing Sites (ASOS) which have been deployed with laser beam ceilometers (LBC) at hundreds of locations in the US, providing hourly cloud bases below 4 km, will yield a more accurate climatology of cloud base heights. When combined with satellite data in the GEWEX Continental-Phase International Project (GCIP; World Climate Research Program 1992) and enhanced surface radiometric observations, a sound test of satellite-based retrievals of the SARB and cloud base heights would be possible.

### 5.6 Data Processing Requirements

Since Release 1, Dr. Qiang Fu provided a 2-stream model (Fu et al., 1997) that greatly reduced the CPU time needed to process a CERES FOV. New CPU chips (R10000), along with new versions of the operating systems and compilers, have greatly reduced the CPU time needed.

A timing study conducted in April 1997 tracked the number of daytime and nighttime Fu-Liou calculations made during a contiguous 15-hour period. The number of CERES FOVs with no cloud layers, one cloud layer, and two cloud layers were tracked. Results indicate 64 Fu-Liou calculations with 30 vertical levels can be made per second. Assuming the minimum cloud layer coverage scenario of no cloud layers -- initial and constrained clear sky Fu-Liou calculations only (two calculations) -- 32 CERES FOVs can be processed per second. Assuming the maximum cloud layer coverage scenario of two cloud layers -- initial and constrained Fu-Liou calculations for clear sky plus the two cloud layers (six calculations) -- 10 CERES FOVs can be processed per second. Neither of these assumptions are realistic, however, and are only included here to indicate the variability of the CPU time necessary for each CERES FOV. Cloud parameters in the 15-hour period were retrieved from AVHRR data sets, providing a more realistic sampling of cloud layers within a CERES FOV.

Test data sets simulating the CERES sampling rate contain about 180,000 Earth-viewing FOVs per hour, or 50 per second. In the 15-hour study, a total of 381,513 FOVs were processed in a total of 23,208 seconds of CPU time, suggesting that 16 FOVs can be processed per second. This is three times the CERES data rate. The hardware installed at the Langley DAAC will be equipped with multiple processors, thus enabling multiple SARB Subsystem jobs to be processed concurrently. This will enable SARB Subsystem processing to keep up with real time.

### 5.7. References

Alberta, T., and T. Charlock, 1997: Comparison of broadband radiative transfer calculations with surface and aircraft measurements during ARESE. Proceedings of the Ninth Conference on Atmospheric Radiation, Long Beach (Feb. 2-7, 1997), AMS, 22-25.

Barkstrom, B., E. Harrison, G. L. Smith, R. Green, J. Kibler, R. Cess, and the ERBE Science,1989: Earth Radiation Budget Experiment (ERBE) archival and April 1985 results. Bull. Amer. Meteor. Soc., 70, 1254-1262.

Briegleb, B., P. Minnis, V. Ramanthan, and E. Harrison, 1986: Comparison of regional and clear-sky albedos inferred from satellite observations and model computations. J. Clim. Appl. Meteor., 25, 214-226.

Cess, R., E. Dutton, J. DeLuisi, and F. Jiang, 1991: Determining surface solar absorption from broadband satellite measurements for clear skies: Comparisons with surface measurements. J. Clim., 4, 236-247.

Cess, R. D., M. H. Zhang, P. Minnis, L. Corsetti, E. G. Dutton, B. W. Forgan, D. P. Garber, W. L. Gates, J. J. Hack, E. F. Harrison, X. Jing, J. T. Kiehl, C. N. Long, J.-J. Morcrette, G. L. Potter, V. Ramanathan,

B. Subasilar, C. H. Whitlock, D. F. Young, and Y. Zhou, 1995: Absorption of solar radiation by clouds: Observations versus models. Science, 267, 496-499.

Chahine, M., 1992: The hydrological cycle and its influence on climate. Nature, 359, 373-380.

Charlock, T. P., and T. L. Alberta, 1996: The CERES/ARM/GEWEX Experiment (CAGEX) for the retrieval of radiative fluxes with satellite data. Bull. Amer. Meteor. Soc., Vol. 77, 2673-2683.

Charlock, T., and V. Ramanathan, 1985: The albedo field and cloud radiative forcing produced by a general circulation model with internally generated cloud optics. J. Atmos. Sci., 42, 1408-1429.

Charlock, T., F. Rose, D. Rutan, L. Coleman, B. Baum, and R. Green, 1997: The total-sky, global atmospheric radiation budget from radiative transfer calculations using ERBE, AVHRR, and sounding data. Proceeding of the Ninth Conference on Atmospheric Radiation, Long Beach (Feb. 2-7, 1997), AMS, 60-63.

Charlock, T., F. Rose, and G. Smith, 1990: A satellite retrieval of the shortwave heating of the atmosphere and the surface: Relationship to the general circulation, interannual climate variability, and the cryosphere. Proceeding of Seventh Conference on Atmospheric Radiation, San Francisco (23-27 July 1990), AMS, 137-141.

Charlock, T., F. Rose, S.-K. Yang, T. Alberta, and G. Smith, 1993: An observational study of the interaction of clouds, radiation, and the general circulation. Proceedings of IRS '92: Current Problems in Atmospheric Radiation, Tallinn (3-8 August 1992), A. Deepak Publishing, 151-154.

Chertock, B., R. Frouin, and R. Somerville, 1991: Global monitoring of net solar irradiance at the ocean surface: Climatological variability and the 1982-1983 El Nino. J. Climate, 4, 639-650.

Chou, M.-D., 1984: Broadband water vapor transmission functions for atmospheric IR flux computations. J. Atmos. Sci., 41, 1775-1778.

Chou, M.-D., 1992: A solar radiation model for use in climate studies. J. Atmos. Sci., 49, 762-772.

Chou, M.-D., A. Arking, J. Otterman, and W. L. Ridgway, 1995: The effect of clouds on atmospheric absorption of solar radiation. Geophys. Res. Lett., 22, 1885-1888.

Chou, M.-D., and L. Peng, 1983: A parameterization of the absorption of the 15 micrometer CO2 spectral region with application to climate sensitivity studies. J. Atmos. Sci., 40, 2183-2192.

Chou, M.-D., and W. Zhao, 1996: Estimation and model validation of surface solar radiation and cloud radiative forcing using TOGA COARE measurements. Submitted to J. Climate.

Churchill, D., 1992: Vertical retrieval of solar and infrared irradiances in the stratiform regions of EMEX cloud clusters. J. of Appl. Meteor., 31, 1229-1247.

Churchill, D., and R. Houze, Jr., 1991: Effects of radiation and turbulence on the diabatic heating and water budget of the stratiform region of a tropical cloud cluster. J. Atmos. Sci, 48, 903-922.

Clough, S. A., M. J. Iacono, and J.-L. Moncet, 1992: Line-by-line calculations of atmospheric fluxes and cooling rates: Application to water vapor. J. Geophys. Res., 97, 15761-15785.

Collins, W. D., and A. K. Inamdar, 1995: Validation of clear-sky fluxes for tropical oceans from the Earth Radiation Budget Experiment. J. Climate, 8, 569-578.

d'Almeida, G., P. Koepke, and E. P. Shettle, 1991: Atmospheric Aerosols - Global Climatology and Radiative Characteristics. A. Deepak Publishing, Hampton, Virginia. 561 pp.

Darnell, W., W. Staylor, S. Gupta, N. Ritchey, and A. Wilber, 1992: Seasonal variation of surface radiation budget derived from the International Satellite Cloud Climatology Project C1 data. J. Geophys. Res., 97, 15,741-15,760.

DeLuisi, J., 1991: Second Workshop on Implementation of the Baseline Surface Radiation Network. WCRP-64, WMO/TD No. 453.

Dickinson, R. E., 1983: Land surface processes and climate -- Surface albedos and energy balance. Advances in Geophysics, 25, 305-353.

Donner, L., 1988: An initialization for cumulus convection in numerical weather prediction models. Mon. Wea. Rev., 116, 377-385.

Donner, L., and H.-L. Kuo, 1984: Radiative forcing of stationary planetary waves. J. Atmos. Sci., 41, 2849-2868.

Dopplick, T., 1972: Radiative heating of the global atmosphere. J. Atmos. Sci., 29, 1278-1294.

Ellingson, R., and Y. Fouquart, 1990: Radiation and climate: Intercomparison of Radiation Codes in Climate Models (ICRCCM), World Climate Research Programme-39, 38 pp.

Ellingson, R., and J. Gille, 1978: An infrared radiative transfer model. Part I: Model description and comparison of observations with calculations. J. Atmos. Sci., 35, 523-545.

Ellingson, R., W. Wiscombe, J. DeLuisi, V. Kunde, H. Melfi, D. Murcray, and W. Smith, 1993: The Spectral Radiation Experiment (SPECTRE): Clear-sky observations and their use in ICRCCM and ITRA. Proceedings of IRS '92: Current Problems in Atmospheric Radiation, Tallinn (3-8 August 1992), A. Deepak Publishing, 451-453.

Ellingson, R. G., and W. J. Wiscombe, 1995: The Spectral Radiance Experiment (SPECTRE): Project description and sample results. Submitted to Bull. Amer. Meteor. Soc.

Ellingson, R. G., D. Yanuk, A. Gruber, and A. J. Miller, 1994: Development and application of remote sensing of longwave cooling from the NOAA polar orbiting satellites. Photogrammetric Engineering and Remote Sensing, 60, 307-316.

Feigelson, E., 1978: Preliminary radiation model of a cloudy atmosphere. Beitr. Phys. Atmosph., 51, 203-229.

Fu, Q., and K. Liou, 1993: Parameterization of the radiative properties of cirrus clouds. J. Atmos. Sci., 50, 2008-2025.

Fu, Q., K. Liou, M. Cribb, T. Charlock, and A Grossman, 1997: On multiple scattering in thermal infrared radiative transfer. Accepted for publication by J. Atmos. Sci.

Gates, W., 1992: AMIP: The Atmospheric Model Intercomparison Project. Bull. Amer. Meteor. Soc., 73, 1962-1970.

Gautier, C., and R. Frouin, 1992: Net surface solar irradiance variability in the central equatorial Pacific during 1982-1985. J. Climate, 5, 30-55.

Gupta, S., 1989: A parameterization for longwave surface radiation from sun-synchronous satellite data. J. Climate, 2, 305-320.

Gupta, S., W. Darnell, and A. Wilber, 1992: A parameterization for longwave surface radiation from satellite data: Recent improvements. J. Appl. Meteorol., 31, 1361-1367.

Harrison, L., J. Michalsky, and J. Berndt, 1994: Automated multifilter rotating shadow-band radiometer: An instrument for optical depth and radiation measurements. Appl. Opt., 33, 5118-5132.

Harshvardhan, R. Davies, D. Randall, and T. Corsetti, 1987: A fast radiation parameterization for atmospheric circulation models. J. Geophys. Res., 92, 1009-1016.

Hartmann, D., H. Hendon, and R. Houze, Jr., 1984: Some implications of the mesoscale circulations in tropical cloud clusters for large-scale dynamics and climate. J. Atmos. Sci., 41, 113-121.

Hayasaka, T., N. Kikuchi, and M. Tanaka, 1995: Absorption of solar radiation by stratocumulus clouds: Aircraft measurements and theoretical calculations. J. Appl. Meteor., 34, 1047-1055.

Heidinger, A., and S. Cox, 1994: Radiative surface forcing of boundary layer clouds. Eighth Conference on Atmospheric Radiation, Nashville, Tennessee, January 23-28, 1994, 246-248.

Hicks, B. B., J. J. DeLuisi, and D. R. Matt, 1996: The NOAA Integrated Surface Irradiance Study (ISIS) - a new surface radiation monitoring program. In press for Bull. Amer. Meteor. Soc.

Hlavka, D. L., J. D. Spinhirne, A. E. Galbraith, and J. A. Reagan, 1996: Full time lidar cloud and aerosol height distribution data sets to support radiation/climate forcing studies. Proceeding of the Ninth Conference on Atmospheric Radiation, Long Beach (Feb. 2-7, 1997), AMS, 81-84.

Hollingsworth, A., 1996: Flood and drought prediction: Results from operational medium-range forecasts and experimental seasonal forecasts at ECMWF. Preprint volume of the Second International Conference on the Global Energy and Water Cycle. 17-21 June 1996, FWashington, DC, p. 3.

Hoskins, B., 1996: On the existence and strength of the summer subtropical anticyclones. Bernard Haurwitz Memorial Lecture. Bull. Amer. Meteor. Soc., 77, 1287-1292.

Ignatov, A. M., L. Stowe, and S. M. Sakerin, 1994: Estimation of oceanic aerosol properties by simultaneous shipboard sun-photometer and satellite measurements. Proceedings of the Eighth Conference on Atmospheric Radiation, Nasheville, TN, Jan. 1994, AMS, pp. 389-391.

Inamdar, A., and V. Ramanathan, 1994: Physics of greenhouse effect and convection in warm oceans. J. Climate, in press.

Intergovernmental Panel on Climate Change (IPCC), 1990: Climate Change - The IPCC Scientific Assesment. Houghton, J., G. Jenkins, and J. Ephraums, Eds. Cambridge University Press. 364 pp.

International Global Atmospheric Chemistry Program (IGAC), 1994: The Operational Plan, Report No. 32 of the International Geosphere-Biosphere Program. Stockholm, Sweden, 134 pp.

Kalnay, E., M. Kanamitsu, R. Kistler, W. Collins, D. Deaven, L. Gandin, M. Iredell, S. Saha, G. White, J. Woolen, Y. Zhu, M. Chelliah, W. Ebisuzaki, W. Higgins, J. Janowiak, K. C. Mo, C. Ropelewski, J. Wang, A. Leetma, R. Reynolds, R. Jenne, and D. Joseph, 1996: The NCEP/NCAR 40-year Reanalysis Project. Bull. Amer. Meteor. Soc., 77, 437-471.

Kato, S., T. P. Ackerman, C. N. Long, E. Clothiaux, and J. Mather, 1996: A comparison between clear-sky shortwave flux calculatins and observations during ARESE. Presentation to ARM Science Team Meeting, San Antonio Texas, March 4-7, 1996.

Kiehl., J., and B. Briegleb, 1992: Comparison of observed and calculated clear-sky greenhouse effect. J. Geophys. Res., 97, 10,037-10,049.

Kinne, S., 1996: Cloud inhomogeneity effects on radiative transfer. Presentation to ARM Science Team Meeting, San Antonio Texas, March 4-7, 1996.

Kratz, D., 1995: The corrrelated k-distribution technique as applied to the AVHRR channels. JQRST, Vol. 53, 501-517.

Kratz, D., 1997: The use of correlated d-distributions to account for the radiative effect of molecular absorption upon satellite measured radiances. Conference on Atmospheric Radiation, Long Beach (Feb. 2-7, 1997), AMS, 184-185.

Lee, H.-T., R. Ellingson, and D. Yanuk, 1993: Estimation of longwave radiation budget parameters with HIRS radiances. Proceedings of IRS '92: Current Problems in Atmospheric Radiation, Tallinn (3-8 August 1992), A. Deepak Publishing, 224-226.

Leese, J. (compiler), 1995: Major Activities Plan for 1996, 1997 & Outlook for 1998 for the GEWEX Continental-Scale International Project (GCIP). World Climate Research Program (WCRP) and International GEWEX Project Office (IGPO). IGPO Publication Series No. 16 (see pp. I3-I8).

Li, Z., H. W. Barker, and L. Moreau, 1995: The variable effect of clouds on atmospheric absorption of solar radiation. Nature, 376, 486-490.

Li, Z., and H. Leighton, 1993: Global climatologies of solar radiation budgets at the surface and in the atmosphere from 5 years of ERBE data. J. Geophys. Res., 98, 4919-4930.

Li, Z., H. Leighton, K. Masuda, and T. Takashima, 1993: Estimation of SW flux absorbed at the surface from TOA reflected flux. J. Climate, 6, 317-330.

Liou, K.-N., 1992: Radiation and Cloud Processes in the Atmosphere, Oxford University Press, 487 pp.

Liou, K.-N., Q. Fu, and T. Ackerman, 1988: A simple formulation of the delta-four-stream approximation for radiative transfer parameterizations. J. Atmos. Sci., 45, 1940-1947.

London, J., 1957: A study of the atmospheric heat balance. New York University Final Report No. AF19(122)-165, AFCRC-TR-57-287, ASTIA no. 117227, 99 pp.

Lorenz, E., 1955: Available potential energy and the maintenance of the general circulation. Tellus, 7, 157-167.

Manabe, S., and R. Wetherald, 1967: Thermal equilibrium of the atmosphere with a given distribution of relative humidity. J. Atmos. Sci., 24, 241-259.

Michalsky, J., M. Rubes, T. Stoffel, M. Wesely, M. Splitt, and J. DeLuisi, 1997: Optimal measurement of surface shortwave irradiance using current instrumentation -- The ARM experience. Proceeding of the Ninth Conference on Atmospheric Radiation, Long Beach (Feb. 2-7, 1997), AMS, 60-63.

Minnis, P., K.-N. Liou, and Y. Takano, 1993a: Inference of cirrus cloud properties using satellite-observed visible and infrared radiances. Part I: Parameterization of radiance fields. J. Atmos. Sci., 50, 1279-1304.

Minnis, P., K.-N. Liou, and Y. Takano, 1993b: Inference of cirrus cloud properties using satellite-observed visible and infrared radiances. Part II: Verification of theoretical cirrus radiative properties. J. Atmos. Sci., 50., 1305-1322.

Minnis, P., W. L. Smith, Jr., D. P. Garber, J. K. Ayers, and D. R. Doelling, 1995: Cloud properties derived from GOES-7 for spring 1994 ARM Intensive Observing Period using Version 1.0.0 of ARM satellite data analysis program. NASA Reference Publication 1366, 58 pp.

O'Hirok, W., and C. Gautier, 1996: The role of three-dimensional clouds on atmospheric absorption. Presentation to ARM Science Team Meeting, San Antonio Texas, March 4-7, 1996.

Ohmura, A., and H. Gilgen, 1993: Re-evaluation of the global energy balance. Geophysical Monograph 75, IUGG Volume 15, 93-110.

Paltridge, G., 1974: Atmospheric radiation and the gross character of stratiform cloud. J. Atmos. Sci., 31, 244-250.

Payne, R. E., 1972: Albedo of the sea surface. J. Atmos. Sci., 29, 959-970.

Penner, J. E., R. J. Charlson, J. M. Hales, N. S. Leifer, R. Novakov, J. Ogren, L. F. Radke, S. E. Schwartz, and L. Travis, 1994: Quantifying and minimizing the uncertainty of climate forcing by anthropogenic aerosols. Bull. Amer. Meteor. Soc., 75, 375-400.

Pilewskie, P., and F. P. J. Valero, 1995: Direct observations of excess solar absorption by clouds. Science, 267, 1626-1629.

Pinker, R., and I. Laszlo, 1992: Modeling surface solar irradiance for satellite applications on a global scale. J. Appl. Meteor., 31, 194-211.

Polak, E., 1971: Computational Methods in Optimization. Academic Press, New York.

Prata, A. J., 1993: Land surface temperatures derived from the advanced very high resolution radiometer and the along-track scanning radiometer 1. Theory. J. Geophys. Res., 98, 16,689-16,702.

Press, W. H., B. P. Flannery, S. A Teukolsky, W. T. Vetterling, 1986: Numerical Recipes. Cambridge University Press. pp. 274-334.

Ramanathan, V., 1987: Atmospheric general circulation and its low frequency variance: Radiative influences. J. Meteor. Soc. Japan, 65, 151-175.

Ramanathan, V., and R. Dickinson, 1979: The role of stratospheric ozone in the zonal and seasonal radiative energy balance of the earth-troposphere system. J. Atmos. Sci., 36, 1084-1104.

Ramanathan, V., E. Pitcher, R. Malone, and M. Blackmon, 1983: The response of a spectral general circulation model to refinements in radiative processes. J. Atmos. Sci., 40, 605-630.

Ramaswamy, V., and S. Freidenreich, 1992: A study of broadband paremeterizations of the solar radiative interactions with water vapor and water drops. J. Geophys. Res., 97, 11,487-11,512.

Randall, D., Harshvardhan, D. Dazlich, and T. Corsetti, 1989: Interactions among radiation, convection, and large-scale dynamics in a general circulation model. J. Geophys. Res., 46, 1943-1970.

Reynolds, R. W., and T. M. Smith, 1994: Improved global sea surface temperature analyses using optimum interpolation. J. of Climate, 7, 929-948.

Raval, A., V. Ramanathan, 1989: Observational determination of the greenhouse effect. Nature, 342, 758-761.

Ritter, B., and J.-F. Geleyn, 1992: A comprehensive radiation scheme for numerical weather prediction models with potential applications in climate simulations. Mon. Wea. Rev., 120, 303-325.

Rockel, B., E. Raschke, and B. Weyres, 1991: A parameterization of broadband radiative transfer properties of water, ice, and mixed clouds. Beitr. Phys. Atmosph., 64, 1-12.

Rodgers, C., 1968: Some extension and applications of the new random model for molecular band transmission. Quart. J. Roy. Meteor. Soc., 94, 99-102.

Roberts, R. E., J. E. A. Selby, and L. M. Biberman, 1976: Infrared continuumn absorption by atmospheric water vapor in the 8-12 mm window. Appl. Opt., 15, 2085-2090.

Rose, F., T. Charlock, D, Rutan, and G. L. Smith, 1997: Tests of a constrainment algorithm for the surface and atmospheric radiation budget. Proceedings of the Ninth Conference on Atmospheric Radiation, Long Beach (Feb. 2-7, 1997), AMS, 466-469

Rossow, W., L. Garder, P. Lu, and A. Walker, 1991: International Satellite Cloud Climatology Project (ISCCP) Documentation of Cloud Data. In WMO/TD-No.266 (Revised). World Meteorological Organization, Geneva, 76 pp.

Rutan, D., and T. Charlock, 1997: Spectral reflectance, directional reflectance, and broadband albedo of the earth's surface. Proceedings of the Ninth Conference on Atmospheric Radiation, Long Beach (Feb. 2-7, 1997), AMS, 466-469.

Salisbury, J., and D. D'Aria, 1992: Emissivity of terrestrial materials in the 8-14 μm atmospheric window. Remote Sens. Environ., 42, 83-106.

Schiffer, R., and W. Rossow, 1983: ISCCP global radiance data set: A new resource for climate research. Bull. Amer. Meteor. Soc., 66, 1498-1505.

Schmetz, J., 1984: On the parameterization of the radiative properties of broken clouds. Tellus, 36, 417-432.

Schubert, S., C.-K. Park, C.-Y. Wu, W. Higgins, Y. Kondratyeva, A. Molod, L Takacs, M. Seablom, R. Rood, 1995: A Multiyear assimilation with the GEOS-1 system: Overview and results. NASA TM 104606, Vol. 6, 183 pp.

Schuster, G., C. Whitlock, J. Plant, R. Wheeler, C. Moats, and K. Larman, 1997: Season and vegetational variation in albedo measured during CERES ground validation pilot study. Conference on Atmospheric Radiation, Long Beach (Feb. 2-7, 1997), AMS, 456-459.

Sellers, P., and F. Hall, 1992: FIFE in 1992: Results, scientific gains, and future research directions. J. Geophys. Res., 97, 19,091-19,109.

Slingo, A., and J. Slingo, 1988: The response of a general circulation model to cloud longwave radiative forcing. I: Introduction and initial experiments. Quart. J. Roy. Meteor. Soc., 114, 1027-1062.

Slingo, J., and A. Slingo, 1991: The response of a general circulation model to cloud longwave radiative forcing. II: Further studies. J. Atmos. Sci., 117, 333-364.

Slingo, A., and M. Webb, 1992: Simulation of clear-sky outgoing longwave radiation over the oceans using operational analyses. Quart. J. Roy. Meteorol. Soc., 118, 1117-1144.

Soden, B. J., S. A. Ackerman, D. O'C. Starr, S. H. Melfi, and R. A. Ferrare, 1994: Comparison of upper tropospheric water vapor from GOES, Raman lidar, and CLASS sonde measurements. J. Geophys. Res., 99, 21 005-21 016.

Spinhirne, J. D., 1991: Visible and near IR lidar backscatter observations on the GLOBE Pacific survey missions. Preprint Volume of the Seventh Symposium on Meteorological Observations and Instrumentation, AMS (Boston MA), pp. J261-J264.

Spinhirne, J. D., 1993: Micro Pulse Lidar. IEEE Trans. Geosc. Rem. Sens., 31, 48-55.

Spinhirne, J. D., S. Chudamani, and A. D. Clarke, 1996: Distribution of aerosol scattering throughout the Pacific Basin regions from observations. Proceeding of the Ninth Conference on Atmospheric Radiation, Long Beach (Feb. 2-7, 1997), AMS, 33-36.

Stackhouse Jr., P., and G. Stephens, 1991: A theoretical and observational study of the radiative properties of cirrus: Results from FIRE 1986. J. Atmos. Sci., 48, 2044-2059.

Stamnes, K., and P. Conklin, 1984: A new multi-layer discrete ordinate approach to radiative transfer in vertically inhomogeneous atmospheres. J. Quant. Spectrosc. Radiat. Transfer, 31, 273-282.

Staylor, W. F., and A. C. Wilber, 1990: Global surface albedos estimated from ERBE data. Proceeding of Seventh Conference on Atmospheric Radiation, San Francisco (23-27 July 1990), AMS, 231-236.

Stephens, G., and T. Greenwald, 1991: The Earth's radiation budget and its relation to atmospheric hydrology: 1. Observations of the clear-sky greenhouse effect. J. Geophys. Res., 96, 15,325-15,340.

Stephens, G., A. Slingo, M. Webb, P. Minnett, P. Daum, L. Kleinman, I. Wittmeyer, and D. Randall, 1993: Observations of the Earth's radiation budget in relation to atmospheric hydrology. Part IV: Atmospheric column radiative cooling over the world's oceans. Submitted to J. Geophys. Res.

Stephens, G., and S. Tsay, 1990: On the cloud absorption anomaly. Quart. J. Roy. Meteorol. Soc., 116, 671-704.

Stephens, G., and P. Webster, 1984: Cloud decoupling of the surface and planetary radiative budgets. J. Atmos. Sci., 41, 681-686.

Stokes, G., and S. Schwartz, 1994: The Atmospheric Radiation Measurement (ARM) Program: Programmatic background and design of the cloud and radiation testbed. Bull. Amer. Meteor. Soc., 75, 1201.

Stowe, L., C. Wellemeyer, T. Eck, H. Yeh, and the Nimbus-7 Cloud Data Processing Team, 1988: Nimbus-7 global cloud climatology. Part I: Algorithms and validation. J. Climate, 1, 445-470.

Stuhlmann, R., E. Raschke, and U. Schmid, 1993: Cloud generated radiative heating from METEOSAT data. Proceedings of IRS '92: Current Problems in Atmospheric Radiation, Tallinn (3-8 August 1992), A. Deepak Publishing, 69-75.

Stuhlmann, R., and G. Smith, 1988a: A study of cloud-generated radiative heating and its generation of available potential energy. Part I: Theoretical background. J. Atmos. Sci., 45, 3911-3927.

Stuhlmann, R., and G. Smith, 1988b: A study of cloud-generated radiative heating and its generation of available potential energy. Part II: Results for a climatological zonal mean January. J. Atmos. Sci., 45, 3928-3943.

Takano, Y., and K.-N. Liou, 1994: Light scattering by irregularly shaped ice crystals: Climatic implications. Eighth Conference on Atmospheric Radiation, Nashville, Tennessee, January 23-28, 1994, 440-442.

Tao, W.-K., J. Simpson, C.-H. Sui, B. Ferrier, S. Lang, J. Scala, M.-D. Chou, K. Pickering, 1993: Heating, moisture, and water budgets of tropical and midlatitude squall lines: Comparisons and sensitivity to longwave radiation. J. Atmos. Sci., 50, 673-690.

Ting, M., and P. Sardeshmukh, 1993: Factors determining the extratropical response to equatorial diabatic heating anomalies. J. Atmos. Sci., 50, 907-918.

Valero, F. P. J., B. Bush, S. Pope, A. Bucholtz, and P. Flatau, 1996: MODTRAN simulations relevant to the ARESE campaign. Presentation to ARM Science Team Meeting, San Antonio Texas, March 4-7, 1996

Waliser, D. E., W. D. Collins, S. P. Anderson, 1996: An estimate of the surface shortwave cloud forcing over the Western Pacific during TOGA COARE. Geophys. Res. Lett., 23, 519-522.

Wan, Z., and J. Dozier, 1989: Land-surface temperature measurement from space: Physical principles and inverse modeling. IEEE Trans. Geosci. and Remote Sensing, 27, 268-278.

Wang, W.-C., and G.-Y. Shi, 1988: Total band absorptance and k-distribution function for atmospheric gases. J. Quant. Spectrosc. Radiat. Transfer, 39, 387-397.

Wang, W.-C., G.-Y. Shi, and J. Kiehl, 1991: Incorporation of the thermal radiative effect of CH4, N2O, CF2Cl2, and CFCl3 into the National Center for Atmospheric Research Community Climate Model. J. of Geophys. Res., 96, 9097-9103.

Whitlock, C. H., T. P. Charlock, W. F. Staylor, R. T. Pinker, I. Laszlo, A. Ohmura, H. Gilgen, T. Konzelman, R. C. DiPasquale, C. D. Moats, S. R. LeCroy, and N. A. Ritchey, 1995: First global WCRP shortwave Surface Radiation Budget dataset. Bull. Amer. Meteor. Soc., 76, 905-922.

Whitlock, C. H., S. R. LeCroy, and R. J. Wheeler, 1994: Narrowband angular reflectance properties of the alkali flats at White Sands, New Mexico. Remote Sens. Environ., 50, 171-181.

Wielicki, B., and R. Green, 1989: Cloud identification for ERBE radiative flux retrieval. J. Appl. Meteor., 28, 1133-1146.

Wielicki, B., and L. Parker, 1992: On the determination of cloud cover from satellite sensors: The effect of sensor spatial resolution. J. Geophys. Res., 97, 12,799-12,823.

Wild, M., A. Ohmura, H. Gilgen, and E. Roeckner, 1995: Validation of general circulation model radiative fluxes using surface observations. J. Climate, 8, 1309-1324.

World Climate Research Program (WCRP), 1992: Scientific Plan for the GEWEX Continental-Scale International Project (GCIP). WCRP-67 WMO/TD-No. 461.

Wu, M., and L.-P. Chang, 1992: Longwave radiation budget parameters computed from ISCCP and HIRS2/MSU products. J. Geophys. Res., 97, 10,083-10,101.

# Appendix A - Input Data Products

## Compute Surface and Atmospheric Fluxes (Subsystem 5)

This appendix describes the data products which are produced by the algorithms in this subsystem. The table below summarizes these products, listing the CERES and EOSDIS product codes or abbreviations, a short product name, the product type, the production frequency, and volume estimates for each individual product as well as a complete data month of production. The product types are defined as follows:

| | |
|---|---|
| Archival products: | Assumed to be permanently stored by EOSDIS |
| Internal products: | Temporary storage by EOSDIS (days to years) |

The following pages describe each product. An introductory page provides an overall description of the product and specifies the temporal and spatial coverage. The table which follows the introductory page briefly describes every parameter which is contained in the product. Each product may be thought of as metadata followed by data records. The metadata (or header data) is not well-defined yet and is included mainly as a placeholder. The description of parameters which are present in each data record includes parameter number (a unique number for each distinct parameter), units, dynamic range, the number of elements per record, an estimate of the number of bits required to represent each parameter, and an element number (a unique number for each instance of every parameter). A summary at the bottom of each table shows the current estimated sizes for metadata, each data record, and the total data product. A more detailed description of each data product will be contained in a User's Guide to be published before the first CERES launch.

Table A-1. Output Products Summary

| Product Code | | Name | Type | Frequency | Size, MB | Monthly Size, MB |
|---|---|---|---|---|---|---|
| CERES | EOSDIS | | | | | |
| MOA | CERX06 | Meteorological, Ozone, and Aerosol Data | Archival | 1/Hour | 11.55 | 8591 |
| SSF | CER11 | Single Satellite Footprint, TOA and Sfc Flux, Clouds | Archival | 1/Hour | 226.61 | 168598 |

## Meteorological, Ozone, and Aerosol Data (MOA)

The CERES archival product Meteorological, Ozone, and Aerosol Data (MOA) is produced by the CERES Regrid MOA Subsystem. Each MOA file contains meteorological, ozone, and aerosol data for one hour, and is used by several of the CERES subsystems. Data on the MOA are derived from several data sources external to the CERES system, such as the Data Assimilation Office (DAO), NOAA, and various other

meteorological satellites. These data arrive anywhere from four times daily to once a month, and have various horizontal resolutions. The Regrid MOA Subsystem interpolates the aerosol and ozone data horizontally to conform with the horizontal resolution of the meteorological data. Profile data are interpolated vertically to conform with CERES requirements. All data are temporally interpolated to provide data to the CERES processing system on an hourly basis.

The MOA contains:

- Surface pressure, geopotential height, skin temperature, and sea surface state
- Vertical profiles of temperature and humidity for 58 atmospheric levels
- Vertical profiles for 18 atmospheric levels below the tropopause of wind u-vector and v-vector data
- Tropospheric height
- Air mass index
- Column precipitable water based on humidity profiles
- Column precipitable water based on microwave measurements
- Column averaged relative humidity
- Vertical profile of ozone mixing ratios for 58 atmospheric levels
- Column ozone
- Aerosol optical depth

**Level:** 3
**Type:** Archival
**Frequency:** 1/Hour

**Time Interval Covered**
**File:** 1 hour
**Record:** 1 hour

**Portion of Globe Covered**
**File:** Global
**Record:** One region

**Portion of Atmosphere Covered**
**File:** Surface to TOA

## Table A-2 Meteorological, Ozone, and Aerosol (MOA)

| Description | Parameter Number | Units | Range | Elements/ Record | Bits/Elem ElemNum |
|---|---|---|---|---|---|
| **Header** | | | | | |
| Date and Hour | | N/A | ASCII string | 1 | 216 |
| MOA Processing Date | | N/A | ASCII string | 1 | 216 |
| MOA Grid Index | | N/A | 1 .. 1 | 1 | 16 |
| Number of MOA Regions | | N/A | 13104 .. 13104 | 1 | 32 |
| Temperature, Humidity, and Ozone Profile Fixed Pressure Levels | | hPa | 0 .. 1100 | 55 | 32 |
| Wind Speed Profile Pressure levels | | hPa | 0 .. 1100 | 18 | 32 |
| **Surface Data** | | | | | |
| MOA Region Number | 1 | N/A | 1 .. 13104 | 1 | 321 |
| Surface Pressure | 2 | hPa | 0 .. 1100 | 1 | 322 |
| Surface Geopotential Height | 3 | m | -100 .. 10000 | 1 | 323 |
| Surface Skin Temperature | 4 | K | 175 .. 375 | 1 | 324 |
| Flag, Sea Surface State | 5 | N/A | 0 .. 9 | 1 | 325 |
| Flag, Source Surface Data | 6 | N/A | TBD | 1 | 326 |
| **Meteorological Profiles** | | | | | |
| Temperature Profiles | 7 | K | 175 .. 375 | 58 | 327 |
| Specific Humidity Profiles | 8 | N/A | 0 .. 100 | 58 | 3265 |
| Wind Profile, U-Vector | 9 | m $sec^{-1}$ | -100 .. 100 | 18 | 32123 |
| Wind Profile, V-Vector | 10 | m $sec^{-1}$ | -100 .. 100 | 18 | 32141 |
| Flag, Source Meteorological Profiles | 11 | N/A | TBD | 1 | 32159 |
| **Meteorological Column Data** | | | | | |
| Tropospheric Height | 12 | hPa | 150 .. 300 | 1 | 32160 |
| Air Mass Index | 13 | N/A | 0 .. 10 | 1 | 32161 |
| Precipitable Water | 14 | cm | 0.001 .. 10.000 | 1 | 32162 |
| Column Averaged Relative Humidity | 15 | N/A | 0 .. 100 | 1 | 32163 |
| Microwave Precipitable Water | 16 | cm | 0.001 .. 10.000 | 1 | 32164 |
| Microwave Precipitable Water, std | 17 | cm | TBD | 1 | 32165 |
| Flag, Source Microwave Column Precipitable Water | 18 | N/A | TBD | 1 | 32166 |
| **Ozone Profile Data** | | | | | |
| Ozone Mixing Ratio Profiles | 19 | g $kg^{-1}$ | 0.00002 .. 0.02 | 58 | 32167 |
| Flag, Source Ozone Profile Data | 20 | N/A | TBD | 1 | 32225 |
| **Column Ozone** | | | | | |
| Column Ozone | 21 | du | 0 .. 500 | 1 | 32226 |
| Flag, Source Column Ozone | 22 | N/A | TBD | 1 | 32227 |
| **Total Column Aerosol** | | | | | |
| Optical Depth, Total Column | 23 | g $m^{-2}$ | 0 .. 2 | 1 | 32228 |
| Flag, Source Optical Depth, Total Column | 24 | N/A | TBD | 1 | 32229 |
| Spares | 25 | N/A | TBD | 2 | 32230 |

| | |
|---|---|
| Total Header Bits/File: | 544 |
| Total Data Bits/Record: | 7392 |
| Total Records/File: | 13104 |
| Total Data Bits/File: | 96864768 |
| Total Bits/File: | 96865312 |

## Single Satellite Footprint, TOA and Sfc Flux, Clouds (SSF)

**EOSDIS Product Code:** CER11

The Single Satellite CERES Footprint TOA and Surface Fluxes, Clouds (SSF) is produced from the cloud identification, convolution, inversion, and surface processing for CERES. Each SSF covers a single hour swath from a single CERES scanner (3 channels) mounted on one satellite. The product has a product header and multiple records of 113 parameters or 261 elements for each footprint.

The major categories of data output on the SSF are

- CERES footprint geometry and CERES viewing angles
- CERES footprint radiance and flux (TOA and Surface)
- CERES footprint area statistics and imager viewing angles
- CERES footprint clear area statistics
- CERES footprint cloudy area statistics for two out of four cloud height categories
  - Visible optical depth (mean and standard deviation)
  - Logarithm of visible optical depth (mean and standard deviation)
  - Infrared emissivity (mean and standard deviation)
  - Liquid water path (mean and standard deviation)
  - Ice water path (mean and standard deviation)
  - Cloud top pressure (mean and standard deviation)
  - Cloud effective pressure (mean and standard deviation)
  - Cloud effective temperature (mean and standard deviation)
  - Cloud effective height (mean and standard deviation)
  - Cloud bottom pressure (mean and standard deviation)
  - Water particle radius (mean and standard deviation)
  - Ice particle effective diameter (mean and standard deviation)
  - Particle phase (mean and standard deviation)
  - Vertical aspect ratio (mean and standard deviation)
  - Visible optical depth and IR emissivity (13 percentiles)
- CERES footprint cloud overlap conditions (4 conditions)

The SSF is an archival product that will be run daily in validation mode starting with the TRMM launch until sufficient data have been collected and analyzed to produce a production quality set of CERES Angular Distribution Models (CADM). It is estimated that at TRMM launch plus 18 to 24 months, the SSF product will be produced on a routine basis and will be archived within EOSDIS for distribution to the science community.

**Level:** 2
**Type:** Archival
**Frequency:** 1/Hour
**Time Interval Covered**
**File:** 1 Hour
**Record:** 1/100 Second

**Portion of Globe Covered**
**File:** Satellite Footprints
**Record:** One Footprint
**Portion of Atmosphere Covered**
**File:** Surface to TOA

Table A-3 Single Satellite Footprint (SSF) (1 of 3)

| Description Product | Parameter Number | Units | Range | Elements/Record | Bits/Elem | Code |
|---|---|---|---|---|---|---|
| **SSF** | | | | | | |
| **SSF_Header** | | | | | | |
| 1 Day and Time at hour start | | N/A | ASCII string | 1 | 216 | A |
| 2 Character name of satellite | | N/A | ASCII string | 1 | 64 | A |
| 3 Character name of CERES instrument | | N/A | ASCII string | 1 | 32 | A |
| 4 Character name of high resolution imager instrument | | N/A | ASCII string | 1 | 64 | A |
| 5 Number of imager channels used | | N/A | 1 .. 20 | 1 | 16 | A |
| 6 Central wavelengths of imager channels | | μm | 0.4 .. 15.0 | 2 | 32 | A |
| 7 Earth-Sun distance | | AU | 0.98 .. 1.02 | 1 | 32 | A |
| 8 Day and Time IES processed (SS1.0) | | N/A | ASCII string | 1 | 152 | V |
| 9 Day and Time Imager Cloud properties processed (SS4-1 - 4.3) | | N/A | ASCII string | 1 | 152 | V |
| 10 Day and Time Convolution of imager with CERES processed (SS4.4) | | N/A | ASCII string | 1 | 152 | V |
| 11 Day and Time TOA and Surface Estimation processed (SS4.5 - 4.6) | | N/A | ASCII string | 1 | 152 | A |
| 12 Number of Footprints in SSF product | | N/A | 0.. 245475 | 1 | 32 | A |
| **SSF_Record** | | | | | | |
| **Footprint Geometry** | | | | | | |
| **Time and Position** | | | | | | |
| 1 Time of observation | 1 | day | -0.01 ..1.01 | 1 | 64 | A |
| 2 Radius of satellite from center of Earth at observation | 2 | km | 6000..8000 | 1 | 64 | A |
| 3 Colatitude of satellite at observation | 3 | deg | 0..180 | 1 | 32 | A |
| 4 Longitude of satellite at observation | 4 | deg | 0..360 | 1 | 32 | A |
| 5 Colatitude of Sun at observation | 5 | deg | 0..180 | 1 | 32 | A |
| 6 Longitude of Sun at observation | 6 | deg | 0..360 | 1 | 32 | A |
| 7 Colatitude of CERES FOV at TOA | 7 | deg | 0..180 | 1 | 32 | A |
| 8 Longitude of CERES FOV at TOA | 8 | deg | 0..360 | 1 | 32 | A |
| 9 Colatitude of CERES FOV at surface | 9 | deg | 0..180 | 1 | 32 | A |
| 10 Longitude of CERES FOV at surface | 10 | deg | 0..360 | 1 | 32 | A |
| 11 Scan sample number | 11 | N/A | 1..660 | 1 | 16 | A |
| 12 Packet number | 12 | N/A | 0..32767 | 1 | 16 | A |
| 13 Cone angle of CERES FOV at satellite | 13 | deg | 0..90 | 1 | 32 | A |
| 14 Clock angle of CERES FOV at satellite wrt inertial velocity | 14 | deg | 0..360 | 1 | 32 | A |
| 15 Rate of change of cone angle | 15 | deg $sec^{-1}$ | -100 .. 100 | 1 | 32 | A |
| 16 Rate of change of clock angle | 16 | deg $sec^{-1}$ | -10 .. 10 | 1 | 32 | A |
| 17 Along-track angle of CERES FOV at TOA | 17 | deg | 0 .. 360 | 1 | 32 | A |
| 18 Cross-track angle of CERES FOV at TOA | 18 | deg | -90..90 | 1 | 32 | A |
| 19 X component of satellite inertial velocity | 19 | km $sec^{-1}$ | -10 ..10 | 1 | 64 | A |
| 20 Y component of satellite inertial velocity | 20 | km $sec^{-1}$ | -10 ..10 | 1 | 64 | A |
| 21 Z component of satellite inertial velocity | 21 | km $sec^{-1}$ | -10 ..10 | 1 | 64 | A |
| **CERES Viewing Angles** | | | | | | |
| 22 CERES viewing zenith at TOA | 22 | deg | 0 .. 90 | 1 | 32 | A |
| 23 CERES solar zenith at TOA | 23 | deg | 0 .. 180 | 1 | 32 | A |
| 24 CERES relative azimuth at TOA | 24 | deg | 0..360 | 1 | 32 | A |
| 25 CERES viewing azimuth at TOA wrt North | 25 | deg | 0..360 | 1 | 32 | V |
| **Surface_Map Parameters** | | | | | | |
| 26 Altitude of surface above sea level | 26 | m | -1000 .. 10000 | 1 | 32 | A |
| 27 Surface type index | 27 | N/A | 1 .. 20 | 1 | 8 | A |
| 28 Surface type percent coverage | 28 | N/A | 0 .. 100 | 1 | 8 | A |
| **Scene_Type** | | | | | | |
| 29 CERES SW ADM type for inversion process | 29 | N/A | 0 .. 200 | 1 | 16 | A |

| | | | | | |
|---|---|---|---|---|---|
| | 30 CERES LW ADM type for inversion process | 30 | N/A | 0 .. 600 | 116A |
| | 31 CERES WN ADM type for inversion process | 31 | N/A | 0 .. 600 | 116A |
| **Footprint Radiation** | | | | | |
| **CERES Filtered Radiances** | | | | | |
| | 32 CERES TOT filtered radiance, upwards | 32 | W $m^{-2}$ $sr^{-1}$ | 0..700 | 132I |
| | 33 CERES SW filtered radiance, upwards | 33 | W $m^{-2}$ $sr^{-1}$ | -10..510 | 132I |
| | 34 CERES WN filtered radiance, upwards | 34 | W $m^{-2}$ $sr^{-1}$ | 0..50 | 132I |
| | 35 IES quality flags | 35 | N/A | see Table TBD | 132A |
| **CERES Unfiltered Radiances** | | | | | |
| | 36 CERES SW radiance, upwards | 36 | $Wm^{-2}$ $sr^{-1}$ | -10 .. 510 | 132A |
| | 37 CERES LW radiance, upwards | 37 | $Wm^{-2}$ $sr^{-1}$ | 0 .. 200 | 132A |
| | 38 CERES WN radiance, upwards | 38 | $Wm^{-2}$ $sr^{-1}$ | 0 .. 50 | 132A |
| **TOA and Surface Flux** | | | | | |
| | 39 CERES SW flux at TOA, upwards | 39 | $Wm^{-2}$ | 0 .. 1400 | 132A |
| | 40 CERES LW flux at TOA, upwards | 40 | $Wm^{-2}$ | 0 .. 500 | 132A |
| | 41 CERES WN flux at TOA, upwards | 41 | $Wm^{-2}$ | 10 .. 400 | 132A |
| | 42 CERES downward SW surface flux, Model A | 42 | $Wm^{-2}$ | 0 .. 1400 | 132A |
| | 43 CERES downward LW surface flux, Model A | 43 | $Wm^{-2}$ | 0 .. 700 | 132A |
| | 44 CERES downward WN surface flux, Model A | 44 | $Wm^{-2}$ | 0 .. 700 | 132A |

Table A-3 Single Satellite Footprint (SSF) (2 of 3)

| **Description** | **Parameter Number** | **Units** | **Range** | **Elements/Record** | **Bits/Elem** | **Code** |
|---|---|---|---|---|---|---|
| | 45 CERES downward nonWN surface flux, Model A | 45 | $Wm^{-2}$ | 0 .. 700 | | 132A |
| | 46 CERES net SW surface flux, Model A | 46 | $Wm^{-2}$ | 0 .. 1400 | | 132A |
| | 47 CERES net LW surface flux, Model A | 47 | $Wm^{-2}$ | -250 .. 50 | | 132A |
| | 48 CERES downward SW surface flux, Model B (TBD) | 48 | $Wm^{-2}$ | 0 .. 1400 | | 132A |
| | 49 CERES downward LW surface flux, Model B | 49 | $Wm^{-2}$ | 0 .. 700 | | 132A |
| | 50 CERES net SW surface flux, Model B (TBD) | 50 | $Wm^{-2}$ | 0 .. 1400 | | 132A |
| | 51 CERES net LW surface flux, Model B | 51 | $Wm^{-2}$ | -250 .. 50 | | 132A |
| | 52 CERES spectral reflectivity | 52 | N/A | 0 .. 1 | | 632I |
| | 53 CERES broadband surface albedo | 53 | N/A | 0 .. 1 | | 132I |
| | 54 CERES LW surface emissivity | 54 | N/A | 0 .. 1 | | 132I |
| | 55 CERES WN surface emissivity | 55 | N/A | 0 .. 1 | | 132I |
| | 56 Imager-based surface skin temperature | 56 | K | 175 .. 375 | | 132I |
| **Full Footprint Area** | | | | | | |
| | 57 Number of imager pixels in CERES FOV | 57 | N/A | 0 .. 9000 | | 116A |
| | 58 Imager percent coverage | 58 | N/A | 0..100 | | 116A |
| | 59 Precipitable water | 59 | cm | 0.001 .. 10 | | 132A |
| | 60 Shadowed pixels percent coverage (TBD) | 60 | N/A | 0 .. 100 | | 116A |
| | 61 Notes on general procedure | 61 | N/A | TBD | | 116A |
| | 62 Notes on Cloud Algorithms | 62 | N/A | TBD | | 116A |
| | 63 Mean imager viewing zenith over CERES FOV | 63 | deg | 0 .. 90 | | 132A |
| | 64 Mean imager relative azimuth over CERES FOV | 64 | deg | 0 .. 360 | | 132A |
| | 65 Imager channel identifier | 65 | N/A | 1 .. 20 | | 516A |
| | 66 5th percentile of imager radiances over CERES FOV | 66 | W $m^{-2}$ $sr^{-1}$ $\mu m^{-1}$ | TBD | | 532V |
| | 67 Mean of imager radiances over CERES FOV | 67 | W $m^{-2}$ $sr^{-1}$ $\mu m^{-1}$ | TBD | | 532A |
| | 68 95th percentile of imager radiances over CERES FOV | 68 | W $m^{-2}$ $sr^{-1}$ $\mu m^{-1}$ | TBD | | 532V |
| **Clear Footprint Area** | | | | | | |
| | 69 Sunglint percent coverage | 69 | N/A | 0 .. 100 | | 116A |
| | 70 Snow/Ice percent coverage | 70 | N/A | 0 .. 100 | | 116A |
| | 71 Smoke percent coverage | 71 | N/A | 0 .. 100 | | 116A |
| | 72 Fire percent coverage | 72 | N/A | 0 .. 100 | | 116A |
| | 73 Mean of imager radiances over clear area | 73 | W $m^{-2}$ $sr^{-1}$ $\mu m^{-1}$ | TBD | | 532A |
| | 74 Stddev of imager radiances over clear area | 74 | W $m^{-2}$ $sr^{-1}$ $\mu m^{-1}$ | TBD | | 532I |
| | 75 Total aerosol visible optical depth in clear area | 75 | N/A | 0 .. 2 | | 132A |
| | 76 Total aerosol effective radius in clear area | 76 | $\mu m$ | 0 .. 20 | | 132A |
| **Cloudy Footprint Area** | | | | | | |
| **Cloud Category Arrays** is Array[2] of: | | | | | | |
| | 77 Cloud category area percent coverage | 77 | N/A | 0 .. 100 | | 216A |
| | 78 Cloud category overcast percent coverage | 78 | N/A | 0 .. 100 | | 216A |
| | 79 Cloud category broken percent coverage | 79 | N/A | 0 .. 100 | | 216A |
| | 80 Mean of imager radiances for cloud category | 80 | W $m^{-2}$ $sr^{-1}$ $\mu m^{-1}$ | TBD | | 2 x 532A |
| | 81 Stddev of imager radiances for cloud category | 81 | W $m^{-2}$ $sr^{-1}$ $\mu m^{-1}$ | TBD | | 2 x 532I |
| | 82 Mean cloud visible optical depth for cloud category | 82 | N/A | 0 .. 400 | | 232A |
| | 83 Stddev of visible optical depth for cloud category | 83 | N/A | TBD | | 232A |
| | 84 Mean logarithm of cloud visible optical depth for cloud category | 84 | N/A | 0 .. 6 | | 232A |
| | 85 Stddev of logarithm of visible optical depth for cloud category | 85 | N/A | TBD | | 232A |
| | 86 Mean cloud infrared emissivity for cloud category | 86 | N/A | 0 .. 1 | | 232A |

| | | | | |
|---|---|---|---|---|
| 87 Stddev of cloud infrared emissivity for cloud category | 87 | N/A | TBD | 232A |
| 88 Mean liquid water path for cloud category | 88 | g $m^{-2}$ | TBD | 232A |
| 89 Stddev of liquid water path for cloud category | 89 | g $m^{-2}$ | TBD | 232V |
| 90 Mean ice water path for cloud category | 90 | g $m^{-2}$ | TBD | 232A |
| 91 Stdev of ice water path for cloud category | 91 | g $m^{-2}$ | TBD | 232V |
| 92 Mean cloud top pressure for cloud category | 92 | hPa | 0 .. 1100 | 232A |
| 93 Stddev of cloud top pressure for cloud category | 93 | hPa | TBD | 232V |
| 94 Mean cloud effective pressure for cloud category | 94 | hPa | 0 .. 1100 | 232A |
| 95 Stddev of cloud effective pressure for cloud category | 95 | hPa | TBD | 232A |
| 96 Mean cloud effective temperature for cloud category | 96 | K | 100 .. 350 | 232A |
| 97 Stddev of cloud effective temperature for cloud category | 97 | K | TBD | 232A |
| 98 Mean cloud effective height for cloud category | 98 | km | 0 .. 20 | 232A |
| 99 Stddev of cloud effective height for cloud category | 99 | km | TBD | 232V |
| 100 Mean cloud bottom pressure for cloud category | 100 | hPa | 0 .. 1100 | 232A |
| 101 Stddev of cloud bottom pressure for cloud category | 101 | hPa | TBD | 232V |
| 102 Mean water particle radius for cloud category | 102 | µm | TBD | 232A |
| 103 Stddev of water particle radius for cloud category | 103 | µm | TBD | 232A |
| 104 Mean ice particle effective diameter for cloud category | 104 | µm | TBD | 232A |
| 105 Stddev of ice particle effective diameter for cloud category | 105 | µm | TBD | 232A |
| 106 Mean cloud particle phase for cloud category | 106 | N/A | 0 .. 1 | 232A |
| 107 Stddev of cloud particle phase for cloud category | 107 | N/A | 0 .. 1 | 232V |
| 108 Mean vertical aspect ratio for cloud category (TBD) | 108 | N/A | 0 .. 1 | 232A |

Table A-3 Single Satellite Footprint (SSF) (3 of 3)

| **Description Product** | **Parameter Number** | **Units** | **Range** | **Elements/Bits/Record** | **Code** |
|---|---|---|---|---|---|
| 109 Stddev of vertical aspect ratio for cloud category (TBD) | 109 | N/A | TBD | | 232V |
| 110 Percentiles of visible optical depth for cloud category | 110 | N/A | TBD | 2 | x 1332I |
| 111 Percentiles of IR emissivity for cloud category | 111 | N/A | TBD | 2 | x 1332I |
| **Overlap Footprint Area** | | | | | |
| 112 Number of imager pixels for overlap condition | 112 | N/A | 0 .. 9000 | | 416A |
| 113 Overlap condition weighted area percentage | 113 | N/A | 0 .. 100 | | 416A |

| | |
|---|---|
| Total Meta Bits/File: | 1704 |
| Total Data Bits/Record: | 7744 |
| Total Records/File: | 245475 |
| Total Data Bits/File: | 1900958400 |
| Total MegaBytes / Hour | 237.6 |
| Total GigaBytes / Day | 5.7 |

# Appendix B - Output Data Products

## Compute Surface and Atmospheric Fluxes (Subsystem 5)

This appendix describes the data products which are produced by the algorithms in this subsystem. The table below summarizes these products, listing the CERES and EOSDIS product codes or abbreviations, a short product name, the product type, the production frequency, and volume estimates for each individual product as well as a complete data month of production. The product types are defined as follows:

| | |
|---|---|
| Archival products: | Assumed to be permanently stored by EOSDIS |
| Internal products: | Temporary storage by EOSDIS (days to years) |

The following pages describe each product. An introductory page provides an overall description of the product and specifies the temporal and spatial coverage. The table which follows the introductory page briefly describes every parameter which is contained in the product. Each product may be thought of as metadata followed by data records. The metadata (or header data) is not well-defined yet and is included mainly as a placeholder. The description of parameters which are present in each data record includes parameter number (a unique number for each distinct parameter), units, dynamic range, the number of elements per record, an estimate of the number of bits required to represent each parameter, and an element number (a unique number for each instance of every parameter). A summary at the bottom of each table shows the current estimated sizes for metadata, each data record, and the total data product. A more detailed description of each data product will be contained in a User's Guide to be published before the first CERES launch.

Table B-1. Output Products Summary

| Product Code | | Name | Type | Frequency | Size, MB | Monthly Size, MB |
|---|---|---|---|---|---|---|
| CERES | EOSDIS | | | | | |
| CRS | CER04 | Clouds and Radiative Swath | Archival | 1/Hour | 285.61 | 212491 |

## Clouds and Radiative Swath (CRS)

The CERES archival product Clouds and Radiative Swath (CRS) is produced by the CERES Instantaneous Surface and Atmospheric Radiation Budget (SARB) Subsystem. Each CRS file contains longwave and shortwave radiative fluxes for the surface, internal atmosphere and TOA for each CERES field-of-view (FOV). The CRS contains data for an one-hour satellite swath (8-12 percent of the Earth) from one satellite. In addition to being an archival product, the CRS is used by the CERES subsystem Grid Single Satellite Radiative Fluxes and Clouds.

For each CERES FOV, the CRS contains:

- CERES FOV geometry, time, and scene data
- CERES FOV satellite altitude radiance data
- CERES FOV estimated TOA flux data
- CERES FOV surface flux data
- CERES FOV total-sky area data
- CERES FOV clear-sky area data
- Cloud category properties for two of four cloud height categories (low (L), lower middle (LM), upper middle (UM), and high (H)) over the CERES FOV
- Overlap data for four of eleven cloud overlap conditions (clear, L, LM, UM, H, H/UM, H/LM, H/L, UM/LM, UM/L, LM/L) over the CERES FOV
- CERES FOV surface radiative parameters
- Atmospheric flux profiles for both clear-sky and total-sky at the surface, 500hPa, the tropopause, and the TOA over the CERES FOV
- Flux adjustments (tuned-untuned) for clear-sky and total-sky at the surface and TOA over the CERES FOV
- Adjustment parameters for clear-sky (note that these are calculated for both clear-sky and total-sky FOV)
- Adjustment parameters for the two cloud categories over the CERES FOV
- Auxilliary adjustment quality control flags

**Level:** 2
**Type:** Archival
**Frequency:** 1/ Hour

**Time Interval Covered**
**File:** 1 hour
**Record:** Instantaneous

**Portion of Globe Covered**
**File:** Satellite Swath
**Record:** 1 CERES FOV

**Portion of Atmosphere Covered**
**File:** Surface to TOA

Table B-2 Clouds and Radiative Swath (CRS) (1 of 3)

| Description Product | Parameter Number | Units | Range | Elements/ Record | Bits/ Elem Code |
|---|---|---|---|---|---|
| **CRS Header** | | | | | |
| Day and time at hour start | | N/A | ASCII string | 1 | 216A |
| Character name of satellite | | N/A | ASCII string | 1 | 64A |
| Character name of CERES instrument | | N/A | ASCII string | 1 | 32A |
| Character name of high resolution imager instrument | | N/A | ASCII string | 1 | 64A |
| Number of imager channels used | | N/A | 1 .. 20 | 1 | 16A |
| Central wavelengths of imager channels | | μm | 0.4 .. 15.0 | 20 | 32A |
| Earth-Sun distance | | AU | .98 .. 1.02 | 1 | 32A |
| Day and time IES processed (SS 1.0) | | N/A | ASCII string | 1 | 152V |
| Day and time Imager Cloud Properties processed (SS 4.1- 4.3) | | N/A | ASCII string | 1 | 152V |
| Day and time Convolution of Imager with CERES processed (SS 4.4) | | N/A | ASCII string | 1 | 152V |
| Day and time TOA and Surface Estimation processed (SS 4.5 - 4.6) | | N/A | ASCII string | 1 | 152A |
| Number of footprints in CRS product | | N/A | 0 .. 245275 | 1 | 32A |
| **CERES FOV Geometry, Time, and Scene** | | | | | |
| Time of observation | 1 | day | -0.01 .. 1.01 | 1 | 64A |
| Radius of satellite from center of Earth at observation | 2 | km | 6000 .. 8000 | 1 | 64A |
| Colatitude of satellite at observation | 3 | deg | 0 .. 180 | 1 | 32A |
| Longitude of satellite at observation | 4 | deg | 0 .. 360 | 1 | 32A |
| Colatitude of Sun at observation | 5 | deg | 0 .. 180 | 1 | 32A |
| Longitude of Sun at observation | 6 | deg | 0 .. 360 | 1 | 32A |
| Colatitude of CERES FOV at TOA | 7 | deg | 0 .. 180 | 1 | 32A |
| Longitude of CERES FOV at TOA | 8 | deg | 0 .. 360 | 1 | 32A |
| Colatitude of CERES FOV at surface | 9 | deg | 0 .. 180 | 1 | 32A |
| Longitude of CERES FOV at surface | 10 | deg | 0 .. 360 | 1 | 32A |
| Scan sample number | 11 | N/A | 1 .. 660 | 1 | 16A |
| Packet number | 12 | N/A | 0 .. 32767 | 1 | 16A |
| Cone angle of CERES FOV at satellite | 13 | deg | 0 .. 90 | 1 | 32A |
| Clock angle of CERES FOV at satellite wrt inertial velocity | 14 | deg | 0 .. 360 | 1 | 32A |
| Rate of change of cone angle | 15 | deg $sec^{-1}$ | -100 .. 100 | 1 | 32A |
| Rate of change of clock angle | 16 | deg $sec^{-1}$ | -10 .. 10 | 1 | 32A |
| Along-track angle of CERES FOV at TOA | 17 | deg | 0 .. 360 | 1 | 32A |
| Cross-track angle of CERES FOV at TOA | 18 | deg | -90 .. 90 | 1 | 32A |
| X component of satellite inertial velocity vector | 19 | km $sec^{-1}$ | -10 .. 10 | 1 | 64A |
| Y component of satellite inertial velocity vector | 20 | km $sec^{-1}$ | -10 .. 10 | 1 | 64A |
| Z component of satellite inertial velocity vector | 21 | km $sec^{-1}$ | -10 .. 10 | 1 | 64A |
| CERES viewing zenith angle at TOA | 22 | deg | 0 .. 90 | 1 | 32A |
| CERES solar zenith angle at TOA | 23 | deg | 0 .. 180 | 1 | 32A |
| CERES relative azimuth angle at TOA | 24 | deg | 0 .. 360 | 1 | 32A |
| CERES viewing azimuth angle at TOA wrt North | 25 | deg | 0 .. 360 | 1 | 32V |
| Surface altitude above sea level | 26 | m | -1000 .. 10000 | 1 | 32A |
| Surface type index | 27 | N/A | 1 .. 20 | 8 | 16A |
| Surface type percent coverage | 28 | N/A | 0 .. 100 | 8 | 16A |
| CERES SW ADM type for inversion process | 29 | N/A | 0 .. 200 | 1 | 16A |
| CERES LW ADM type for inversion process | 30 | N/A | 0 .. 600 | 1 | 16A |
| CERES WN ADM type for inversion process | 31 | N/A | 0 .. 600 | 1 | 16A |
| **CERES FOV Satellite Altitude Radiance Data** | | | | | |
| CERES TOT filtered radiance, satellite altitude, upwards | 32 | W $m^{-2}sr^{-1}$ | 0 .. 700 | 1 | 32I |
| CERES SW filtered radiance, satellite altitude, upwards | 33 | W $m^{-2}sr^{-1}$ | -10 .. 510 | 1 | 32I |
| CERES WN filtered radiance, satellite altitude, upwards | 34 | W $m^{-2}sr^{-1}$ | 0 .. 50 | 1 | 32I |
| IES quality flags | 35 | N/A | see table TBD | 1 | 32A |
| CERES SW unfiltered radiance, satellite altitude, upwards | 36 | W $m^{-2}sr^{-1}$ | -10 .. 510 | 1 | 32A |
| CERES LW unfiltered radiance, satellite altitude, upwards | 37 | W $m^{-2}sr^{-1}$ | 0 .. 200 | 1 | 32A |
| CERES WN unfiltered radiance, satellite altitude, upwards | 38 | W $m^{-2}sr^{-1}$ | 0 .. 50 | 1 | 32A |
| **CERES FOV Estimated TOA Flux Data** | | | | | |
| CERES SW flux, TOA, upwards | 39 | W $m^{-2}$ | 0 .. 1400 | 1 | 32A |
| CERES LW flux, TOA, upwards | 40 | W $m^{-2}$ | 0 .. 500 | 1 | 32A |
| CERES WN flux, TOA, upwards | 41 | W $m^{-2}$ | 0 .. 1400 | 1 | 32A |

Table B-2 Clouds and Radiative Swath (CRS) (2 of 3)

| Description Product | Parameter Number | Units | Range | Elements/ Record | Bits/ Elem Code |
|---|---|---|---|---|---|
| **CERES FOV Surface Flux Data** | | | | | |
| CERES SW flux, surface, downwards, Model A | 42 | W $m^{-2}$ | 0 .. 1400 | 1 | 32A |
| CERES LW flux, surface, downwards, Model A | 43 | W $m^{-2}$ | 0 .. 700 | 1 | 32A |
| CERES WN flux, surface, downwards, Model A | 44 | W $m^{-2}$ | 0 .. 700 | 1 | 32A |
| CERES nonWN flux, surface, downwards, Model A | 45 | W $m^{-2}$ | 0 .. 700 | 1 | 32A |
| CERES SW flux, surface, net, Model A | 46 | W $m^{-2}$ | 0 .. 1400 | 1 | 32A |
| CERES LW flux, surface, net, Model A | 47 | W $m^{-2}$ | -250 .. 50 | 1 | 32A |
| CERES SW flux, surface, downwards, Model B (TBD) | 48 | W $m^{-2}$ | 0 .. 1400 | 1 | 32A |
| CERES LW flux, surface, downwards, Model B | 49 | W $m^{-2}$ | 0 .. 700 | 1 | 32A |
| CERES SW flux, surface, net, Model B (TBD) | 50 | W $m^{-2}$ | 0 .. 1400 | 1 | 32A |
| CERES LW flux, surface, net, Model B | 51 | W $m^{-2}$ | -250 .. 50 | 1 | 32A |
| CERES spectral reflectivity | 52 | N/A | 0 .. 1 | 6 | 32I |
| CERES broadband surface albedo (uncorrected) | 53 | N/A | 0 .. 1 | 1 | 32I |
| CERES LW surface emissivity | 54 | N/A | 0 .. 1 | 1 | 32I |
| CERES WN surface emissivity | 55 | N/A | 0 .. 1 | 1 | 32I |
| Imager-based surface skin temperature | 56 | K | 175 .. 375 | 1 | 32I |
| **CERES FOV Total-Sky Area Data** | | | | | |
| Number of imager pixels in CERES FOV | 57 | N/A | 0 .. 9000 | 1 | 16A |
| Imager percent coverage | 58 | N/A | 0 .. 100 | 1 | 16A |
| Precipitable water | 59 | cm | 0.001 .. 10.000 | 1 | 32A |
| Shadowed pixels percent coverage (TBD) | 60 | N/A | 0 .. 100 | 1 | 16A |
| Notes on general procedures | 61 | N/A | TBD | 1 | 16A |
| Notes on cloud algorithms | 62 | N/A | TBD | 1 | 16A |
| Imager viewing zenith angle over CERES FOV, mean | 63 | deg | 0 .. 90 | 1 | 32A |
| Imager relative azimuth angle over CERES FOV, mean | 64 | deg | 0 .. 360 | 1 | 32A |
| Imager channel identifier (5 channels) | 65 | N/A | 1 .. 20 | 5 | 16A |
| Imager radiance over CERES FOV, 5th percentile | 66 | W $m^{-2}sr^{-1}\mu m^{-1}$ | TBD | 5 | 32V |
| Imager radiance over CERES FOV, mean | 67 | W $m^{-2}sr^{-1}\mu m^{-1}$ | TBD | 5 | 32A |
| Imager radiance over CERES FOV, 95th percentile | 68 | W $m^{-2}sr^{-1}\mu m^{-1}$ | TBD | 5 | 32V |
| **CERES FOV Clear-Sky Area Data** | | | | | |
| Sunglint percent coverage | 69 | N/A | 0 .. 100 | 1 | 16A |
| Snow/Ice percent coverage | 70 | N/A | 0 .. 100 | 1 | 16A |
| Smoke percent coverage | 71 | N/A | 0 .. 100 | 1 | 16A |
| Fire percent coverage | 72 | N/A | 0 .. 100 | 1 | 16A |
| Imager radiance, clear-sky area, mean | 73 | W $m^{-2}sr^{-1}\mu m^{-1}$ | TBD | 5 | 32A |
| Imager radiance, clear-sky area, std | 74 | W $m^{-2}sr^{-1}\mu m^{-1}$ | TBD | 5 | 32I |
| Total aerosol visible optical depth, clear-sky area | 75 | N/A | 0 .. 2 | 1 | 32A |
| Total aerosol effective radius, clear-sky area | 76 | μm | 0 .. 20 | 1 | 32A |
| **Cloud Properties for Two of Four Cloud Height Categories (Height categories are Low (L), Lower Middle (LM), Upper Middle (UM), and High (H))** | | | | | |
| Area percent coverage | 77 | N/A | 0 .. 100 | 2 | 16A |
| Overcast percent coverage | 78 | N/A | 0 .. 100 | 2 | 16A |
| Broken percent coverage | 79 | N/A | 0 .. 100 | 2 | 16A |
| Imager radiance, mean | 80 | W $m^{-2}sr^{-1}\mu m^{-1}$ | TBD | 10 | 32A |
| Imager radiance, std | 81 | W $m^{-2}sr^{-1}\mu m^{-1}$ | TBD | 10 | 32I |
| Cloud visible optical depth, linear, mean | 82 | N/A | 0 .. 400 | 2 | 32A |
| Cloud visible optical depth, linear, std | 83 | N/A | TBD | 2 | 32A |
| Cloud visible optical depth, logarithmic, mean | 84 | N/A | 0 .. 6 | 2 | 32A |
| Cloud visible optical depth, logarithmic, std | 85 | N/A | TBD | 2 | 32A |
| Cloud infrared emissivity, mean | 86 | N/A | 0 .. 1 | 2 | 32A |
| Cloud infrared emissivity, std | 87 | N/A | TBD | 2 | 32A |
| Liquid water path, mean | 88 | g $m^{-2}$ | TBD | 2 | 32A |
| Liquid water path, std | 89 | g $m^{-2}$ | TBD | 2 | 32V |
| Ice water path, mean | 90 | g $m^{-2}$ | TBD | 2 | 32A |
| Ice water path, std | 91 | g $m^{-2}$ | TBD | 2 | 32V |
| Cloud top pressure, mean | 92 | hPa | 0 .. 1100 | 2 | 32A |
| Cloud top pressure, std | 93 | hPa | TBD | 2 | 32V |
| Cloud effective pressure, mean | 94 | hPa | 0 .. 1100 | 2 | 32A |
| Cloud effective pressure, std | 95 | hPa | TBD | 2 | 32A |
| Cloud effective temperature, mean | 96 | K | 100 .. 350 | 2 | 32A |
| Cloud effective temperature, std | 97 | K | TBD | 2 | 32A |

Table B-2 Clouds and Radiative Swath (CRS) (3 of 3)

| Description | Parameter Number | Units | Range | Elements/Bits/ Record | Product ElemCode |
|---|---|---|---|---|---|
| **Cloud Properties (Continued)** | | | | | |
| Cloud effective height, mean | 98 | km | 0 .. 20 | 2 | 32A |
| Cloud effective height, std | 99 | km | TBD | 2 | 32V |
| Cloud bottom pressure, mean | 100 | hPa | 0 .. 1100 | 2 | 32A |
| Cloud bottom pressure, std | 101 | hPa | TBD | 2 | 32V |
| Water particle radius, mean | 102 | µm | TBD | 2 | 32A |
| Water particle radius, std | 103 | µm | TBD | 2 | 32A |
| Ice particle effective diameter, mean | 104 | µm | TBD | 2 | 32A |
| Ice particle effective diameter, std | 105 | µm | TBD | 2 | 32A |
| Cloud particle phase, mean | 106 | N/A | 0 .. 1 | 2 | 32A |
| Cloud particle phase, std | 107 | N/A | 0 .. 1 | 2 | 32V |
| Vertical aspect ratio, mean (TBD) | 108 | N/A | 0 .. 1 | 2 | 32A |
| Vertical aspect ratio, std (TBD) | 109 | N/A | TBD | 2 | 32V |
| Visible optical depth, 13 percentiles | 110 | N/A | TBD | 26 | 32I |
| IR emissivity, 13 percentiles | 111 | N/A | TBD | 26 | 32I |
| **CERES FOV Overlap Data for Four Overlap Conditions** | | | | | |
| Number imager pixels for overlap condition | 112 | N/A | 0 .. 9000 | 4 | 16A |
| Overlap condition weighted area percentage | 113 | N/A | 0 .. 100 | 4 | 16A |
| **Surface Radiative Parameters** | | | | | |
| Photosynthetically active radiation, surface (TBD) | 114 | W $m^{-2}$ | 0 .. 780 | 1 | 32A |
| Direct/diffuse ratio, surface (TBD) | 115 | N/A | 0 .. 30 | 1 | 32A |
| Corrected initial broadband surface albedo | 116 | N/A | 0 .. 1 | 1 | 32A |
| **Atmospheric Flux Profile for Clear-sky and Total-sky (Atmospheric levels in profile are surface, 500 hPa, tropopause and TOA)** | | | | | |
| Number atmospheric levels | 117 | N/A | 0 .. 4 | 1 | 16A |
| Level pressures | 118 | hPa | 0 .. 1100 | 4 | 32A |
| SW flux, atmospheric level, upwards, tuned | 119 | W $m^{-2}$ | 0 .. 1400 | 8 | 32A |
| SW flux, atmospheric level, downwards, tuned | 120 | W $m^{-2}$ | 0 .. 1400 | 8 | 32A |
| LW flux, atmospheric level, upwards, tuned | 121 | W $m^{-2}$ | 0 .. 500 | 8 | 32A |
| LW flux, atmospheric level, downwards, tuned | 122 | W $m^{-2}$ | 0 .. 500 | 8 | 32A |
| **Flux Adjustments (Tuned - Untuned) for Clear-sky and Total-sky** | | | | | |
| SW flux, surface, downwards, delta | 123 | W $m^{-2}$ | -1400 .. 1400 | 2 | 32A |
| SW flux, surface, upwards, delta | 124 | W $m^{-2}$ | -1400 .. 1400 | 2 | 32A |
| SW flux, TOA, upwards, delta | 125 | W $m^{-2}$ | -1400 .. 1400 | 2 | 32A |
| LW flux, surface, downwards, delta | 126 | W $m^{-2}$ | -500 .. 500 | 2 | 32A |
| LW flux, surface, upwards, delta | 127 | W $m^{-2}$ | -500 .. 500 | 2 | 32A |
| LW flux, TOA, upwards, delta | 128 | W $m^{-2}$ | -500 .. 500 | 2 | 32A |
| **Adjustment Parameters for Clear Skies** | | | | | |
| Adjusted precipitable water, delta | 129 | cm | -10 .. 10 | 1 | 32A |
| Adjusted surface albedo, delta | 130 | N/A | -1 .. 1 | 1 | 32A |
| Adjusted aerosol optical depth, delta | 131 | N/A | -2 .. 2 | 1 | 32A |
| Adjusted skin temperature, delta | 132 | K | TBD | 1 | 32A |
| **Adjustment Parameters for Two Cloud Height Categories** | | | | | |
| Adjusted mean visible optical depth, delta | 133 | N/A | -400 .. 400 | 2 | 32A |
| Adjusted mean cloud fractional area, delta | 134 | N/A | -1 .. 1 | 2 | 32A |
| Adjusted mean cloud effective temperature, delta | 135 | K | TBD | 2 | 32A |
| **Auxillary Adustment Quality Control Flags** | | | | | |
| Constrainment status flag | 136 | N/A | TBD | 1 | 32A |
| Sigma table configuration flag | 137 | N/A | TBD | 1 | 32A |

| | |
|---|---|
| Total Meta Bits/File: | 1704 |
| Total Data Bits/Record: | 9760 |
| Total Records/File: | 245475 |
| Total Data Bits/File: | 2395836000 |
| Total Bits/FIle: | 2395837704 |

# Appendix C

## Nomenclature

### Acronyms

| | |
|---|---|
| ADEOS | Advanced Earth Observing System |
| ADM | Angular Distribution Model |
| AIRS | Atmospheric Infrared Sounder (EOS-AM) |
| AMSU | Advanced Microwave Sounding Unit (EOS-PM) |
| APD | Aerosol Profile Data |
| APID | Application Identifier |
| ARESE | ARM Enhanced Shortwave Experiment |
| ARM | Atmospheric Radiation Measurement |
| ASOS | Automated Surface Observing Sites |
| ASTER | Advanced Spaceborne Thermal Emission and Reflection Radiometer |
| ASTEX | Atlantic Stratocumulus Transition Experiment |
| ASTR | Atmospheric Structures |
| ATBD | Algorithm Theoretical Basis Document |
| AVG | Monthly Regional, Average Radiative Fluxes and Clouds (CERES Archival Data Product) |
| AVHRR | Advanced Very High Resolution Radiometer |
| BDS | Bidirectional Scan (CERES Archival Data Product) |
| BRIE | Best Regional Integral Estimate |
| BSRN | Baseline Surface Radiation Network |
| BTD | Brightness Temperature Difference(s) |
| CCD | Charge Coupled Device |
| CCSDS | Consultative Committee for Space Data Systems |
| CEPEX | Central Equatorial Pacific Experiment |
| CERES | Clouds and the Earth’s Radiant Energy System |
| CID | Cloud Imager Data |
| CLAVR | Clouds from AVHRR |
| CLS | Constrained Least Squares |
| COPRS | Cloud Optical Property Retrieval System |
| CPR | Cloud Profiling Radar |
| CRH | Clear Reflectance, Temperature History (CERES Archival Data Product) |
| CRS | Single Satellite CERES Footprint, Radiative Fluxes and Clouds (CERES Archival Data Product) |
| DAAC | Distributed Active Archive Center |
| DAC | Digital-Analog Converter |

| | |
|---|---|
| DAO | Data Assimilation Office |
| DB | Database |
| DFD | Data Flow Diagram |
| DLF | Downward Longwave Flux |
| DMSP | Defense Meteorological Satellite Program |
| EADM | ERBE-Like Albedo Directional Model (CERES Input Data Product) |
| ECA | Earth Central Angle |
| ECLIPS | Experimental Cloud Lidar Pilot Study |
| ECMWF | European Centre for Medium-Range Weather Forecasts |
| EDDB | ERBE-Like Daily Data Base (CERES Archival Data Product) |
| EID9 | ERBE-Like Internal Data Product 9 (CERES Internal Data Product) |
| EOS | Earth Observing System |
| EOSDIS | Earth Observing System Data Information System |
| EOS-AM | EOS Morning Crossing Mission |
| EOS-PM | EOS Afternoon Crossing Mission |
| ENSO | El Niño/Southern Oscillation |
| ENVISAT | Environmental Satellite |
| EPHANC | Ephemeris and Ancillary (CERES Input Data Product) |
| ERB | Earth Radiation Budget |
| ERBE | Earth Radiation Budget Experiment |
| ERBS | Earth Radiation Budget Satellite |
| ESA | European Space Agency |
| ES4 | ERBE-Like S4 Data Product (CERES Archival Data Product) |
| ES4G | ERBE-Like S4G Data Product (CERES Archival Data Product) |
| ES8 | ERBE-Like S8 Data Product (CERES Archival Data Product) |
| ES9 | ERBE-Like S9 Data Product (CERES Archival Data Product) |
| FLOP | Floating Point Operation |
| FIRE | First ISCCP Regional Experiment |
| FIRE II IFO | First ISCCP Regional Experiment II Intensive Field Observations |
| FOV | Field of View |
| FSW | Hourly Gridded Single Satellite Fluxes and Clouds (CERES Archival Data Product) |
| FTM | Functional Test Model |
| GAC | Global Area Coverage (AVHRR data mode) |
| GAP | Gridded Atmospheric Product (CERES Input Data Product) |
| GCIP | GEWEX Continental-Phase International Project |
| GCM | General Circulation Model |
| GEBA | Global Energy Balance Archive |

| | |
|---|---|
| GEO | ISSCP Radiances (CERES Input Data Product) |
| GEWEX | Global Energy and Water Cycle Experiment |
| GLAS | Geoscience Laser Altimetry System |
| GMS | Geostationary Meteorological Satellite |
| GOES | Geostationary Operational Environmental Satellite |
| HBTM | Hybrid Bispectral Threshold Method |
| HIRS | High-Resolution Infrared Radiation Sounder |
| HIS | High-Resolution Interferometer Sounder |
| ICM | Internal Calibration Module |
| ICRCCM | Intercomparison of Radiation Codes in Climate Models |
| ID | Identification |
| IEEE | Institute of Electrical and Electronics Engineers |
| IES | Instrument Earth Scans (CERES Internal Data Product) |
| IFO | Intensive Field Observation |
| INSAT | Indian Satellite |
| IOP | Intensive Observing Period |
| IR | Infrared |
| IRIS | Infrared Interferometer Spectrometer |
| ISCCP | International Satellite Cloud Climatology Project |
| ISS | Integrated Sounding System |
| IWP | Ice Water Path |
| LAC | Local Area Coverage (AVHRR data mode) |
| LaRC | Langley Research Center |
| LBC | Laser Beam Ceilometer |
| LBTM | Layer Bispectral Threshold Method |
| Lidar | Light Detection and Ranging |
| LITE | Lidar In-Space Technology Experiment |
| Lowtran 7 | Low-Resolution Transmittance (Radiative Transfer Code) |
| LW | Longwave |
| LWP | Liquid Water Path |
| MAM | Mirror Attenuator Mosaic |
| MC | Mostly Cloudy |
| MCR | Microwave Cloud Radiometer |
| METEOSAT | Meteorological Operational Satellite (European) |
| METSAT | Meteorological Satellite |
| MFLOP | Million FLOP |
| MIMR | Multifrequency Imaging Microwave Radiometer |
| MISR | Multiangle Imaging Spectroradiometer |

| | |
|---|---|
| MLE | Maximum Likelihood Estimate |
| MOA | Meteorology Ozone and Aerosol |
| MODIS | Moderate-Resolution Imaging Spectroradiometer |
| MSMR | Multispectral, multiresolution |
| MTSA | Monthly Time and Space Averaging |
| MWH | Microwave Humidity |
| MWP | Microwave Water Path |
| NASA | National Aeronautics and Space Administration |
| NCAR | National Center for Atmospheric Research |
| NCEP | National Centers for Environmental Prediction |
| NESDIS | National Environmental Satellite, Data, and Information Service |
| NIR | Near Infrared |
| NMC | National Meteorological Center |
| NOAA | National Oceanic and Atmospheric Administration |
| NWP | Numerical Weather Prediction |
| OLR | Outgoing Longwave Radiation |
| OPD | Ozone Profile Data (CERES Input Data Product) |
| OV | Overcast |
| PC | Partly Cloudy |
| POLDER | Polarization of Directionality of Earth’s Reflectances |
| PRT | Platinum Resistance Thermometer |
| PSF | Point Spread Function |
| PW | Precipitable Water |
| RAPS | Rotating Azimuth Plane Scan |
| RPM | Radiance Pairs Method |
| RTM | Radiometer Test Model |
| SAB | Sorting by Angular Bins |
| SAGE | Stratospheric Aerosol and Gas Experiment |
| SARB | Surface and Atmospheric Radiation Budget Working Group |
| SDCD | Solar Distance Correction and Declination |
| SFC | Hourly Gridded Single Satellite TOA and Surface Fluxes (CERES Archival Data Product) |
| SHEBA | Surface Heat Budget in the Arctic |
| SPECTRE | Spectral Radiance Experiment |
| SRB | Surface Radiation Budget |
| SRBAVG | Surface Radiation Budget Average (CERES Archival Data Product) |
| SSF | Single Satellite CERES Footprint TOA and Surface Fluxes, Clouds |
| SSMI | Special Sensor Microwave Imager |

| | |
|---|---|
| SST | Sea Surface Temperature |
| SURFMAP | Surface Properties and Maps (CERES Input Product) |
| SW | Shortwave |
| SWICS | Shortwave Internal Calibration Source |
| SYN | Synoptic Radiative Fluxes and Clouds (CERES Archival Data Product) |
| SZA | Solar Zenith Angle |
| THIR | Temperature/Humidity Infrared Radiometer (Nimbus) |
| TIROS | Television Infrared Observation Satellite |
| TISA | Time Interpolation and Spatial Averaging Working Group |
| TMI | TRMM Microwave Imager |
| TOA | Top of the Atmosphere |
| TOGA | Tropical Ocean Global Atmosphere |
| TOMS | Total Ozone Mapping Spectrometer |
| TOVS | TIROS Operational Vertical Sounder |
| TRMM | Tropical Rainfall Measuring Mission |
| TSA | Time-Space Averaging |
| UAV | Unmanned Aerospace Vehicle |
| UT | Universal Time |
| UTC | Universal Time Code |
| VAS | VISSR Atmospheric Sounder (GOES) |
| VIRS | Visible Infrared Scanner |
| VISSR | Visible and Infrared Spin Scan Radiometer |
| WCRP | World Climate Research Program |
| WG | Working Group |
| Win | Window |
| WN | Window |
| WMO | World Meteorological Organization |
| ZAVG | Monthly Zonal and Global Average Radiative Fluxes and Clouds (CERES Archival Data Product) |

**Symbols**

| | |
|---|---|
| $A$ | atmospheric absorptance |
| $B_\lambda(T)$ | Planck function |
| $C$ | cloud fractional area coverage |
| $CF_2Cl_2$ | dichlorofluorocarbon |
| $CFCl_3$ | trichlorofluorocarbon |
| $CH_4$ | methane |
| $CO_2$ | carbon dioxide |
| $D$ | total number of days in the month |

| | |
|---|---|
| $D_e$ | cloud particle equivalent diameter (for ice clouds) |
| $E_o$ | solar constant or solar irradiance |
| $F$ | flux |
| $f$ | fraction |
| $G_a$ | atmospheric greenhouse effect |
| $g$ | cloud asymmetry parameter |
| $H_2O$ | water vapor |
| $I$ | radiance |
| $i$ | scene type |
| $m_i$ | imaginary refractive index |
| $\hat{N}$ | angular momentum vector |
| $N_2O$ | nitrous oxide |
| $O_3$ | ozone |
| $P$ | point spread function |
| $p$ | pressure |
| $Q_a$ | absorption efficiency |
| $Q_e$ | extinction efficiency |
| $Q_s$ | scattering efficiency |
| $R$ | anisotropic reflectance factor |
| $r_E$ | radius of the Earth |
| $r_e$ | effective cloud droplet radius (for water clouds) |
| $r_h$ | column-averaged relative humidity |
| $S_o$ | summed solar incident SW flux |
| $S_o'$ | integrated solar incident SW flux |
| $T$ | temperature |
| $T_B$ | blackbody temperature |
| $t$ | time or transmittance |
| $W_{liq}$ | liquid water path |
| $w$ | precipitable water |
| $\hat{x}_o$ | satellite position at $t_o$ |
| $x, y, z$ | satellite position vector components |
| $\dot{x}, \dot{y}, \dot{z}$ | satellite velocity vector components |
| $z$ | altitude |
| $z_{top}$ | altitude at top of atmosphere |
| $\alpha$ | albedo or cone angle |
| $\beta$ | cross-scan angle |
| $\gamma$ | Earth central angle |
| $\gamma_{at}$ | along-track angle |

| | |
|---|---|
| $\gamma_{ct}$ | cross-track angle |
| $\delta$ | along-scan angle |
| $\varepsilon$ | emittance |
| $\Theta$ | colatitude of satellite |
| $\theta$ | viewing zenith angle |
| $\theta_o$ | solar zenith angle |
| $\lambda$ | wavelength |
| $\mu$ | viewing zenith angle cosine |
| $\mu_o$ | solar zenith angle cosine |
| $\nu$ | wave number |
| $\rho$ | bidirectional reflectance |
| $\tau$ | optical depth |
| $\tau_{aer}(p)$ | spectral optical depth profiles of aerosols |
| $\tau_{H_2O\lambda}(p)$ | spectral optical depth profiles of water vapor |
| $\tau_{O_3}(p)$ | spectral optical depth profiles of ozone |
| $\Phi$ | longitude of satellite |
| $\phi$ | azimuth angle |
| $\omega_o$ | single-scattering albedo |

Subscripts:

| | |
|---|---|
| *c* | cloud |
| *cb* | cloud base |
| *ce* | cloud effective |
| *cld* | cloud |
| *cs* | clear sky |
| *ct* | cloud top |
| *ice* | ice water |
| *lc* | lower cloud |
| *liq* | liquid water |
| *s* | surface |
| *uc* | upper cloud |
| $\lambda$ | spectral wavelength |

**Units**

| | |
|---|---|
| AU | astronomical unit |
| cm | centimeter |
| cm-sec$^{-1}$ | centimeter per second |
| count | count |
| day | day, Julian date |

| | |
|---|---|
| deg | degree |
| deg-sec$^{-1}$ | degree per second |
| DU | Dobson unit |
| erg-sec$^{-1}$ | erg per second |
| fraction | fraction (range of 0–1) |
| g | gram |
| g-cm$^{-2}$ | gram per square centimeter |
| g-g$^{-1}$ | gram per gram |
| g-m$^{-2}$ | gram per square meter |
| h | hour |
| hPa | hectopascal |
| K | Kelvin |
| kg | kilogram |
| kg-m$^{-2}$ | kilogram per square meter |
| km | kilometer |
| km-sec$^{-1}$ | kilometer per second |
| m | meter |
| mm | millimeter |
| μm | micrometer, micron |
| N/A | not applicable, none, unitless, dimensionless |
| ohm-cm$^{-1}$ | ohm per centimeter |
| percent | percent (range of 0–100) |
| rad | radian |
| rad-sec$^{-1}$ | radian per second |
| sec | second |
| sr$^{-1}$ | per steradian |
| W | watt |
| W-m$^{-2}$ | watt per square meter |
| W-m$^{-2}$sr$^{-1}$ | watt per square meter per steradian |
| W-m$^{-2}$sr$^{-1}$μm$^{-1}$ | watt per square meter per steradian per micrometer |